Parvalbumin$^+$ interneurons enable efficient pattern separation in hippocampal microcircuits

by

Claudia Espinoza

May, 2019

A thesis presented to the

Graduate School

of the

Institute of Science and Technology Austria, Klosterneuburg, Austria

in partial fulfillment of the requirements

for the degree of

Doctor of Philosophy

I|S|T AUSTRIA

Institute of Science and Technology

The dissertation of Claudia Espinoza, titled "Parvalbumin$^+$ interneurons enable efficient pattern separation in hippocampal microcircuits", is approved by:

Supervisor: Peter Jonas, IST Austria, Klosterneuburg, Austria

Signature: _____

Committee Member: Ryuichi Shigemoto, IST Austria, Klosterneuburg, Austria

Signature: _____

Committee Member: Thomas Klausberger, Medical University of Vienna, Vienna, Austria

Signature: _____

Exam Chair: Edouard Hannezo, IST Austria, Klosterneuburg, Austria

Signature: _____

signed page is on file

I hereby declare that this dissertation is my own work and that it does not contain other people's work without this being so stated; this thesis does not contain my previous work without this being stated, and the bibliography contains all the literature that I used in writing the dissertation.

I declare that this is a true copy of my thesis, including any final revisions, as approved by my thesis committee, and that this thesis has not been submitted for a higher degree to any other university or institution.

I certify that any republication of materials presented in this thesis has been approved by the relevant publishers and coauthors.

Signature: _____

Claudia Espinoza Martinez

May 7th, 2019

signed page is on file

Abstract

Distinguishing between similar experiences is achieved by the brain in a process called pattern separation. In the hippocampus, pattern separation reduces the interference of memories and increases the storage capacity by decorrelating similar inputs patterns of neuronal activity into non-overlapping output firing patterns. Winners-take-all (WTA) mechanism is a theoretical model for pattern separation in which a "winner" cell suppresses the activity of the neighboring neurons through feedback inhibition. However, if the network properties of the dentate gyrus support WTA as a biologically conceivable model remains unknown. Here, we showed that the connectivity rules of PV$^+$ interneurons and their synaptic properties are optimized for efficient pattern separation. We found using multiple whole-cell *in vitro* recordings that PV$^+$ interneurons mainly connect to granule cells (GC) through lateral inhibition, a form of feedback inhibition in which a GC inhibits other GCs but not itself through the activation of PV$^+$ interneurons. Thus, lateral inhibition between GC–PV$^+$ interneurons was ~10 times more abundant than recurrent connections. Furthermore, the GC–PV$^+$ interneuron connectivity was more spatially confined but less abundant than PV$^+$ interneurons–GC connectivity, leading to an asymmetrical distribution of excitatory and inhibitory connectivity. Our network model of the dentate gyrus with incorporated real connectivity rules efficiently decorrelates neuronal activity patterns using WTA as the primary mechanism. This process relied on lateral inhibition, fast-signaling properties of PV$^+$ interneurons and the asymmetrical distribution of excitatory and inhibitory connectivity. Finally, we found that silencing the activity of PV$^+$ interneurons *in vivo* leads to acute deficits in discrimination between similar environments, suggesting that PV$^+$ interneuron networks are necessary for behavioral relevant computations. Our results demonstrate that PV$^+$ interneurons possess unique connectivity and fast signaling properties that confer to the dentate gyrus network properties that allow the emergence of pattern separation. Thus, our results contribute to the knowledge of how specific forms of network organization underlie sophisticated types of information processing.

Esta tesis está dedicada a:

Cada persona que con dedicación, paciencia y amor buscan y crean conocimientos significativos.

A mi madre, por bridarme toda su ternura y los cimientos que forman mi vida. A mi padre, por mostrarme el verdadero sentido del coraje, y lo que este significa en el contexto de nuestra propia fragilidad. A mi hermano, por ser una inspiración, a José por su amistad y por ser un ejemplo de que todo lo valioso requiere esfuerzo y dedicación. Finalmente a Andy por acompañarme y emprender conmigo este viaje.

This thesis is dedicated to:

Every person with dedication, patience, and love create and look for meaningful knowledge.

My mother for giving me all her tenderness and the foundations of my life. My father for showing me what courage means when we confront our fragility. My brother for being an inspiration, José for his friendship and being an example that every worthy thing requires effort and dedication. Finally, Andy for starting and walking with me on this journey.

Acknowledgments

I would like to especially thank Peter Jonas for his continuous support during my work at IST as my supervisor. For being always available for discussing anything related to this project. For showing me how perseverance and dedication are essential companions of good ideas.

I want to thank Jose Guzman for sharing all his scientific experience and providing guidance through the whole project. To Christina Altmutter and Florian Marr for their excellent technical support. For ensuring their work with dedication and patience. To Alois Schlögl for performing the large scale simulations on computer clusters and for his generosity in sharing his knowledge. To Sylvia Badureck for her continuous support with the implementation of the behavioral experiments. To Felipe Fredes for sharing his experience in setting the experiments that involved the DREADD manipulations. To the IST faculty members Jozsef Csicsvari and Ryuichi Shigemoto for giving me their feedback and providing scientific advice. To the people from the IST Graduate School, especially Vlad Cozac, who with his humor, competence, and interest in helping others, made my stay in Austria easier.

Finally, I would like to thanks all my lab colleagues, who contributed in a very diverse way to my work in an academic and non-academic manner. To Hua Hu, Itaru Arai, Nick Vyleta for giving me feedback and suggestions when I just started with electrophysiological experiments at IST. To Yoav Simon Ben for helping me with everything concerning the preparation and administration of viruses in the behavioral trials. To Xiaomin Zhang for providing information about the activity of parvalbumin+ interneurons *in vivo*. To Magdalena Picher, David Vandael and Carolina Borges for establishing excellent academic discussions and for making my life in the lab very pleasant.

About the Author

Claudia comes from Valparaiso, a colorful harbor city facing the Pacific coast of Chile. There, she studied neurorehabilitation and later worked on the treatment of children with neurological disorders in public and private institutions. Besides, she volunteers in an equine therapy center for the rehabilitation of kids with Down syndrome. At the same time, Claudia worked as a lecturer at the Medicine Faculty of the Valparaiso University in the subjects of Human Anatomy, Neuroanatomy and Neurological rehabilitation (2008-2012).

Before coming to Austria, she obtained a government scholarship (CONICYT) for conducting a master study in neurobiology at the Centre of Neurobiology and Cerebral Plasticity. There, she had her first approximation to the electrophysiological techniques studying the alterations of the inhibitory synaptic transmission in a mouse model of Duchenne muscular disease. This work was published in the journal Neurobiology of Disease 86:109-120 (2016).

In 2012, she started a Ph.D. in neuroscience at IST Austria and shortly joined to the Jonas group in 2013. Since then, her research interest was focused on studying the connectivity rules between principal neurons and interneurons in the dentate gyrus and their implications in the phenomenon of pattern separation. She had presented part of this work at the Society for Neuroscience (SfN, 2016, 2018) and at the Austrian Neuroscience Association (ANA meeting, 2017). This work was published in the journal Nature Communication 9: 4605 (2018).

Besides her doctoral work, Claudia did teaching assistance in the course Molecules, Cells, and Models (2015), enrolled for the summer course Neuron at Wright State University, Ohio (2017) and participated in the organizing committee for the "Young Scientist Symposium 2018". As recreational activities, she pretty much enjoys painting and practicing sports such as yoga, running and biking. For the future, she hopes to find a place where she can continue contributing to the scientific knowledge by creating and answering challenging questions in neuroscience.

Lists of publications and presentations appearing in the thesis

Original publication

Espinoza C, Guzman SJ, Zhang X, Jonas P. (2018) Parvalbumin$^+$ interneurons obey unique connectivity rules and establish a powerful lateral-inhibition microcircuit in dentate gyrus. Nat Commun 9: 4605

Posters

Espinoza C, Guzman SJ, Jonas P. (2016) Abundance of recurrent and lateral inhibition in the dentate gyrus of the hippocampus. Program No. 782.08. Neuroscience Meeting Planner. San Diego, CA: Society for Neuroscience, 2016. Online.

Espinoza C, Guzman SJ, Jonas P. (2017) Synaptic excitation of PV-expressing interneurons on inhibition in the dentate gyrus of the hippocampus. 15th ANA Austrian Neuroscience Association. IST Austria.

Espinoza C, Guzman SJ, Csicsvari JL, Jonas P. (2018) Unique connectivity of parvalbumin$^+$ interneurons enables efficient pattern separation in hippocampal microcircuits. Program No. 166.09. 2018. Neuroscience Meeting Planner. San Diego, CA: Society for Neuroscience, Online.

Presentations

The role of Parvalbumin$^+$ interneurons in pattern separation. (2019) Workshop on cognitive and behavioral screening of rodents and how to apply the 3Rs policy in this research. Session Neuroscience. Brno, Czech Republic.

Table of contents

Chapter 2: Methods

Chapter 3: Results

List of figures

List of tables

xi

List of abbreviations

abGCs	adult-born granule cells
ACSF	artificial cerebrospinal fluid
AP	action potential
BC	basket cell
CA1	*Cornu Ammonis* region 1
CA3	*Cornu Ammonis* region 3
CCK$^+$	cholecystokinin-positive
CGE	caudal ganglionic eminence
c_{max}	maximal connection probability experimentally measured
CNO	clozapine n-oxide
d_{half}	distance where the connection probability (c_{max}) decayed to 50%
DREADD	designer receptors exclusively activated by designer drugs
eAPs	evoked action potentials
E	excitatory
ECs	entorhinal cortex cells
EGFP	enhanced green fluorescent protein
EI	excitatory neuron to interneuron connection
EPSCs	excitatory postsynaptic currents
EPSPs	excitatory postsynaptic potentials
GABA	gamma–aminobutyric acid
GAD	glutamic acid decarboxylase
GCL	granule cell layer
GCs	granule cells
HICAP	hilar commissural-associational pathways-associated axons
HIPP	hilar perforant pathway-associated axonal terminal
hM4Di	G_i-coupled human M4 muscarinic DREADD
I	inhibitory
IF	integrate and fire
II	interneuron to interneuron chemical synapses
IML	inner molecular layer
IN	interneuron

IPSCs	inhibitory postsynaptic currents
IQR	interquartile range
IR-DIC	infrared differential interference contrast
J	synaptic strength in the network model
J_{gamma}	inhibitory gamma frequency drive to GCs in the network model
LEC	lateral entorhinal cortex
LFP	local field potential
MEC	medial entorhinal cortex
MGE	medial ganglionic eminence
OLM	oriens alveus-lacunosum-moleculare
PB	phosphate buffer
PFA	paraformaldehyde
PN	principal neuron
PV^+	parvalbumin-positive
Q	quartile: Q1, first quartile; Q2, second quartile
R_{in}	input correlation coefficient
R_{out}	output correlation coefficient
sAPs	spontaneous action potentials
SEM	standard error of the mean
SST^+	somatostatin-positive
V_{ap}	action potential propagation velocity
WTA	winner-takes-all
α	activity level in the upstream neurons. Used for the network model
γ	gain of pattern separation
ρ	reliability of pattern separation
σ	standard deviation, distance width
τ	decay time
ψ	pattern separation index

Chapter 1

INTRODUCTION

1.1 Information processing: pattern separation

The mammalian brain possesses the ability to filter, process and store sensory information inputs to respond to environmental demands with complex behaviors. In this context, distinguishing between similar animals, odors or places has become a highly relevant task for the nervous system. Pattern separation is the computational brain process for discriminating similar inputs patterns of neuronal activity into non-overlapping activity patterns, which is essential for many types of information processing that leads to a neuronal representation (Aimone et al., 2011). However, there are few brain regions where the mechanisms underlying pattern separation have been extensively studied, such as cerebellum (Cayco-Gajic et al., 2017), olfactory bulb (Friedrich and Wiechert, 2014; Gschwend et al., 2015) and hippocampus (Leutgeb et al., 2007; Leal and Yassa, 2018). For instance, in the cerebellum, pattern separation is fundamental for detecting small differences in sensory inputs and amplify them for efficiently generate a motor performance (Marr, 1969; Albus, 1971; Cayco-Gajic et al., 2017). In sensory circuits, such as the olfactory bulb (Wiechert et al., 2010) and visual system (Cohen and Maunsell, 2009) pattern separation allows the detection of small differences in the environment for eliciting appropriate behavioral responses. Most importantly, in the hippocampus, pattern separation is tightly related to the emergence of episodic memory (Rolls, 2016), in which discrimination between similar experiences becomes relevant for accurately create memory presentations and for increasing the memory storage capacity of the brain. Finally, impairments in pattern separation in humans contribute to memory and emotional deficits such as anxiety and posttraumatic stress disorders, which highlight the relevance of pattern separation in the formation of adaptive behaviors (Lange et al., 2017).

1.2 Pattern separation in the hippocampus: a historical perspective

The idea that pattern separation is required for memory formation dates back to the 1970s. Theoretical work carried by David Marr associated the recurrent hippocampal networks to temporary memory storage and recognized its limited storage capacity (Marr, 1971). Later, Hopfield and Amit while worked on attractor network models realized the importance of an upstream structure that orthogonalizes input patterns of neuronal activity (Hopfield, 1982; Amit et al., 1987). They pointed out that decorrelation of patterns would increase the storage capacity of the network and reduce the interference for the recalling of similar firing patterns. From the biological side, the "classical trisynaptic architecture" of the hippocampus (Ramón y Cajal, 1911; Andersen, 1975) was at this time already known and the powerful connection between mossy terminals and the apical dendrites of the CA3 neurons confirmed by functional and anatomical findings (Blackstad and Kjaerheim, 1961; Harris and Carl, 1986). Thus, hippocampal network models of memory introduced mossy fiber pathway as the system that provides uncorrelated activity pattern to the CA3 network from an upstream region (McNaughton and Morris, 1987; Treves and Rolls, 1992; O'Reilly and McClelland, 1994). The initial assumptions of these theoretical models included sparse activity and random projections (O'Reilly and McClelland, 1994). Despite the development of an extensive theoretical frame, it was only after two decades, that the first behavioral evidence supporting pattern separation in the hippocampus was published (Gilbert et al., 2001; McHugh et al., 2007; Clelland et al., 2009; Sahay et al., 2011) and the first place modulated granule cells (GCs) were reported (Leutgeb et al., 2007). Since then, extensive experimental work is being conducted to elucidate the mechanisms underlying pattern separation in the hippocampus.

1.3 The hippocampus: connectivity and function

The hippocampal formation is the brain structure involved in the creation and retrieval of episodic memories, which are the memories of the experiences (what) associated to a particular time (when) and place (where) (Dere et al., 2005). Therefore, the hippocampus processes spatiotemporal, perceptual and emotional information provided for many structures across the brain. Thus, most of the spatial and contextual

content is forwarded by the entorhinal cortex through the perforant path (Witter et al., 2017), while perceptual information (e.g., visual and auditory stimuli in primates) emerge from the perirhinal cortex and the parahippocampal gyrus, allowing the hippocampus to relate objects to temporal information (Eichenbaum, 2017). The amygdala and the orbitofrontal, structures involved in processing reward/avoidance value of experiences (valence), provide the emotional content by projecting to the entorhinal cortex (Rolls, 2016).

In the hippocampus, memory representations occur as a result of different computations at the level of specific subnetworks, which have been classically described in a "trisynaptic circuit" as: dentate gyrus, *Cornu Ammonis* region 3 (CA3) and *Cornu Ammonis* region 1 (CA1) (Andersen, 1975).

1.3.1 Hippocampal microcircuitry: dentate gyrus

The hallmark computation of the dentate gyrus, the input region of the hippocampus, is to convert highly overlapping synaptic input patterns into non-overlapping action potential (AP) output patterns, a phenomenon referred to as orthogonalization, decorrelation, or pattern separation (Leutgeb et al., 2007; Rolls, 2016; Cayco-Gajic et al., 2017; Chavlis and Poirazi, 2017; Leal and Yassa, 2018). The anatomical structure that supports this function is a banana-shaped formation that extends from the septal nuclei rostrally to the temporal cortex caudally, which is constituted by three layers: molecular layer, granule cell layer (GCL) and hilus (**Fig. 1.1**) (Leranth and Hajszan, 2007).

The most abundant principal neurons (PNs) of the dentate gyrus are the GCs. Roughly one million in rats and ~10 million of GCs in humans (Amrein et al., 2004; Jonas and Lisman, 2014) are tightly packed forming the GCL. They possess dendrites branching into the molecular layer while their axons extend to the hilus. GCs have unmyelinated axons, named by Ramon and Cajal "mossy fibers" characterized by large boutons that form *en passant synapses* with CA3 pyramidal neurons. Before entering to the CA3 region, each main mossy fiber branches almost seven times in thinner collaterals, extensively branching again and giving rise to much thinner collaterals that innervate mossy cells and GABAergic interneurons (Amaral et al., 2007).

The primary input of the dentate gyrus arrives from layer II of the entorhinal cortex via perforant path, which is divided into medial and lateral according to their specific cortical origin (Witter, 2007). The medial perforant path carries spatial information, arise from the medial entorhinal cortex (MEC) and innervate the middle one-third of the molecular layer of the ipsilateral dentate gyrus (Witter, 2007). In contrast, the lateral perforant path carries object-related, attentional and motivational information, originates from the lateral entorhinal cortex (LEC) and innervates the outer one-third of the molecular layer. The inner part of the molecular layer receives inputs from the contralateral dentate gyrus through the commissural/associational pathway (Amaral et al., 2007; Leranth and Hajszan, 2007). The spatial/temporal information originated in the entorhinal cortex is expanded into the dentate gyrus (GCs are 5-10 times more abundant than EC cells) and suggested to be translated into sparse representations.

Additionally, few inputs from subcortical nuclei into the dentate gyrus have also been described. Septal nuclei (medial septal nucleus and diagonal band of Broca) provide mostly cholinergic projection (50-70%), while the supramammillary area and the medial mammillary nuclei (hypothalamic input) bring glutamatergic inputs to the proximal dendrites of the GCs. Besides, the brain stem sends noradrenergic inputs from the nucleus locus coeruleus, dopaminergic projections from the ventral tegmental area, and serotoninergic afferents from medial and dorsal raphe nuclei (Amaral et al., 2007; Leranth and Hajszan, 2007).

These projections follow a specific functional – anatomical organization observed through the whole longitudinal axis of the dentate gyrus (**Fig 1.1**) (Fanselow and Dong, 2010). In rodents the dorsal part of the dentate gyrus receives inputs almost exclusively from the lateral portions of the LEC and MEC, providing mostly visual and navigational information. By contrast, the ventral regions of the dentate gyrus receive inputs from the medial parts of the LEC and MEC, which carry olfactory, visceral and gustatory information related to the emotional content of experiences (Witter, 2007; Fanselow and Dong, 2010). Moreover, each subfield of the trisynaptic hippocampal circuit maintains this topographic organization (Fanselow and Dong, 2010). Thus, the richness of the afferent system of the dentate gyrus together with their functional compartmentalization into the dorsal/ventral axis reveals the complexity of the contextual information processing and the broad functional implications of pattern separation computations.

1.3.2 Hippocampal CA3 and CA1 subfields

The activity patterns that were separated in the dentate gyrus are subsequently relayed to the CA3 subfield through the mossy fiber synapses, leading to the storage of information in the CA3 recurrent network (Bischofberger et al., 2006a; Guzman et al., 2016; Rolls, 2016). The CA3 region was shown to harbor only one-third of the dentate gyrus PNs, which are powerfully connected (each CA3 PN receives approximately 50 mossy fiber inputs) (Rolls, 2016). In addition, the connectivity among CA3 PNs is sparsely present (with a probability ~1%), and appears organized in a non-random manner into specific connectivity motifs (Guzman et al., 2016). This configuration seems to be optimized for the retrieval of the information from partial or noise cues, in a process named "pattern completion" (Guzman et al., 2016).

The CA1 subfield constitutes the main synaptic output of the hippocampus and participates in the retrieval and consolidation of information through back-projections to the neocortex (Kesner and Rolls, 2015). The CA1 PNs are functionally organized in a superficial and a depth layer (Valero et al., 2015), receiving inputs mainly from the CA3 subfield through the Schaffer collaterals (**Fig. 1.1**). These circuits underlie the emergence of the sharp-wave ripple, a physiological rhythm recognized for remarkably synchronous events appearing during consummatory behaviors (e.g., immobility, grooming) (Buzsáki, 2015). It carries the replay of the sequence of the neuronal firing resembling the activity of the neurons during previous walking periods, which is thought to contribute to the long-term storage of neuronal ensembles in the neocortex (Buzsáki, 2015). Finally, besides to the hippocampal afferent input, CA1 receives direct monosynaptic connections from the entorhinal cortex (layer II and III) which are involved in context-depend processing of fear memories (Kitamura et al., 2015) and the temporal association of memories (**Fig 1.1**) (Suh et al., 2011).
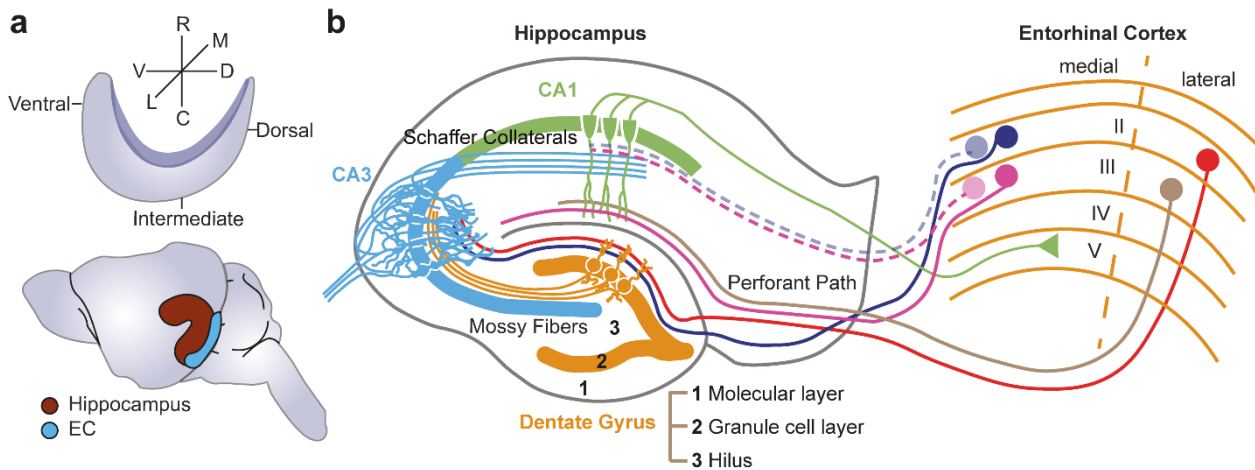
Figure 1.1: Hippocampal local circuits
(**a**) Schematic illustration of the orientation of the hippocampal longitudinal axis in rodents (Strange et al., 2014). (**b**) Schematic representation of the hippocampal trisynaptic circuit and the afferent and efferent pathways from the entorhinal cortex. The perforant path forward the primary input to the hippocampus. Mossy fibers, the terminal collateral of the GCs, innervate the PNs of CA3, while the Schaffer collaterals constitute the final path of the trisynaptic circuit synapse onto CA1 PNs. Besides, direct communication from layer II/III of the entorhinal cortex provide direct context-depending information to CA1. Continue lines indicate the direction of the trisynaptic circuit and dashed lines represent the monosynaptic connections from the entorhinal cortex. Modified from Neves et al., 2012.

Nowadays, the classical feedforward trisynaptic circuit in the hippocampus is challenged for providing a simplistic overview of the hippocampal organization. One example is the CA2 region, an area lying between CA1 and CA3 subfields (Chevaleyre and Siegelbaum, 2010), which besides of the neuronal expression of specific neuronal markers is associated to the emergence of social behaviors (Hitti and Siegelbaum, 2014; Leroy et al., 2018). Also, a more sophisticated hippocampal afferent and efferent circuit have been described, with direct entorhinal connections to each hippocampal subfield (Witter et al., 2017) and functional feedback projections from CA3 to the dentate gyrus (Amaral et al., 2007). Moreover, the classical description of the hippocampus does not consider the inhibitory component, thought to be highly unspecific at least in the neocortex (Packer and Yuste, 2011). Thus, in the light of recent findings, the hippocampal organization needs to be further discussed in terms of anatomical organization and functional computations.

1.4 Hippocampal inhibition

Synaptic inhibition in neuronal networks is mediated in large extent by GABAergic interneurons, which are very diverse in morphology, genetic expression, chemical markers, physiological properties, connectivity patterns, and tempo-spatial origin (Kepecs and Fishell, 2014). According to this diversity, interneurons are mainly classified using morphological, physiological and molecular criteria (**Fig 1.2**) (Zeng and Sanes, 2017).

Specifically, in the dentate gyrus, the first attempts for characterizing interneurons were based on Golgi technique leading to the identification of 21 different cellular types (Amaral, 1978). Further endeavors have combined physiological and morphological properties (Freund and Buzsáki, 1996; Mott et al., 1997; Sik et al., 1997; Houser, 2007; Hosp et al., 2014) resulting in the description of at least five main interneuron types (**Fig 1.2a, b**): a) axo-axonic cells: fast-spiking interneurons that target the axon initial segment of PNs; b) basket cells: interneurons innervating most of the GCL and inner molecular layer, together with axo-axonic cells provide the perisomatic inhibition to GCs; c) hilar-perforant pathway-associated axonal-terminal (HIPP) cells: large multipolar interneurons with spiny dendrites in the hilar region. Their axons innervate the outer molecular layer; d) hilar-commissural-associational pathways-associated axons (HICAP) cells: pyramidal-shaped cells with bodies located in the subgranular layer and axons extended into the inner molecular layer and GCL; e) molecular layer perforant path-associated (MOPP) cells: provide feedforward inhibition to GCs by targeting their dendritic shaft (Stam et al., 2013). The functional characterization of these interneurons have been done in *in vitro* and *in vivo* experiments (Sik et al., 1997; Klausberger and Somogyi, 2008; Stam et al., 2013).

Genetic and molecular markers have also been extensively used to classify GABAergic interneurons, with the advantage of providing genetic tools for identifying and manipulating the activity of specific groups of interneurons (Taniguchi et al., 2011). The three major interneuron types in the hippocampus are parvalbumin (PV), somatostatin (SST), and cholecystokinin (CCK) expressing interneurons (**Fig 1.2c**) (Freund and Buzsáki, 1996; Savanthrapadian et al., 2014).

1.4.1 Parvalbumin positive (PV$^+$) interneurons

This group constitutes almost 15% of the GABAergic interneurons in the hippocampus (Hosp et al., 2014). The two most important morphological types are the basket cells and axo-axonic cells, which provide perisomatic inhibition to PNs by targeting their soma and axonal initial segment. Somatic current injection into PV$^+$ interneurons elicits a fast non-accommodating spiking phenotype, allowing their easy identification (Hu et al., 2014). In the dentate gyrus, PV$^+$ interneurons exhibit dendrites that expand into the inner molecular layer and hilus, suggesting their participation in feedback and feedforward inhibition (Hosp et al., 2014). Also, PV$^+$ interneurons provide fast and precise synaptic signaling (Hu et al., 2014), whose contributing mechanisms were proposed as the following: first, weakly excitable dendrites enriched in Kv3 channels, that acting synergistically with AMPA receptors, generate large and fast excitatory postsynaptic potentials (EPSPs). This effect was proposed to decrease the temporal window for summation and promotes AP generation at high speed with precise temporal resolution (Hu et al., 2014). Second, the high axonal expression of Na$^+$ voltage channels allows conveying information in a highly reliable manner together with an increased speed of AP propagation (Hu and Jonas, 2014). Finally, their axon terminals were shown to almost exclusively express P/Q type calcium channels (Hefft and Jonas, 2005), which tightly coupled to the release sensors, shortens the synaptic delay and enhances the temporal precision of the transmitter release (Hu et al., 2014).

At the network level, the fast output of the PV$^+$ interneurons allows the synchronization of neuronal ensembles and the emergence of cortical rhythms (Bartos and Elgueta, 2012). In CA1 region, recordings in anesthetized rodents show fast-spiking interneurons firing time-locked to the descending phase of gamma oscillations (Klausberger et al., 2005), while in head-fixed running mice PV$^+$ interneurons seem to regulate the theta phase precession (Royer et al., 2012).

Furthermore, the involvement of PV$^+$ interneurons in the performance of accurate neuronal computations has also been reported in other brain circuits. In the primary visual cortex, the optogenetic activation of PV$^+$ interneurons sharpen neuronal feature selectivity and improve orientation discrimination (Lee et al., 2012). Besides, PV$^+$ interneurons modulate gain responses of primary sensory computations (Wilson et al., 2012). Finally, their role in complex behavioral tasks such as associative-fear or reward learning has also been explored in circuits of the amygdala, the auditory

system and the prefrontal cortex (Letzkus et al., 2011; Davis et al., 2017; Marek et al., 2018; Takesian et al., 2018).

1.4.2 Somatostatin positive (SST+) interneurons

Interestingly, SST+ interneurons share an embryological origin with PV+ interneurons in the medial ganglionic eminence (MGE) (Xu et al., 2004; Butt et al., 2005). Specifically in the dentate, gyrus SST+ interneurons account for almost 16% of the glutamic acid decarboxylase (GAD)-expressing interneurons (Tallent, 2007). They were classically identified as HIPP cells (Savanthrapadian et al., 2014), dendritic targeting interneurons that provide weak feedback inhibition to the local GCs (Sik et al., 1997; Tallent, 2007; Royer et al., 2012; Hosp et al., 2014). However, a recent study has identified a second group of SST+ interneurons termed hilar interneurons (HILs), which target local GABAergic interneurons and project to the medial septum (Yuan et al., 2017).

Although SST+ interneurons have not been as extensively studied as PV+ interneurons, the current evidence suggests that these interneuron types modulate neural computations in a highly complementary manner (Royer et al., 2012; Wolff et al., 2014; Khan et al., 2018). Specifically, at the cellular level, dendritic inhibition regulates synaptic plasticity by modulating the gating for dendritic electrogenesis (Lovett-Barron et al., 2012). At the network level, neocortical SST+ interneurons receive excitation from nearly 30% of surrounding PNs and provide inhibition to almost 100% of these cells (Urban-Ciecko and Barth, 2016). Thus, SST+ interneurons, specifically Martinotti cells, control neighboring PNs by disynaptic inhibition when PNs discharge at high frequencies (Silberberg and Markram, 2007). This form of delayed lateral inhibition is characterized by a slow temporal resolution response that can be modulated by cholinergic inputs, which makes it suitable for controlling synaptic integration and burst firing (Obermayer et al., 2018). However, if this specific inhibitory motif is present in the hippocampus remains elusive.

1.4.3 Cholecystokinin positive (CCK$^+$) interneurons

The best characterized CCK$^+$ interneurons in the dentate gyrus are HICAP and CCK$^+$ basket cells. They share with PV$^+$ interneurons some morphological properties such as the dendritic arborization of HICAP in the molecular layer and hilus. In addition, CCK$^+$ basket cells target the soma and proximal dendrites of PNs, providing perisomatic inhibition together with PV$^+$ interneurons. However, CCK$^+$ interneurons also possess unique properties that allow to distinguish them from other interneuron types. First, in contrast to PV$^+$ interneurons, CCK$^+$ interneurons originate from the caudal ganglionic eminence (CGE) (Kepecs and Fishell, 2014). Second, they show a regular non-accommodating spiking phenotype after somatic current injection. Third, according to the expression of molecular markers, CCK$^+$ interneurons can be further classified in VGlut3 expressing neurons and vasoactive intestinal peptide (VIP) positive cells (Somogyi et al., 2004). Fourth, at the input level, electron microscopy studies revealed that CCK$^+$ interneurons receive three times less excitation than PV$^+$ interneurons in CA1 (Gulyás et al., 1999; Mátyás et al., 2004) which could explain why the amplitude of excitatory postsynaptic currents (EPSCs) recorded at CCK$^+$ are smaller than PV$^+$ interneurons contained synapses (Bartos and Elgueta, 2012). Fifth, at the output level, CCK$^+$ basket cells exhibit less reliable neurotransmitter release (Hefft and Jonas, 2005). Additionally, these terminals characteristically express endocannabinoid 1 receptors (CB1Rs) (Katona et al., 1999), which can further provide synaptic modulation (Glickfeld and Scanziani, 2006). Finally, at the synaptic level, the weak coupling between the N-type calcium channel and the calcium sensors could explain the low temporal resolution that characterized CCK$^+$ synapses (Hefft and Jonas, 2005); that together with broadening of the AP at the synaptic terminals (after repetitive stimulation) could confer a wide temporal windows for synaptic integration (Bartos and Elgueta, 2012).

At the network level, *in vivo* studies in the hippocampus have shown that during fast network oscillations, CCK$^+$ interneurons are less reliable recruited than PV$^+$ interneurons. Moreover, CCK$^+$ interneurons fire predominantly during the ascending phase of theta waves, while PV$^+$ interneurons do it in the descending phase, suggesting a differential contribution to the formation of neuronal ensembles (Klausberger et al., 2005).
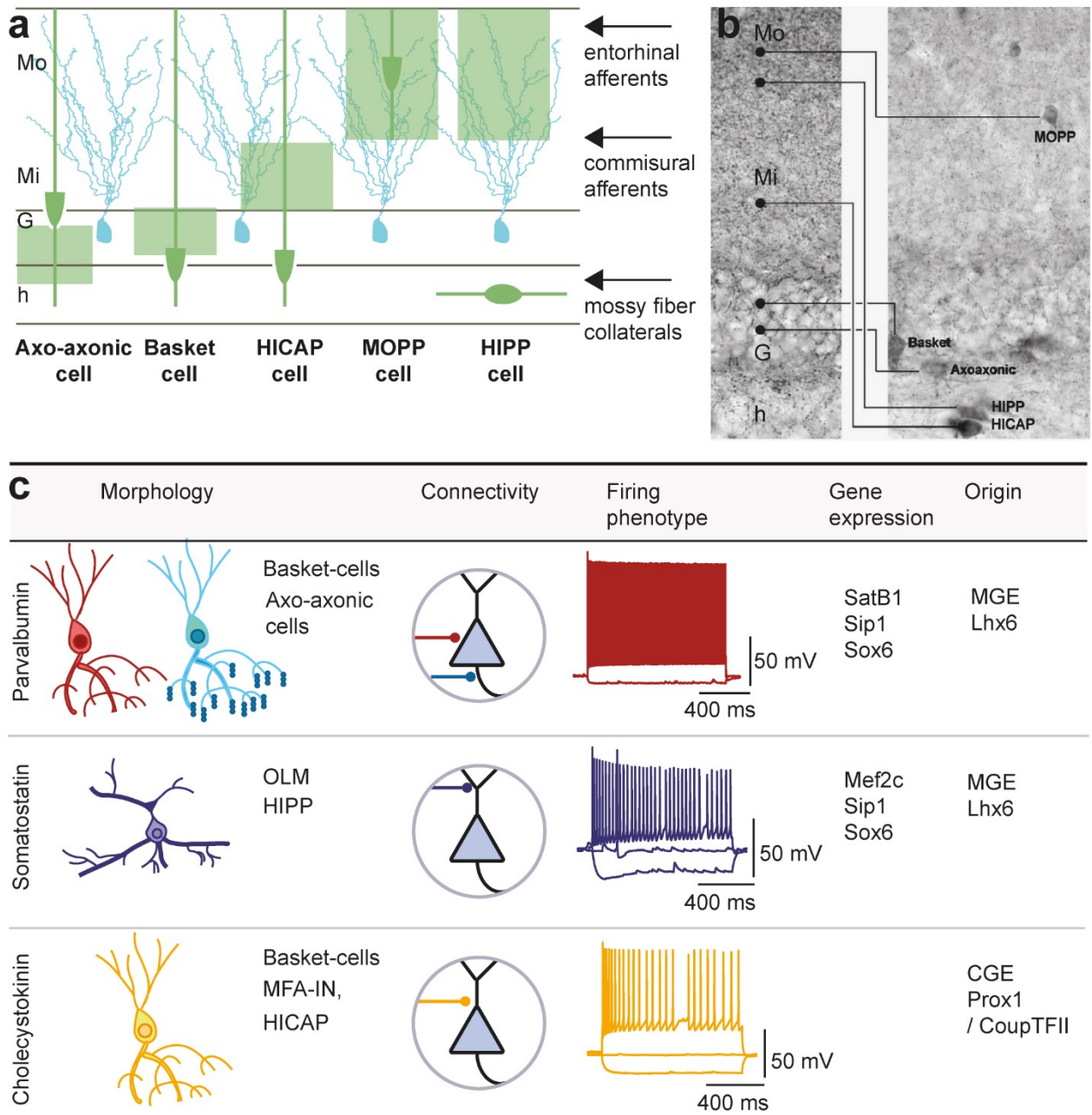
Figure 1.2: Interneuron classification in the hippocampus.
(**a**) Principal morphological type of interneurons in the dentate gyrus (adapted from Freund and Buzsáki, 1996). Five interneuron types are depicted in green. The green horizontal lines indicate the main orientation and distribution of the dendritic arborization. The green boxes represent the region in which the axon of each interneuron typically branches. On the background are GCs (cyan). (**b**) GAD65 labeled axons in the dentate gyrus and their hypothetical cell type origin (taken from Houser 2007) (a–b) Mo = outer molecular layer, Mi = inner molecular layer, G = granule cell layer, and H = hilus. (**c**) Characterization of hippocampal interneuron classified according to chemical expression. Parvalbumin (PV⁺), somatostatin (SST⁺) and cholecystokinin (CCK⁺)-positive expressing interneurons constitute the major GABAergic interneurons in the hippocampus. Basket cells and axo-axonic cells provide perisomatic inhibition and exhibit a characteristic fast-spiking phenotype under somatic current injection. PV⁺ interneurons originate at different embryological stages (i.e., axo-axonic cells at the embryonic day 15 to 18) from Nkx2.1 progenitors

11

in the medial ganglionic eminence (MGE). The activity of Nkx2.1 induces the expression of Lhx6, which promotes the differentiation of PV^+ and SST^+ interneurons. SatB1, Sip1, and Sox6 are transcription factors expressed by PV^+ and SST^+ interneurons that selectively affect their development. Morphological examples of SST^+ interneurons are oriens-alveus-lacunosum-molecular (OLM) interneurons in CA1 and perforant pathway-associated axonal terminal (HIPP) cells in the dentate gyrus. They are dendritic-targeting interneurons and share an embryological origin with PV^+ interneurons. CCK^+ interneurons constitute a highly heterogeneous group in the hippocampus. The CCK^+ basket cells, the most well studied CCK^+ interneuron type, are present in all hippocampal subfields. CCK^+ mossy-fiber-associated interneurons (MFA-IN) are found in CA3 while CCK^+ commissural-associational pathways-associated (HICAP) interneurons are located in the dentate gyrus. CCK^+ basket cells provide perisomatic inhibition, exhibit a regular non-accommodating firing phenotype and have an embryological origin at the caudal ganglionic eminence (CGE) (Bartos and Elgueta, 2012; Kepecs and Fishell, 2014). Firing patterns were obtained from our recordings.

Overall, in the dentate gyrus, the interneuron diversity ensures a fine-tuning of neuronal computations, allowing the emergence of sophisticated forms of information processing, which are far from merely guarding to excitatory networks from runaway of excitation (Douglas et al., 1995). Among these functions are to provide feedforward and feedback inhibition, affect the timing of the signals, synchronize neuronal ensembles, control neuronal thresholds, modulate the synaptic gain and segregate the activity of PNs through lateral inhibition (Hu et al., 2014). However, it is not clear how local network topologies involving PNs and interneurons (INs) ensure the emergence of such computations. So far, it is known specific interneurons targeting either dendritic or somatic domains or even higher order of network organization, such as fast and slow forms of lateral inhibition, involving specific interneuron types (Obermayer et al., 2018). However, for understanding the structural bases of neuronal computations further research is needed. Thus, the differential contribution of each interneuron type to the diverse forms of information processing such as pattern separation remains for being elucidated.

1.5 Local connectivity and information processing

The understating of the function of a brain region requires not only the study of its elementary units (neurons) but also the way that each component interacts. Graph theory, a branch of the mathematics born in the 18th century (Euler, 1736), provides models and measurements that allow the study of networks (graphs) or systems composed of interconnected elements (Sporns, 2018). The reasoning behind the study of network topologies emerges from the notion that connectivity is tightly related to local functional specializations (Sporns, 2018). Thus, following the principles "send only what is needed, send at the lowest acceptable rate; minimize wire, which is length and diameter of all neuronal processes" (Sterling and Laughlin, 2015) each brain circuit had strategically evolved for accomplishing specific functions under energetic and spatial constraints (Bullmore and Sporns, 2012). Moreover, Passingham and collaborators proposed that different brain areas possess "connectional fingerprints" that reveal their specific network functions (Passingham et al., 2002).

Accordingly, there is increasing evidence showing specific local features in the organization of mammal neuronal circuits (**Fig 1.3**). The combination of techniques (e.g., electrophysiology, calcium imaging) for sampling activity of neuronal population associated to graph theory analysis (Bullmore and Sporns, 2009) have revealed macroscopic connectivity rules at the circuit level and specific connectivity motifs at the cellular level. Motifs according to graph theory represent patterns of connectivity (edges are the connections mediated by chemical or gap junction synapses) between few nodes (neurons) (Sporns, 2011). According to some authors, motifs may underlie the elementary units of information processing in neuronal circuits and could provide the structural bases for the emergence of behavioral relevant responses (Schröter et al., 2017). Among non-random topological features of neuronal networks are:

1.5.1 Distance-dependent connectivity

Studies using intracellular recordings in the primary auditory cortex (Levy and Reyes, 2012) and hippocampus (Strüber et al., 2017) have shown connection probabilities between PN–INs decaying as a function of the intersomatic distance. This organization may support the emergence of specific local computation such as synchronic activity between neurons in the gamma frequency range (Strüber et al., 2017). Moreover, changes in connection probabilities as a function of the intersomatic distance seems to be circuit specific since it was not observed among PNs in the CA3 (Guzman et al., 2016).

1.5.2 Clustered connectivity

A neuronal cluster occurs when neighbors of a node are directly connected to each other (Bullmore and Sporns, 2012). In the mammalian brain, the evidence for synaptic clustering started with the finding of reciprocally connected PNs in layer V of the neocortex appearing with a higher probability than expected by chance (Markram, 1997). Later Song and collaborators performing simultaneous quadruple whole-cell recordings in the visual cortex, showed that clusters of neuronal triplets were overrepresented (Song et al., 2005). A higher order of clustered connectivity is depicted by small-world organization, a topological description of global network complexity introduced by Watts and Strogatz (Watts and Strogatz, 1998). Small-world networks are characterized for being highly clustered and yet having short equivalent path lengths (number of synapses that need to be traversed to connect two nodes) in comparison to random networks (Schröter et al., 2017) (**Fig 1.3a**). This network topology is observed among PNs in the neocortex (Perin et al., 2011). Theoretical models have found that small-world organization enhances information-propagation speed and synchronicity between neurons (Watts and Strogatz, 1998). Finally, there is a conceptual distinction between 'topological clustering,' which refers to structural connectivity and 'spatial clustering' which is related to the drop-off connection probability due to the distance-dependent phenomenon (see 1.5.1 distance dependent connectivity) (Schröter et al., 2017).

1.5.3 Long-tailed distribution of connections

In the somatosensory cortex, one study using multi-electrode arrays and transfer entropy analysis found that the degree distribution (number of connection per neuron) was heavy-tailed, indicating the presence of high-degree neurons (hubs, **Fig 1.3b**) (Shimono and Beggs, 2015). Long-tailed distributions were more often observed in functional studies involving neuronal pair recordings, in which the synaptic strength of the majority of the EPSPs had small amplitude with only a small proportion of large EPSPs (Buzsáki and Mizuseki, 2014). The functional relevance of this phenomena has been explored by Cossell and collaborators, whose results showed that in the primary visual cortex few strong and reciprocal connections occurred between neurons with similar spatial field while weak connections were present among neurons with uncorrelated responses (Cossell et al., 2015).

1.5.4 Network motifs

In addition to the classical network motifs (**Fig. 1.3d**), which are feedforward inhibition, feedback inhibition (Jonas and Buzsáki, 2007), disinhibition, feedforward excitation, feedback excitation and convergence/divergence motifs (Schröter et al., 2017) (**Fig. 1.1d**), higher-order networks motifs have been used for describing network topologies. The bidirectional connectivity motif between PNs constitutes an example, which is overrepresented in several brain region (Song et al., 2005; Oswald et al., 2009; Guzman et al., 2016; Schröter et al., 2017). One study performed in layer V of the somatosensory cortex relates the high abundance of bidirectional motifs to the 'neighbor rule,' which states that the degree of connectivity is directly proportional to the number of common neighbors (**Fig. 1.3a**) (Perin et al., 2011). Besides, there are inhibitory specific motifs containing chemical and gap junction synapses, which have been described in the cerebellum when triplets of neurons were analyzed (Rieubland et al., 2014).

a Types of connectivity distributions

Log count / Log distance

1. Uniform: Erdös and Rényi, 1959
2. Nearest neighbor: Chua, 1998
3. Small-world: Watts and Strogatz, 1998
4. Power-law: Wang and Chen, 2003
5. Exponential: Sholl, 1956
Braitenberg and Schüz, 1998

b Hub node

c Rich club

d Circuit motifs

1 Disynaptic inhibition
2 Desinhibition
3 Feedback inhibition
4 Lateral inhibition
5 Reciprocal connections
6 Mutual inhibition
7 Convergence and divergence

node, principal neuron   interneuron   edge, connection   excitatoty effect   inhibitory effect

Figure 1.3: Structured connectivity in brain networks.
(**a**) Different macroscopic connectivity rules are schematized. 1) Erdös and Rénji networks have neurons (nodes) with connection probabilities uniformly distributed across different intersomatic distances (path length). 2) Random networks with connections restricted to the neighbor cells. 3) Small-world networks are characterized by local cluster of neurons (hubs) and short path length. 4) Networks with a power-law distribution of connectivity regardless of any other structure are called free-scaled networks. 5) Braitenberg and Schüz described a functional connectivity network that follows an inverse power function rule. Schematic taken from Freeman and Breakspear, 2007.
(**b–c**) Microscopic connectivity rules: (b) complex networks with high degree nodes (highly interconnected) are called hubs (orange). (c) Hubs can be part of a bigger structured network, rich clubs (orange), which contain a core of nodes more connected than hubs inserted in random networks. Note these graphical representations depict undirected connectivity (--), in which edges (connections)

have not directions. (**d**) Description of heterosynaptic motifs with both inhibitory and excitatory neurons: 1) feedforward inhibition or local disynaptic inhibition; 2) disinhibition; 3) general form of feedback inhibition and two especial cases of feedback inhibition: 4) lateral inhibition and 5) recurrent inhibition. 6) Mutual inhibition, 7) convergence and divergence motifs. Note these representations correspond to directed graphs, in which the edges (synapses) have directionality. (b–d) Modified from Schröter et al 2017.

Despite the abundant description of specific motifs at the cellular and network level, it is not clear the relation between these architectural designs and precise network functions. Some experimental and theoretical work indicates that reciprocal motifs between PNs may be involved in synchronizing neuronal activity, increasing the signal of inputs and shaping receptive fields (Ko et al., 2011; Lee et al., 2016; Schröter et al., 2017). In the olfactory system, convergence and divergence motifs have been hypothesized to support efficient information transmission providing a higher signal to noise ratio (Euler et al., 2014; Jeanne and Wilson, 2015). Moreover, chain motifs in the hippocampal CA3 circuit are crucial for retrieval information in a network model of pattern completion (Guzman et al., 2016).

Higher order brain functions are network phenomena that emerge as a collective property of a large number of neurons (Sporns, 2011). Regarding the structural bases of these computations, most of the research has been focused on the study of large-scale neurocognitive networks (Bullmore and Sporns, 2009; Sporns, 2011) concerning functions such as language, spatial awareness, object recognition, executive functions or memory (Mesulam, 1998). In particular, segregation and integration are the two architectural principles underlying these functions. In this regard, convergence higher-order motifs and synchrony have been involved in the functional integration required for such computations (Sporns, 2011). Also, studies have recognized hub neurons, small-world properties, feedforward and feedback motifs participating in the emergence of cognitive functions (Bullmore and Sporns, 2009; Sporns, 2011). However, despite the assumption that the properties of local connectivity determine the appearance of complex computations, further experimental research is needed to provide biological substrate to higher order functions such as pattern separation.

1.6 General mechanisms of pattern separation

Extensive theoretical work has been conducted for elucidating the network properties for supporting efficient pattern separation. Among the primary mechanisms are adult neurogenesis, thresholding, inhibition, and expansion and sparse coding. Moreover, the contribution of each mechanism to pattern separation seems to be circuit specific. Thus, in the cerebellum, code expansion has a predominant role in decorrelating input patterns (Cayco-Gajic et al., 2017) while in the olfactory system, inhibition seems to be the most crucial mechanism (Lin et al., 2014; Gschwend et al., 2015).

1.6.1 Adult-born granule cells (abGCs)

Theoretical work supports the hypothesis that abGCs could facilitate pattern separation by providing uncorrelated inputs to the network (Rolls, 2013). Besides, experimental studies in which mice undergo manipulations for decreasing abGCs show impairs in fine discrimination while performing in a pattern separation task (Clelland et al., 2009; Aimone et al., 2011; Nakashiba et al., 2012). However, animals with increased neurogenesis showed difficulties for discriminating between very different environments in a contextual-fear discrimination paradigm probably as a consequence of overgeneralization (Clemenson et al., 2015). Additionally, despite the increased excitability of abGCs, manipulations of adult neurogenesis inversely correlate with the overall activity in the dentate gyrus, which seems to be related to a reduction of the inhibitory input to the network (Johnston et al., 2016). This effect could be explained for the limited ability of abGCs for recruiting feedback inhibition (Temprana et al., 2015). Thus, functional distinction between mature and immature abGCs in encoding new representation has been done (**Fig. 1.4b**). Overall, despite the vast amount of experimental data (França et al., 2017) the mechanism by which adult neurogenesis contribute to orthogonalize input patterns remains controversial (Cushman et al., 2012; Groves et al., 2013).

1.6.2 Thresholding

Theoretical models have shown that synaptic non-linearities can affect the correlated activity of randomly connected neurons (De la Rocha et al., 2007; Wiechert et al., 2010). Wiechert and colleagues showed that the thresholding mechanism notable decreases correlation but increases the sparseness of the output activity in a feedforward circuit resembling the connectivity of the olfactory bulb (**Fig. 1.4c**). This silencing effect was overcome by adding recurrent connections to the network, which additionally amplified the effect of thresholding by decorrelating the output activity and feed them back into the network (Wiechert et al., 2010).

1.6.3 Expansion coding

This mechanism is observed in feedforward networks spreading the information into a large population of neurons (Cayco-Gajic et al., 2017). Early theoretical work in cerebellum conducted by Marr and Albus suggested that at mossy fiber–GC synapses, divergent-excitatory networks enhance the capacity of pattern discrimination and increase the learning speed of the Purkinje cells (Marr, 1969; Albus, 1971). Feedforward divergent excitatory networks have also been described between the entorhinal cortex and the dentate gyrus (Witter, 2007), but the contribution of this mechanism to pattern separation at this location has not been addressed yet.

1.6.4 Sparseness

The encoding of information using sparse active neurons is referred to as 'sparse coding.' Different network modalities use this strategy for increasing storage capacity, improving contrast between similar inputs, optimizing energy and facilitating the read-out information in subsequent levels of processing (Olshausen and Field, 2004). Concerning pattern separation, theoretical and experimental evidence suggests that in the input layer of the cerebellum, sparse connectivity is essential for separating spatially correlated inputs, allowing to the network processes information over a wide range of activity patterns (**Fig. 1.4d**) (Billings et al., 2014; Cayco-Gajic et al., 2017). Thus, this mechanism is also suitable for pattern separation in the dentate gyrus,

where GCs characteristically have a low spontaneous activity (Pernía-Andrade and Jonas, 2014) allowing the formation of a sparse and distributed code.
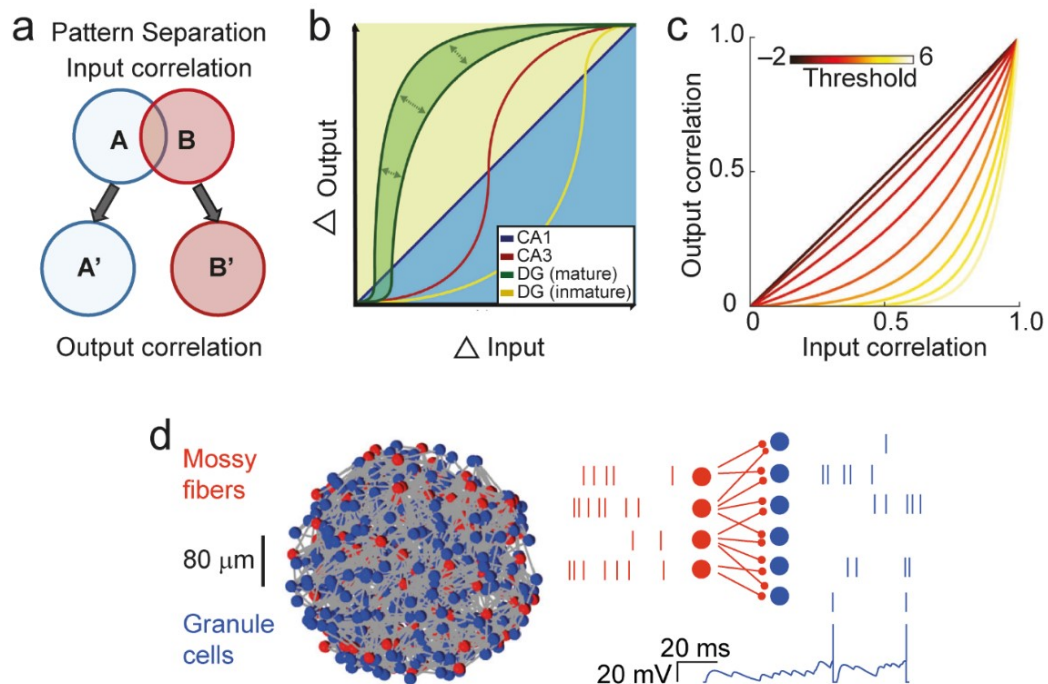
Figure 1.4: Mechanisms of pattern separation.
(**a**) A schematic representation of pattern separation. Venn diagrams of input and output patterns. Overlapping input patterns (A, B; top) are converted into non-overlapping output patterns (A', B'; bottom). (**b**) Effect of adult-born GCs (abGCs) in neuronal computations (Johnston et al., 2016). Here, the yellow area represents the pattern separation while the light blue area indicates pattern completion computation (Guzman et al., 2016). The Blue diagonal represent non-computation. Immature abGCs have double effects, for one hand they integrate patterns across a wide range of inputs, resulting in pattern completion, in the other hand, they dynamically modulate pattern separation by acting on mature abGCs at the network level (Johnston et al., 2016). (**c**) Thresholding mechanism at the olfactory bulb-like circuit (Wiechert et al., 2010). Increasing the threshold level in the network can result in strong decorrelations, which is gradually represented by the output–input Person correlation curves for different thresholds. This effect was modeled in a stochastic system of rectifying elements connected by synapses of uniform weight (Wiechert et al., 2010). (**d**) Sparse connectivity at the cerebellum. A biologically detailed spiking network model of the cerebellar input layer was used for probing that sparse synaptic connectivity is essential for separating correlated input patterns over a wide range of network activity. Bottom, an example of a GC voltage trace (Cayco-Gajic et al., 2017).

1.6.5 Winner-takes-all (WTA) mechanism

A highly attractive model of pattern separation is based on a WTA mechanism and feedback inhibition (Majani et al., 1988; de Almeida et al., 2009; Myers and Scharfman, 2009; Tetzlaff et al., 2012; Faghihi and Moustafa, 2015) (**Fig. 1.5**). WTA is a mechanism in which the selection of active neurons occurs through competitive stages in recurrent networks (Chen, 2017). The "winner neurons" are the cells having higher firing rates or fastest responses, and exert the most robust inhibition on its competitors (Coultrip et al., 1992; Maass, 2000). This model has been widely used for explaining feature selectivity and pattern formation across brain regions (Ermentrout and Cowan, 1979; Wang, 2002; Tozzi and Peters, 2018). However, most of the experimental support for this model comes from the olfactory system (Wiechert et al., 2010; Lin et al., 2014; Gschwend et al., 2015). Similar mechanisms may operate in the dentate gyrus (Engin et al., 2015; Temprana et al., 2015), but the details of this operation remain unclear. In particular, it is unknown whether the rules of PN–INs connectivity are adequate to support pattern separation and the identity of the interneuron type involved in the circuit.
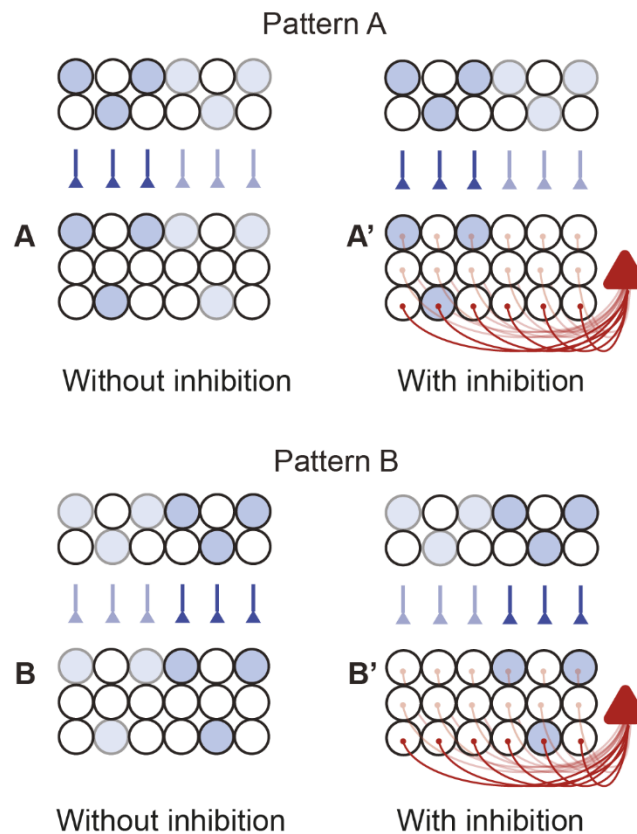
Figure 1.5: Pattern separation mediated by winner-takes-all mechanism.
Schematic illustrations of the network mechanism underlying pattern separation. Top, left, activity pattern A in upstream neurons (e.g., in the entorhinal cortex; top), causes the firing of a large subpopulation of downstream neurons (e.g., GCs) in the absence of inhibition (including cells receiving various levels of excitatory drive, dark and light blue). Top, right, however, in the presence of inhibition, a small subpopulation would fire (including only cells with the strongest drive, "WTA" mechanism). Bottom, for a slightly different activity pattern B, the output pattern is similar in the absence of inhibition but very different in the presence of inhibition. Thus, overlapping input patterns (A, B) are converted into non-overlapping output patterns (A', B'). Triangles: GABAergic interneurons; circles, principal neurons: entorhinal cortex neurons (ECs) or GCs.

1.7 Inhibition and WTA in pattern separation

Two forms of local feedback inhibitory motifs have been proposed: recurrent inhibition, in which an active PN inhibits itself via reciprocal PN–IN connections (**Fig. 1.1d**), and lateral inhibition, in which an active PN inhibits neighboring PNs but not itself (Jonas and Buzsáki, 2007). Theoretical work has recognized the importance of inhibitory feedback motifs for decorrelating neuronal activity (Tetzlaff et al., 2012), relevant process not only for improving the readout of information from a given neuronal ensemble (e.g. in presence of noise) (Tetzlaff et al., 2012) but also for increasing the storage capacity in downstream networks (Marr, 1971). Experimental evidence based on electrophysiological recordings and calcium imaging suggests the role of inhibition for decorrelating activity patterns in the neocortex (Sippy and Yuste, 2013). Moreover, one study in macaques chronically implanted with multielectrode arrays showed that nearby neurons in the visual primary cortex exhibit uncorrelated activity even when sharing similar orientation tuning. A suggested explanation for this phenomenon was the presence of a mechanism that is actively decorrelating the firing of the PNs, yet the details of such operation are not well understood (Ecker et al., 2010).

Furthermore, models of WTA with lateral inhibition have been already implemented in biologically inspired networks showing that this mechanism could exist under certain network constraints (Coultrip et al., 1992; Shoemaker, 2015). Specifically, the dentate gyrus a neuronal implementation of WTA mechanism requires lateral inhibition, recurrent inhibition may be counter-productive, because it could suppress potential winners (Jonas and Buzsáki, 2007; de Almeida et al., 2009; Chow

et al., 2012). However, experimental data show that in both neocortex and brain areas tightly connected to the hippocampus, recurrent inhibition and lateral inhibition appear is equally represented. Thus, PN–IN connectivity in these brain regions is the combination of a high excitatory connection probability with a non-random enrichment of recurrent motifs (Holmgren et al., 2003; Yoshimura et al., 2005; Couey et al., 2013; Peng et al., 2017). We think that such a circuit design would be inappropriate for pattern separation in the dentate gyrus.

Overall in the dentate gyrus, the mechanisms of pattern separation are entirely unclear. We propose that one of the primary mechanism underlying pattern separation in the dentate gyrus is based on WTA mechanism. However, whether the PN–IN connectivity in the dentate gyrus is specialized to support pattern separation remains an open question. Besides, the identity of the specific interneuron types involved in circuits performing pattern separation also remains for being addressed.

1.6 Aim of this project

The principal aim of this project was to elucidate the local synaptic mechanisms of pattern separation in the dentate gyrus. To achieve this goal, we combined experimental and theoretical approaches. To examine functional PN–IN connectivity rules, we performed simultaneous whole-cell patch-clamp recordings from up to seven GCs and up to four GABAergic interneurons in the dentate gyrus. To identify interneurons we used different transgenic mouse lines in which either PV$^+$, SST$^+$ or CCK$^+$ neurons were fluorescently labeled. Our experiments revealed a uniquely high abundance of lateral inhibition, primarily mediated by PV$^+$ interneurons and an overrepresentation of specific disynaptic motifs containing PN and INs (i.e., convergence, divergence, and mutual inhibition motifs). As a second approach, we developed a full-size biologically inspired model of the dentate gyrus based on our empirical connectivity. In this way, we could strictly preserve the connectivity rules of GC–PV$^+$ interneurons networks while studying the mechanisms underlying pattern separation. Our theoretical work supports the hypothesis that in the dentate gyrus, strong lateral inhibition, and structured connectivity allow efficient pattern separation. Finally, our behavioral data show for the first time the involvement of PV$^+$ interneurons for discriminating between highly similar contexts when mice are acutely exposed to the environments, suggesting a role of dentate gyrus PV$^+$ interneurons in pattern separation.

Chapter 2
METHODS

2.1 Experimental methods

2.1.1 Hippocampal acute slice preparation

Experiments on genetically modified mice were performed in strict accordance with institutional, national, and European guidelines for animal experimentation and were approved by the Bundesministerium für Wissenschaft, Forschung und Wirtschaft of Austria (A. Haslinger, Vienna; BMWFW-66.018/0007-WF/II/3b/2014; BMWF-66.018/0010-WF/V/3b/2015; BMWFW-66.018/0020-WF/V/3b/2016).

To label PV$^+$ interneurons, C57BL/6J PV-Cre knockin mice (http:/jaxmice.jax.org/strain/008069) crossed with Ai14 loxP-flanked red fluorescent protein tdTomato reporter mice (https://www.jax.org/strain/007914) were used. To identify SST$^+$ interneurons, somatostatin-ires-Cre mice (C-SSTtm1Npa, kindly provided by H. van der Putten; Novartis Pharma; MTD36044, Basel, Switzerland) crossed with Ai14 tdTomato reporter mice. Finally, to label CCK$^+$ interneurons, CCK-ires-Cre/DLX 5/6-Flp mice (https://www.jax.org/strain/012706 and https://www.jax.org/strain/010815) were crossed with dual reporter mice expressing either EGFP or tdTomato (RCE = R26R CAG boosted EGFP mice, https://www.jax.org/strain/010812; Ai65, https://www.jax.org/strain/021875) (Taniguchi et al., 2011). Mice (20- to 44-days-old; mostly postnatal day 20–25) of either sex were lightly anesthetized with isoflurane (Forane, AbbVie, Vienna). For animals up to postnatal day 30, mice were sacrificed by decapitation. For animals older than 30 days, transcardial perfusion was performed with ice-cold sucrose-artificial cerebrospinal fluid (sucrose-ACSF) solution. Mice were deeply anesthetized with isoflurane followed by the intraperitoneal injection of a mixture of xylazine (0.5 ml, 2%), ketamine (1 ml, 10%), acepromazine (0.3 ml, 1.4%), and physiological NaCl solution (1.5 ml, 0.9%). Anesthetics were applied at a dose of 0.033 ml/10 g body weight. The depth of the anesthesia was verified by the absence of toe pinch reflexes.

For preparing hippocampal slices, the brain was rapidly removed and immersed in ice-cold sucrose-ACSF solution during dissection. A block of tissue containing the

hippocampus was transferred to a vibratome (Leica VT 1200), and transverse slices of 300-μm thickness were cut with a blade oscillation amplitude of 1.25 mm and a blade forward movement velocity of 0.03 mm s^{-1} (Bischofberger et al., 2006b). Finally, slices were incubated at ~35°C in ACSF for 30 minutes and subsequently maintained at ~22°C for maximally 5 hours before transfer into the recording chamber.

2.1.2 Solutions and chemicals

The ACSF used for recordings contained 125 mM NaCl, 25 mM NaHCO$_3$, 25 mM glucose, 2.5 mM KCl, 1.25 mM NaH$_2$PO$_4$, 2 mM CaCl$_2$, and 1 mM MgCl$_2$. The sucrose standard artificial cerebrospinal fluid (sucrose-ACSF) used for dissection contained 64 mM NaCl, 25 mM NaHCO$_3$, 10 mM glucose, 120 mM sucrose, 2.5 mM KCl, 1.25 mM NaH$_2$PO$_4$, 0.5 mM CaCl$_2$, and 7 mM MgCl$_2$. The osmolarity of the solutions was 290–315 mOsm and the pH was maintained at ~7.3 when equilibrated with a 95% O$_2$ / 5% CO$_2$ gas mixture.

The intracellular solution for *in vitro* recordings contained 120 mM K-gluconate, 40 mM KCl, 2 mM MgCl$_2$, 2 mM Na$_2$ATP, 10 mM HEPES, 0.1 mM EGTA, and 0.3% biocytin, pH adjusted to 7.28 with KOH. Chemicals were purchased from Merck or Sigma-Aldrich.

2.1.3 Multi-cell patch clamp recordings

Glass micropipettes were fabricated from thick-walled borosilicate tubing (2 mm outer diameter, 1 mm inner diameter) and had open-tip resistances of 3–8 MΩ. They were manually positioned with eight LN mini 25 micromanipulators (Luigs and Neumann) under visual control (Guzman et al., 2016) provided by a modified Olympus BX51 microscope equipped with 60x water-immersion objective (LUMPlan FI/IR, NA = 0.90, Olympus, 2.05 mm working distance) and infrared differential interference contrast video microscopy and epifluorescence. Targeted cell bodies were located ~30–120 μm below the surface of the slice. Interneurons were identified from the tdTomato or EGFP fluorescence in epifluorescence illumination and the AP phenotype upon 1-s current pulses (> 50 Hz in a series of pulses of 100–1,200 pA for PV$^+$ interneurons). Mature GCs were identified by their morphological appearance in the infrared image and from their passive and active membrane properties. Cells with input resistance >

500 MΩ, potentially representing newborn GCs (Schmidt-Hieber et al., 2004), were not included in the analysis. Cells with resting potentials more positive than −55 mV were discarded. In total, the number of successfully recorded cells per recording varied between eight and two. Recording temperature was ~22°C (range: 20–24°C, room temperature) unless specified differently.

Electrical signals were acquired with four two-channel Multiclamp 700B amplifiers (Molecular Devices), low-pass filtered at 6–10 kHz, and digitized at 20 kHz with a Cambridge Electronic Design 1401 mkII AD/DA converter via custom-made stimulation-acquisition scripts using Signal 6.0 software (CED). For current-clamp recordings, pipette capacitance was ~80% compensated, and series resistance was balanced by the bridge circuit of the amplifier; settings were readjusted throughout the experiment when necessary. For voltage-clamp recordings, series resistance was not compensated but repeatedly monitored using 2-mV hyperpolarizing pulses.

To test synaptic connections, a presynaptic neuron was stimulated with a train of five or ten current pulses (2 ms, 1–2 nA) at frequencies of 20 or 50 Hz, while all other neurons were voltage-clamped at −70 mV. A connection was defined as monosynaptic if synaptic currents had latencies < 4.0 ms and peak amplitudes larger than 2.5 times the standard deviation of the baseline of the average trace (computed from 15–30 individual traces). Events with latencies ≥ 4.0 ms were considered polysynaptic.

2.1.4 Data analysis

Recordings were analyzed using Stimfit and Python-based scripts (Guzman et al., 2014). Synaptic latency was measured from the peak of the presynaptic AP to the onset of the postsynaptic potential or current. Kinetic analysis of EPSCs or inhibitory postsynaptic currents (IPSCs) was performed in pairs with a series resistance of < 15 MΩ. Distance was measured from soma center to soma center. Analysis of the axonal arbor of PV$^+$ interneurons and GCs revealed that the axonal length was 2.21 ± 0.20 and 1.59 ± 0.07 times larger than the corresponding intersomatic distance (**Fig. 2.1**). Connection probability was calculated as the number of connected pairs over the total number of tested pairs in each 50-μm distance interval. 95%-confidence intervals were obtained assuming normality. Distance dependence of connectivity was fit with a sigmoidal function $f(x) = A \left[1 + \text{Exp}[(x - B)/C]\right]^{-1}$, where x is absolute distance, and A, B and C are fitted parameters. Throughout the test, the maximal connection probability (c_{max}) was determined as $f(0)$, and the space constant (d_{half}) was determined as the x' value that specified the condition $x = 0.5$. To test whether connectivity differed between synapses, 10,000 bootstrap replications of the inhibitory PV$^+$ interneuron–GC data set were obtained, and the mean values of the GC–PV$^+$ interneuron and PV$^+$ interneuron–PV$^+$ interneuron experimental data sets were compared against the simulated distribution (Efron and Tibshirani, 1998). Values are given as mean ± standard error of the mean (SEM). Box plots show lower quartile (Q1), median (horizontal line), and upper quartile (Q3). The interquartile range (IQR = Q3–Q1) is represented as the height of the box. Whiskers extend to the most extreme data point that is no more than 1.5 x IQR from the edge of the box (Tukey style). Statistical comparisons were made either with a non-parametric Mann-Whitney U two-sided test or by linear regression, testing whether the slope was significantly different from 0.
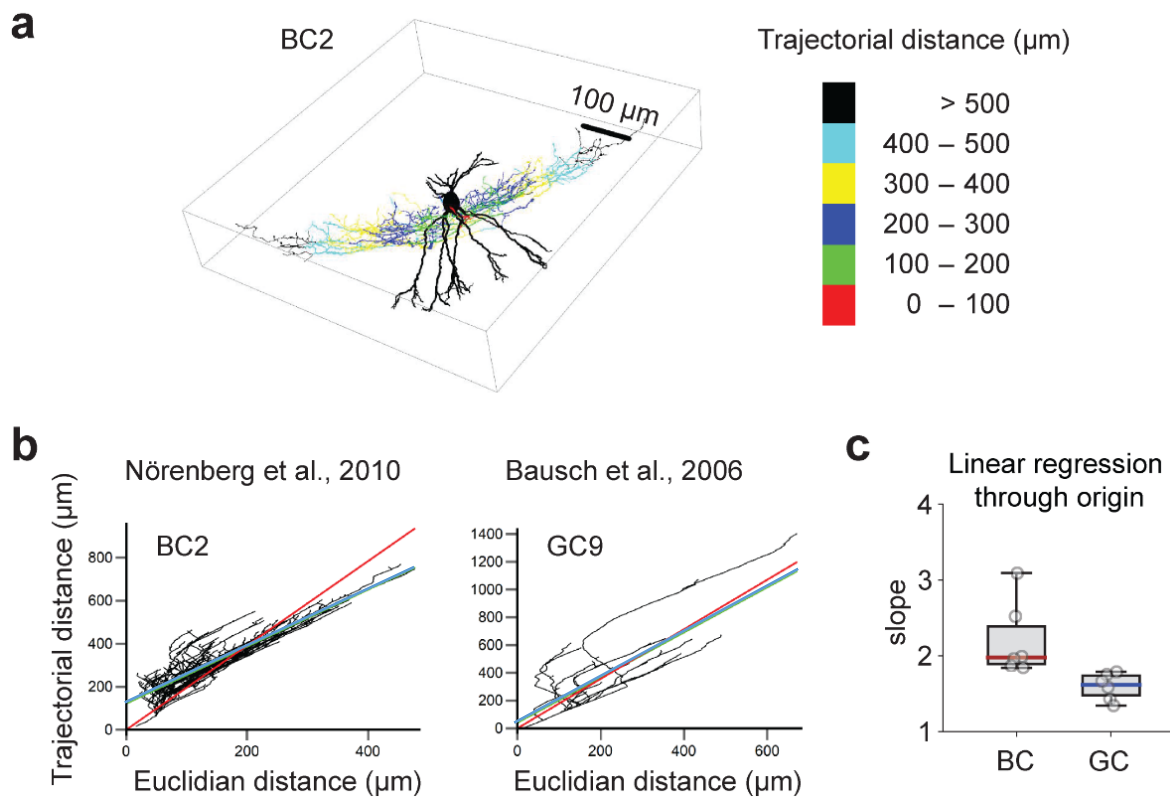
Figure 2.1: **Relation between intersomatic distance and axon length.**
(**a**) Reconstructed fast-spiking dentate gyrus basket cell (BC). Soma and dendrites
are drawn in black, the axon is color-coded according to the length of the axonal path.
Basket cell 2 (BC2) from the sample of Nörenberg et al. (Nörenberg et al., 2010). (**b**)
Plot of axon length (trajectorial distance) against intersomatic distance (Euclidian
distance). Data points were analyzed by regression with linear function through the
origin (red line) or with offset (light blue line). Left, interneuron (BC2) (Nörenberg et
al., 2010); right, GC (Cell number 9) (Bausch et al., 2010). All distance values were
measured relative to the center of the soma. (**c**) Slope of the axon length–
intersomatic distance relation (fit with a line through the origin). Box plots show lower
quartile (Q1), median (horizontal red line), and upper quartile (Q3). The interquartile
range (IQR = Q3–Q1) is represented as the height of the box. Whiskers extend to the
most extreme data point that is no more than 1.5 x IQR from the edge of the box
(Tukey style). Data from individual cells are plotted on top of the corresponding box.
Data from six fast-spiking dentate gyrus BCs (Nörenberg et al., 2010) and six dentate
gyrus GCs (cells number 9, 47, 52, 56, 58, and 61) (Bausch et al., 2010).

To test whether disynaptic motifs (Zhao et al., 2011) occurred significantly more frequently than expected by chance, we simulated the entire set of recording configurations including PV$^+$ interneurons (41 octuples, 62 septuples, 54 sextuples, 37 quintuples, 14 quadruples, 7 triples, and 3 pairs in 218slices) 10,000 times, assuming random connectivity (Erdös and Rényi, 1959; Zhao et al., 2011; Guzman et al., 2016). The connection probabilities were set to the experimentally determined distance-dependence values. For each simulated data set, we counted the number of all 25 possible disynaptic motifs (**Fig. 3.12**). From the 10,000 bootstrap replications, mean, median, and confidence intervals for these counts were determined. *P* values were calculated as the number of replications in which the motif number was equal to or larger than the empirical number, divided by the number of replications. If a motif was never encountered in the 10,000 replications, *P* was assumed as < 0.0001. For assessing statistical significance, correction for multiple testing was performed using a Benjamini–Hochberg method that controls the false discovery rate (Benjamini and Hochberg, 1995). *P* values for m comparisons were sorted in increasing order ($P_1 \leq P_2 \leq \ldots \leq P_m$), the first P_i value that satisfied the condition $P_i \leq i / m$ 0.05 was identified (starting with P_m), and the motifs corresponding to P_j values with $1 \leq j \leq i$ were considered significant. For illustration purposes, *P* values were converted into z scores, using the quantiles of a standard normal distribution.

2.1.5 Morphological analysis

Neurons that were filled with biocytin (0.3%) for > 1 hour were processed for morphological analysis. After withdrawal of the pipettes, resulting in the formation of outside-out patches at the pipette tips, slices were fixed for 12–24 hours at 4°C in a 0.1 M phosphate buffer (PB) solution containing 2.5% paraformaldehyde (PFA), 1.25% glutaraldehyde, and 15% (v/v) saturated picric acid solution. After fixation, slices were treated with hydrogen peroxide (1%, 10 min) to block endogenous peroxidases, and rinsed in PB several times. Membranes were permeabilized with 2% Triton X100 in PB for 1 h. Slices were then transferred to a phosphate-buffered solution containing 1% avidin-biotinylated horseradish peroxidase complex (ABC, Vector Laboratories) and 1% Triton X100 for ~12 hr. Several rinses in PB removed the excess ABC, and the slices were developed with 0.05% 3,3'-diaminobenzidine

tetrahydrochloride and subsequently hydrogen peroxide. Finally, slices were embedded in Mowiol (Sigma-Aldrich).

2.1.6 *In vivo* recordings from dentate gyrus PV$^+$ interneurons

These set of experiments were performed by Xiaomin Zhang. Whole-cell patch-clamp recordings *in vivo* were performed in male 35- to 63-day-old mice as described previously (Pernía-Andrade and Jonas, 2014). Animals were in the head-fixed, fully awake configuration, and were running on a linear belt treadmill (Royer et al., 2012; Bittner et al., 2015). The head-bar implantation and craniotomy were performed under anesthesia by intraperitoneal injection of 80 mg/kg ketamine (Intervet) and 8 mg/kg xylazine (Graeub), followed by local anesthesia with lidocaine. A custom-made steel head-bar was attached to the skull using superglue and dental cement. The day before recording, two small (~0.5 mm in diameter) craniotomies, one for the patch electrode and one for a local field potential (LFP) electrode, were drilled at the following coordinates: 2.0 mm caudal, 1.2 mm lateral for whole-cell recording; 2.5 mm caudal, 1.2 mm lateral for the LFP recording. The dura was left intact, and craniotomies were covered with silicone elastomer (Kwik-Cast, World Precision Instruments). Pipettes were fabricated from borosilicate glass capillaries (1.75 mm outer diameter, 1 mm inner diameter). Long-taper whole-cell patch electrodes (9–12 MΩ) were filled with a solution containing: 130 mM K-gluconate, 2 mM KCl, 2 mM MgCl$_2$, 2 mM Na$_2$ATP, 0.3 mM NaGTP, 10 mM HEPES, 18 mM sucrose, 10 or 0.1 EGTA, and 0.3% biocytin. Whole-cell patch electrodes were advanced through the cortex with 500–600 mbar of pressure to prevent the electrode tip from clogging. After passing the hippocampus CA1 subfield, the pressure was reduced to 20 mbar. After the blind whole-cell recording was obtained, series resistance was calculated by applying a test pulse (+50 mV and −10 mV) under voltage-clamp conditions. Recordings were immediately discarded if series resistance exceeded 70 MΩ. After the bridge balance was compensated, step currents from −100 pA to 400 pA were injected into the cell to calculate the input resistance and maximal firing frequency of the recorded cells. All the recordings were done in current-clamp experiment configuration without holding current injection using a Heka EPC double amplifier. Signals were low-pass filtered at 10 kHz (Bessel) and sampled at 25 kHz with Heka Patchmaster acquisition software. After recording, the patch pipettes were slowly withdrawn to form an outside-out patch,

verifying the integrity of the seal. Data included were obtained from three fast-spiking cells in the dentate gyrus, which generated APs during sustained current injection at a frequency of > 100 Hz. To determine the relative AP threshold, spontaneous action potentials (sAPs) were detected and aligned either at the sAP peak or at the first AP when burst firing occurred. The membrane potential preceding the sAP was measured in a 10–20 ms time window before the sAP. sAP absolute threshold was determined from a dV / dt–V phase plot; the rising phase was fit with an exponential function including a shift factor, and the intersection of the fit curve with the baseline was defined as the threshold.

2.2 Computational methods

2.2.1 Full-size dentate gyrus network model

Simulations of pattern separation were performed using Neuron version 7.5 (Carnevale and Hines, 2006) in combination with Mathematica version 11.2 (Wolfram Research). In essence, the present model provided a neuronal network implementation of a WTA mechanism mediated by lateral inhibition (Majani et al., 1988; de Almeida et al., 2009). The pattern separation network model consists of two layers, the first layer representing the entorhinal cortex, typically with 50,000 entorhinal cortex cells (ECs) and the second layer constituting the dentate gyrus, with 500,000 GCs and 2,500 PV$^+$ interneurons. The EC–GC synapses connected the layers to represent the perforant path input to the dentate gyrus. A WTA mechanism mediated by lateral inhibition was implemented by connecting GCs and INs by excitatory (EI) synapses in one direction and by inhibitory (IE) synapses in the other direction.

Unlike other models (Myers and Scharfman, 2009; Faghihi and Moustafa, 2015), the model was implemented in full-size. The model contained 500,000 GCs, to represent the dentate gyrus of one hemisphere in adult laboratory mice (Amrein et al., 2004) **(Table 1)**. A full-size implementation was necessary first, to increase the realism of the simulations; second to implement measured macroscopic connectivity rules without scaling, and finally, to simulate sparse coding regimes, which were unstable in smaller networks. The model was designed to incorporate the connectivity rules of PV$^+$ interneurons and GCs in the dentate gyrus (**Fig. 3.5**). Other types of interneurons, such as SST$^+$ or CCK$^+$ interneurons were not considered because of their low connectivity (**Fig. 3.4**) and their slower signaling speed (Hu et al., 2014).

Parameter	Meaning	Standard value (range)	References
n_{EC}	number of entorhinal cells (ECs)	50,000 (12,500–200,000)	
n_E	number of granule cells (GCs)	500,000	Amrein et al., 2004
n_I	number of PV[+] interneurons (PV[+] INs)	2,500	
c_{EI}	maximal connection probability EI synapses	0.1[a]	
σ_{EI}	connection width EI synapses	150 µm[b]	
J_{EI}	synaptic strength EI synapses	8 nS[c]	
$\tau_{rise,E}$	EPSC rise time constant	0.1 ms	Geiger et al.,1997
$\tau_{decay,E}$	EPSC decay time constant	1 ms	Geiger et al.,1997
c_{IE}	maximal connection probability IE synapses	0.3[a]	
σ_{IE}	connection width IE synapses	300 µm[b]	
J_{IE}	synaptic strength IE synapses	0.025 (0.005–0.1)[d]	
τ_{IE}	IPSC decay time	10 ms	
c_{II}	maximal connection probability II synapses	0.6	
σ_{II}	connection width II synapses	300 µm[b]	
J_{II}	synaptic strength II synapses	16 nS	
τ_{II}	IPSC decay time constant	2.5 ms	Bartos et al., 2001
$V_{AP,EI}$, $V_{AP,IE}$	axonal AP propagation velocity	0.2 m s^{-1} (0.05–0.8)[e]	Doischer et al., 2008; Hu and Jonas, 2014
J_{gamma}	external inhibitory gamma-frequency drive to GCs	1.0 (0.5–3.5)[d]	de Almeida et al., 2009
c_{gap}	maximal connection probability gap junctions	0.8	
σ_{gap}	connection width gap junctions	150 µm[b]	
R_{gap}	gap junction resistance	300 MΩ	
c_{EC-GC}	maximal connection probability EC–GC synapses	0.2 (0.05–0.1)	Tamamaki and Nojyo, 1993; Witter, 2007
σ_{EC-GC}	connection width EC–GC synapses	500 µm (0.1–infinity)	Tamamaki and Nojyo, 1993; Witter, 2007
α_{EC}	average activity in EC neurons	0.1 (0.02–0.5)	
I_{μ}	amplitude of excitatory drive in E neurons	1.8 (1–2.0)[d]	

Table 1. **Standard parameters for the full-size network model of pattern separation.**
(**a**) For the standard parameter set, the ratio of lateral inhibition over reciprocal inhibition motifs was 6, consistent with the experimental data. (**b**) Space constants refer to a total length of the hippocampal formation of 5 mm. (**c**) Firing threshold of PV$^+$ INs was ~18 nS. (**d**) Unitless, because GCs were modeled as integrate-and-fire (IF) neurons. (**e**) For the standard values of $V_{AP,EI}$, $V_{AP,IE}$ and σ_{EI}, and σ_{IE}, the weighted mean latency is 0.60 ms for EI synapses and 1.20 ms for IE synapses, consistent with experimental observations.
Values in parentheses indicate explored parameter range. EPSC, excitatory postsynaptic current; IPSC, inhibitory postsynaptic current, AP, action potential.

2.2.2 Implementation of neurons

Individual PV$^+$ interneurons were modeled as single-compartment neurons with Wang-Buzsáki-type active conductances (length and diameter 70 µm, C_m = 1.0 µF cm^{-2}, g_{pas} = 0.1 mS cm^{-2}, V_{rest} = −65 mV; (Wang and Buzsáki, 1996). Single neurons were assumed to be cylinders with diameter and length of 70 µm, giving a surface area of 15394 µm^2 and an input resistance of 65 MΩ. Neurons showed a current threshold for AP initiation of 0.039 nA and a fast-spiking, type I action potential phenotype (Ermentrout, 1996), as characteristic for PV$^+$ interneurons **(Fig. 3.2a, 3.6c)**. Individual GCs were modeled as IF spiking neurons, using the IntFire2 class of Neuron; the membrane time constant and synaptic time constant were assumed as 15 ms and 30 ms, respectively.

2.2.3 Implementation of synaptic interconnectivity

Synapses between neurons were placed with distance-dependent probability. Normalized distance was cyclically measured as x = 0.5 − abs[abs[(i/i_{max} − j/j_{max})] − 0.5], where i and j are indices of pre- and postsynaptic neurons, i_{max} and j_{max} are corresponding maximum index values, and abs(r) is the absolute value of the absolute number r. Connection probability was then computed using a Gaussian function as p(x) = $c\ e^{-\frac{x^2}{2\,\sigma^2}}$, where c is maximal connection probability (c_{EI}, c_{IE}, c_{II}, and c_{gap}) and σ is the corresponding standard deviation representing the width of the distribution (σ_{EI}, σ_{IE}, σ_{II}, and σ_{gap}; **Table 1**).

Connection probability between upstream ECs and GCs was computed from a Gaussian function with peak connection probability of 0.02 and a standard deviation of 0.5 mm, to represent the expansion of coding space from the entorhinal cortex to the dentate gyrus (Witter, 2007; Cayco-Gajic et al., 2017). For 50,000 ECs and 500,000 GCs, this corresponds to a convergence of 2,507 and a divergence of 25,066 cells. Binary activity patterns in upstream neurons were then converted into patterns of excitatory drive of GCs. Although this drive was primarily intended to represent input from entorhinal cortex neurons, it may equally represent contributions from other types of excitatory neurons (e.g., mossy cells or CA3 pyramidal cells) (Myers and Scharfman, 2009).

Excitatory GC–interneuron synapses, inhibitory interneuron–GC synapses, and inhibitory interneuron–interneuron synapses were incorporated by random placement of NetCon objects in NEURON (Carnevale and Hines, 2006); gap junctions were implemented by random placement of pairs of point processes. For excitatory GC–interneuron synapses and inhibitory interneuron–interneuron synapses, synaptic events were simulated using the Exp2Syn class of NEURON. For excitatory GC–interneuron synapses, we assumed $\tau_{rise,E}$ = 0.1 ms, $\tau_{decay,E}$ = 1 ms, and a peak conductance of 8 nS. For inhibitory interneuron–interneuron synapses, we chose $\tau_{rise,I}$ = 0.1 ms, $\tau_{decay,I}$ = 2.5 ms, and a peak conductance of 16 nS. For inhibitory interneuron–GC synapses, the synaptic weight was chosen as 0.025 (relative to the threshold, because GCs were modeled as IF neurons). For all chemical synapses, synaptic latency was between 0 and 25 ms according to the distance between pre- and postsynaptic neuron. Gap junction resistance was assumed as 300 MΩ, approximately five times the input resistance of the cell. Synaptic reversal potentials were 0 mV for excitation and −65 mV for inhibition. The maximal length of the hippocampal network was assumed as 5 mm, consistent with anatomical descriptions in mice.

2.2.4 Simulation of network activity and analysis pattern separation

Simulations were performed in four steps (**Fig. 2.2**). First, we computed 100 random binary activity patterns in the ECs. To generate input patterns over a wide range with defined correlations, 100 uncorrelated random vectors a_i of size n_{EC} were computed,

where individual elements were pseudorandom real numbers in a range of 0 to 1 and n_{EC} is the number of ECs. Vectors were transformed into correlated vectors as $r * a_1 + (1 − r) * a_i$, where a_1 is the first random vector and r corresponds to the correlation coefficient. r was varied between 1 and 0.1. Finally, a threshold function $f(x) = H(x − \theta)$ was applied to the vectors, where H is the Heaviside function, and θ is the threshold that determines the activity level in the pattern. Empirically, 100 input patterns were sufficient to continuously cover the chosen range of input correlations. Unless stated differently, the average activity in EC neurons (α_{EC}), i.e. the proportion of spiking cells, was assumed to be 0.1.
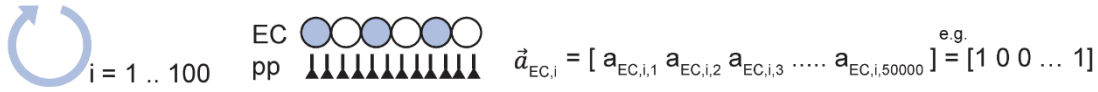
Second, the patterns in the upstream neurons were converted into patterns of excitatory drive in GCs, by multiplying the activity vectors with the previously computed connectivity matrix between ECs and GCs. Unless otherwise indicated, the mean tonic current value was set to 1.8 times the threshold value of the GCs (i.e., $I_\mu = 1.8$; unitless, since GCs were implemented as IF units; **Table 1**). In a subset of simulations (**Fig. 3.14a–c**), the tonic current was replaced by Poisson trains of EPSPs to convey a higher degree of realism. In these simulations, events were simulated by NetStim processes. In another subset of simulations (**Fig. 3.14d–f**), the excitatory tonic drive computed from the EC activity and the EC–GC connectivity was applied in parallel to GCs and INs to implement feedforward inhibition.

Third, we computed the activity of the network for all 100 patterns. Simulations were run with 5 μs fixed time step over a total duration of 50 ms. At the beginning of each simulation, an inhibitory synaptic event of weight 1 (relative to the threshold) was simulated in all GCs to mimic recovery from a preceding gamma cycle (de Almeida et al., 2009). Spikes were detected when membrane potential reached a value of 1 in the GCs and 0 mV in the interneurons. The final result of the computations was a set of 100 binary output vectors.

Finally, Pearson's correlation coefficients were computed for all pairs of patterns ($\binom{100}{2}$ = 4,950 points), at both input (tonic excitatory drive vector) and output level (spike vector) in parallel, and output correlation coefficients (R_{out}) were plotted against input correlation coefficients (R_{in}). Three parameters quantitatively characterized the separation of patterns. (1) The efficacy of pattern separation was quantified by an area-based pattern separation index (ψ), defined as the area between the identity line and the R_{out} versus R_{in} curve, normalized by the area under the identity

line $(\frac{1}{2})$. Thus, $\psi = 2 \int_{x=0}^{1} \big(x - f(x) \big) dx,$ where *f(x)* represents the input-output correlation function. In practice, *f(x)* was determined by fitting a 10th-order polynomial function to the R_{out} versus R_{in} data points. ψ is 1 for perfect separation, and 0 for pattern identity; values < 0 would correspond to pattern completion (Guzman et al., 2016). (2) The reliability of pattern separation (ρ) was quantified by the Pearsson's correlation coefficient of the ranks of all R_{out} versus the ranks of all R_{in} data points. (3) Finally, the gain of pattern separation (γ) was quantified from the maximal slope of the R_{out} versus R_{in} curve. In practice, this value was determined from the first derivative of the 10th-order polynomial function fit to the R_{out} versus R_{in} data points as *f'(x)* for $x \rightarrow$ 1. Thus, the gain factor is >> 1 for efficient pattern separation and 1 for pattern identity.

a **Compute activity pattern in EC neurons (correlated random patterns)**

$i = 1 .. 100$

EC
pp

$\vec{a}_{EC,i} = [\ a_{EC,i,1}\ a_{EC,i,2}\ a_{EC,i,3}\ .....\ a_{EC,i,50000}\ ] \overset{e.g.}{=} [1\ 0\ 0\ ...\ 1]$

b **Compute drive pattern in GCs**

$i = 1 .. 100$

GC

$\vec{d}_{GC,i} = \vec{a}_{EC,i}\ A_{EC-GC}$

$\vec{d}_{GC,i} = [d_{GC,i,1}\ d_{GC,i,2}\ d_{GC,i,3}\ .....\ d_{GC,i,500000}]$

A_{EC-GC}: Connectivity matrix between ECs and GCs
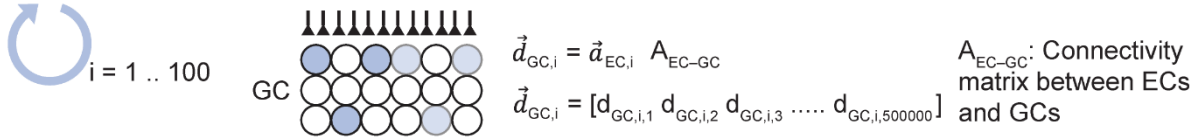
c **Simulate network activity**

$i = 1 .. 100$

GC   PV

$\vec{a}_{GC,i} = [a_{GC,i,1}\ a_{GC,i,2}\ a_{GC,i,3}\ .....\ a_{GC,i,500000}] \overset{e.g.}{=} [1\ 0\ 0\ ...\ 1]$

Gamma input
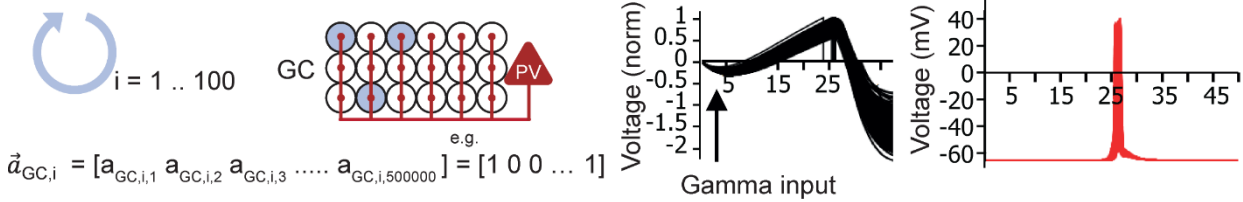
d **Compute pairwise correlations**

$R_{in} = r(\vec{d}_{GC,i}\ \vec{d}_{GC,j})$ $i = 1 .. 100;\ j = 1 .. 100;\ i \neq j$

Patterns

$R_{out}(R_{in}) = f(x)$

$R_{out} = r(\vec{a}_{GC,i}\ \vec{a}_{GC,j})$
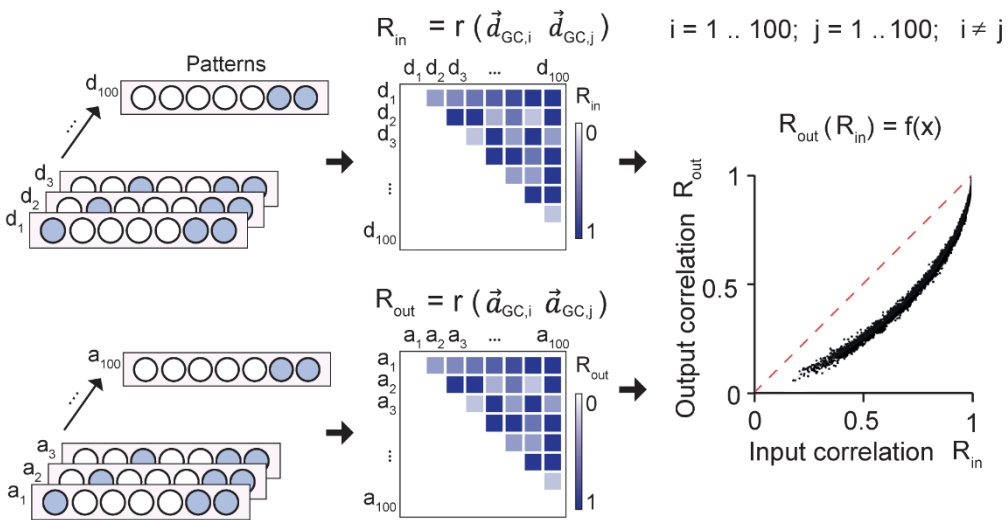
e **Quantify pattern separation**

$\psi = (0.5 - \int_{x=0}^{1} f(x)\ dx)\ /\ 0.5$

Gain of pattern separation, $\gamma = R_{in} \to 1$

39

Figure 2.2: Schematic illustration of full-size network simulations.
(**a**) Computation of activity in upstream neurons. $\vec{a}_{EC,i}$ represents the ith binary activity vector in the entorhinal cortex neurons (50,000 ECs). (**b**) Computation of drive patterns in GCs. $\vec{d}_{GC,i}$ represents the ith drive vector in GCs (500,000 neurons). $\vec{d}_{GC,i}$ was computed as the dot product of $\vec{a}_{EC,I}$, and the connectivity matrix $A_{EC\text{-}GC}$. (**c**) Simulation of network activity in the dentate gyrus. Activity in the full-size network was simulated using NEURON version 7.2. $\vec{a}_{EC,i}$ represents the ith binary spiking vector in GCs, determined by the spiking activity. Interneurons (red) were implemented as a single compartment-based model (2,500 cells). Left,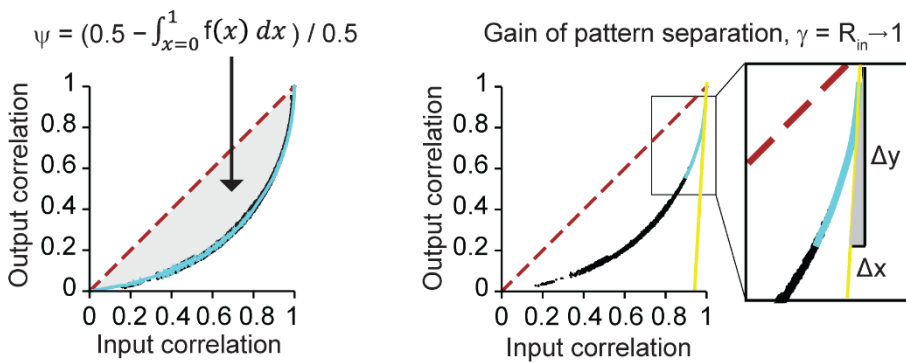 schematic illustration of the model structure. Right, traces of membrane potential of GCs (black) and interneurons (red). Traces from every 1,000[th] GC (500 traces) and every 10th interneuron (250 traces) are superimposed. For PNs, membrane potential is unitless, specified relative to firing threshold. (**d**) Computation of pattern correlation and input-output correlation curves. Correlations R_{in} were computed between pairs of drive vectors, and correlations R_{out} were computed between pairs of activity vectors. Finally, R_{out} and R_{in} values were plotted against each other, and a continuous function *f*(x) was obtained by linear interpolation. (**e**) Quantification of pattern separation. Left, pattern separation index (ψ) was computed as the area (light gray) between the interpolated curve (*f(x)*, blue) and the identity line (red dashed), normalized to the maximal value. Right, the maximal gain of pattern separation γ computed as the slope of the interpolated curve f´(x) for x → 1; yellow line indicates the corresponding tangent.

2.3 Behavioral methods

2.3.1 Pharmacogenetics

Designer Receptors Exclusively Activated by Designer Drugs (DREADD)-based chemogenetics was used for manipulating neural activity *in vivo* (Wiegert et al., 2017). We used an Adeno-associated virus (AAV) encoding hM4Di and the red fluorophore mCherry (AAV$_{dj}$-hSyn-DIO-hM4Di-mCherry) for silencing the activity of PV$^+$ interneurons and AAV carrying only a fluorophore for control experiments (AAV$_{dj}$-hSyn-DIO-mCherry). Bilateral virus injections were performed into the dorsal dentate gyrus of homozygous PV-Cre male mice between postnatal days 30–90 (0.5 µl of AAV, at a flow rate of 60 nl per minute; stereotaxic coordinates from bregma: x = 1,3 mm, y = 1.8 mm, z = 1.9 mm). Anesthesia was delivered by intraperitoneal injection of 160 mg/kg ketamine (Intervet) and 6 mg/kg xylazine. Analgesia during the surgery was provided by subcutaneous injection of Novalgin (Metamizole) (100 mg/kg), and for the post-surgery period, the analgesic Metacam (50 mg/Kg) was used. Throughout the surgery, two small holes were drilled through the parietal bones after exposure of the skull. After the removal of the Hamilton syringe containing the viruses, the head wound was closed with contact adhesive.

For silencing the PV$^+$ interneurons during the behavioral sessions, clozapine-N-oxide (CNO) was administrated by intraperitoneal injection (doses 3 mg/kg) 30 minutes before the behavioral test starts. Because of the potential anxiolytic effects of CNO (Gomez et al., 2017), our controls also received CNO. The specificity of the viruses in targeting interneurons was later confirmed by checking the injection location and the mCherry expression on PV$^+$ interneurons. The specificity of the viruses in silencing the activity PV$^+$ interneurons has been previously confirmed (Xia et al., 2017).

2.3.2 Contextual fear discrimination

For measuring pattern separation in a behavioral task, we used the fear context discrimination task (McHugh et al., 2007; Sahay et al., 2011). To assess the discrimination between very similar environments we used freezing responses, defined as "absence of movement except for respiration" (Curzon et al., 2009). Freezing is a specific response to fear, species-specific that may last for seconds to minutes depending on the strength of the aversive stimulus, the number of presentations, and the degree of learning achieved by the subject" (Curzon et al., 2009).

One week after brain injections, animals were handled by a behavioral experimentalist. This pre-training phase lasted one week, which was immediately followed by the contextual discrimination test. In total 13 mice were blinded tested (8 experiments, 7 control), which had access to food and water *ad libitum*, and lived on a 12:12 hour light/dark cycle. All procedures occurred during the light cycle.

We used two chambers for providing similar contexts. In context A, mice received the foot-shock, while in the context B did not. Importantly, we maintained an identical grid floor (McHugh et al., 2007) while changing the lighting, walls, and odor of the chambers. Previous studies have shown the importance of the floor in the generalization of the fear memories (Huckleberry et al., 2016).

Chamber A: the dimensions were 28 x 21 x 21 cm. Two side walls and ceiling were made of steel while the front door and back wall was made of clear Plexiglas. The floor consisted of 33 stainless steel rods, separated by 6 mm, which were wired to a shock generator and scrambler. The background noise was set at 65 dB. The chamber was lit from above with a house light. A stainless steel pan coated with the acetic acid was placed under the grid floor to provide a distinct odor. Ethanol (70%) was used to clean grids between runs.

Chamber B: the dimensions were 28 x 21 x 21 cm. Black and white strips were covering the side walls. The floor of each chamber consisted of 33 stainless steel rods, separated by 6 mm, which were wired to a shock generator and scrambler. The room

was lit with infrared light. As an olfactory clue, we used rum aroma. A white noise generator provided the 65 dB background noise.

To identify the mice across the experiments, they were tail marked. Each day, mice received an intraperitoneal injection of CNO 30 minutes before starting the test, then mice were transported to an adjacent room to the experimental, and kept undisturbed. The whole set of experiments can be dived in three stages. The first one, during the days 1 to 3 mice experienced the context A, in which after 192 s, they receive a single foot-shock (2 s; 0.65 mA) and after one minute following foot-shock termination, they were removed from the chambers (total session time: ~4 minutes). During the second stage, the days 4 and 5, mice were placed in a counterbalanced order either into the context A or B. No foot-shock was delivered (total session time: 8 minutes). The last experimental phase took place during the days 6 to 17, in which daily, mice experienced both contexts separated in a morning and afternoon session. The exposure order was day 6 BA, day 7 AB, day 8 AB, day 9 BA, day 10 BA, day 11 AB. For the remaining days, the order of the context exposition was reversed. Across this entire discrimination phase, all animals receive a single foot-shock in context A, while never was delivered during context B exposures. Mouse behavior was recorded by digital video cameras mounted above the conditioning chamber. FreezeFrame and FreezeView software (Actimetrics) were used for recording and analyzing freezing behavior, respectively. The freezing score was measured during the first 192 s (pre-shock) in each context on each day. Discrimination ratios were calculated for using these freezing percentage scores according to the following formula: $Freezing_{Chamber\ A}/(Freezing_{Chamber\ A} + Freezing_{Chamber\ B})$

Conntextual fear conditioning using similar contexts
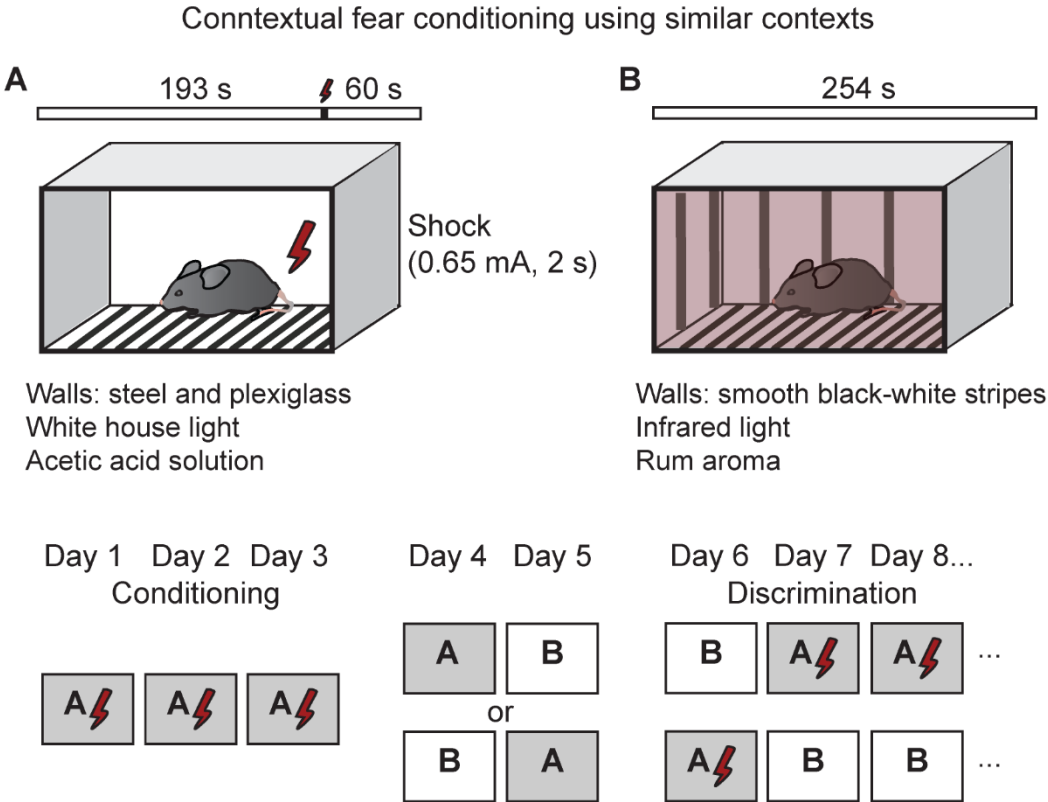
Figure 2.3: Schematic illustration of contextual fear conditioning.
Top, two contexts were used. Context A consisted of a chamber with walls made of steel and clear plexiglass, enlightened from the ceiling with white light. The animals received a 2 s foot-shock after 193 s of exploration. Context B had an identical grid floor to chamber A but had different walls, lighting and olfactory clues. Bottom, the configuration of the experimental protocol. Three consecutive days were used for conditioning mice to the chamber A. Next, mice were exposed either the context AB or BA, where generalization took place. Discrimination between contexts was measured starting from day 6, while mice experienced both contexts within a day in a morning and afternoon session.

44

Chapter 3
RESULTS

3.1 Experimental results

3.1.1 Octuple recordings from granule cells and GABAergic interneurons in the dentate gyrus.

To determine the functional connectivity rules between PNs and INs in the dentate gyrus, we performed simultaneous whole-cell recordings from up to eight neurons (up to seven GCs and up to four interneurons) (**Fig. 3.1**). PV$^+$, SST$^+$, and CCK$^+$ interneurons were identified in genetically modified mice obtained by crossing Cre or Flp recombinase-expressing lines with tdTomato or EGFP reporter lines. PV$^+$ interneurons showed the characteristic fast-spiking AP phenotype during sustained current injection, whereas both SST$^+$ and CCK$^+$ interneurons generated APs with lower frequency, corroborating the reliability of the genetic labeling (**Fig. 3.2**).

To probe synaptic connectivity, we stimulated presynaptic neurons under current-clamp conditions and recorded EPSCs or IPSCs in postsynaptic neurons in voltage-clamp configuration (**Fig. 3.1, 3.3**). In total, we tested 9,098 possible connections in 50 octuples, 72 septuples, 68 sextuples, 48 quintuples, 17 quadruples, 10 triples, and 5 pairs in 270 slices. Interestingly, PV$^+$ interneurons showed much higher connectivity than both SST$^+$ and CCK$^+$ interneurons. For GC–PV$^+$ interneuron pairs with intersomatic distance ≤ 100 μm, the mean connection probability was 11.0% for excitation and 28.8% for inhibition (**Fig. 3.4**). In contrast, for both SST$^+$ interneurons and CCK$^+$ interneurons, the mean connection probability was substantially lower (1.4 and 2.8% for SST$^+$ interneurons, 1.2 and 12.1% for CCK$^+$ interneurons; **Fig. 3.4**). Excitatory interactions between GCs were completely absent, and disynaptic inhibitory interactions (Miles, 1990; Jouhanneau et al., 2018) were extremely sparse (0.124%). These results indicate that in the dentate gyrus PV$^+$ interneurons show markedly higher connectivity than SST$^+$ and CCK$^+$ interneurons, extending previous results obtained *in vivo* in the neocortex (Pala and Petersen, 2015). As PV$^+$ interneurons

showed the highest input and output connectivity, we focused our functional connectivity analysis on these interneurons.
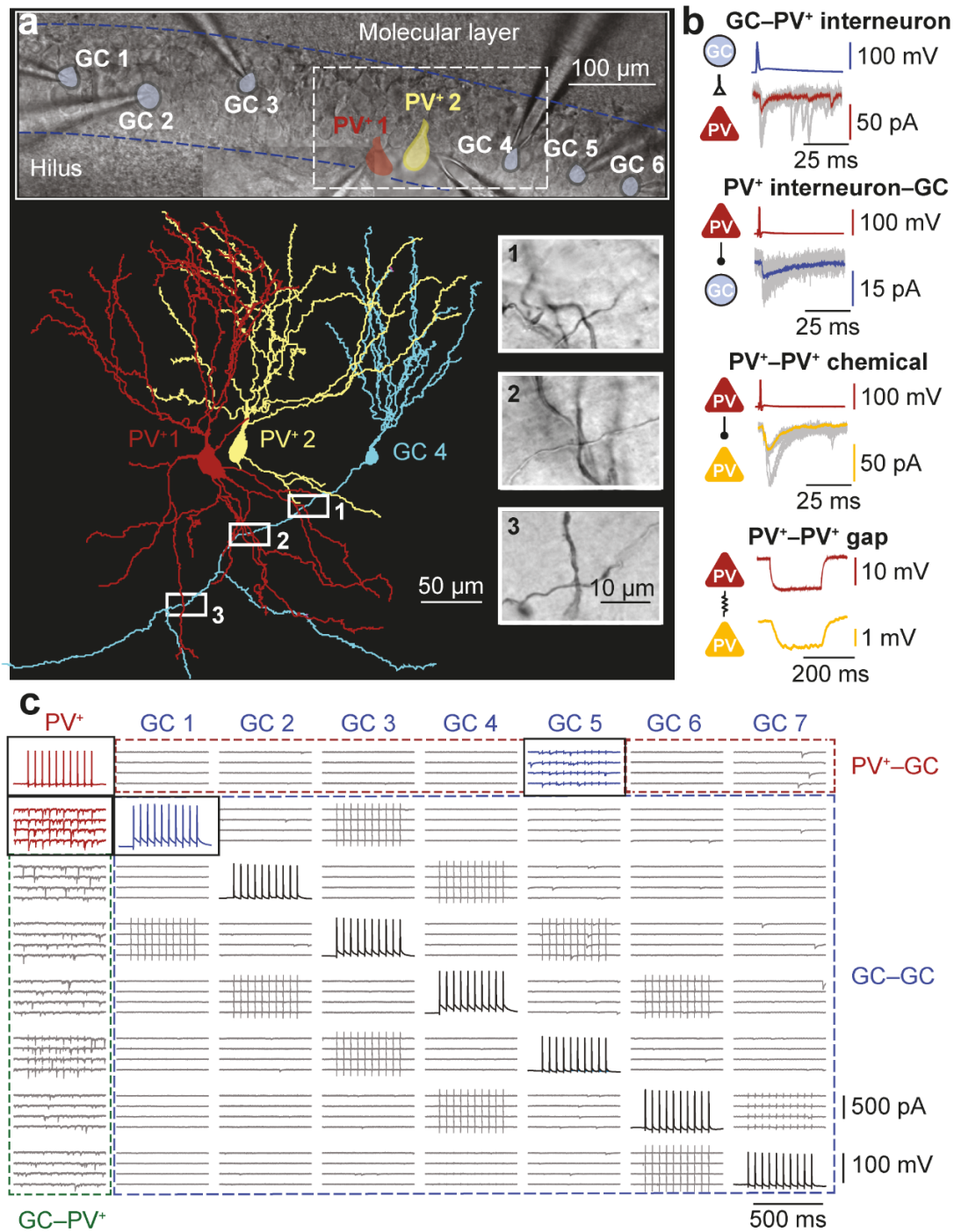
Figure 3.1: Experimental analysis of synaptic mechanisms of pattern separation in the dentate gyrus.

(**a**) Top, infrared differential interference contrast video micrograph of the dentate gyrus in a 300-μm slice preparation, with eight recording pipettes. Shaded areas represent the 2D projections of cell bodies (light blue, GCs; red and yellow, PV⁺ interneurons). Blue dashed lines, boundaries of GC layer. Bottom, partial reconstruction of one GCs and two PV⁺ interneurons. For clarity, only the somatodendritic domains were drawn for the PV⁺ interneurons. Insets, biocytin-labeled putative synaptic contacts, corresponding to boxes in main figure. Data in (a) and (b) from same recording. (**b**) Coexistence of different synapses in an octuple recording (seven cells successfully recorded) containing two PV⁺ interneurons and five GCs. In this recording, an excitatory GC–PV⁺ interneuron connection, an inhibitory PV⁺ interneuron–GC connection, a chemical inhibitory connection between the PV⁺ interneurons, and an electrical connection between the PV⁺ interneurons were found (from top to bottom). (**c**) Connectivity matrix of an octuple recording (all eight cells successfully recorded). Rows represent the presynaptic and columns the postsynaptic cells. In this example, 56 connections were tested; 7 excitatory GC–PV⁺ interneuron connections, 7 inhibitory PV⁺ interneuron–GC connections, and 42 connections between GCs. In this octuple recording, an inhibitory synaptic connection was identified between the PV⁺ interneuron (red) and GC5 (blue) and an excitatory synaptic connection was found between GC1 (blue) and the PV⁺ interneuron (red). The presence of a unidirectional excitatory GC–PV⁺ interneuron connection and a unidirectional inhibitory PV⁺ interneuron–GC connection documents the existence of lateral inhibition in this recording.
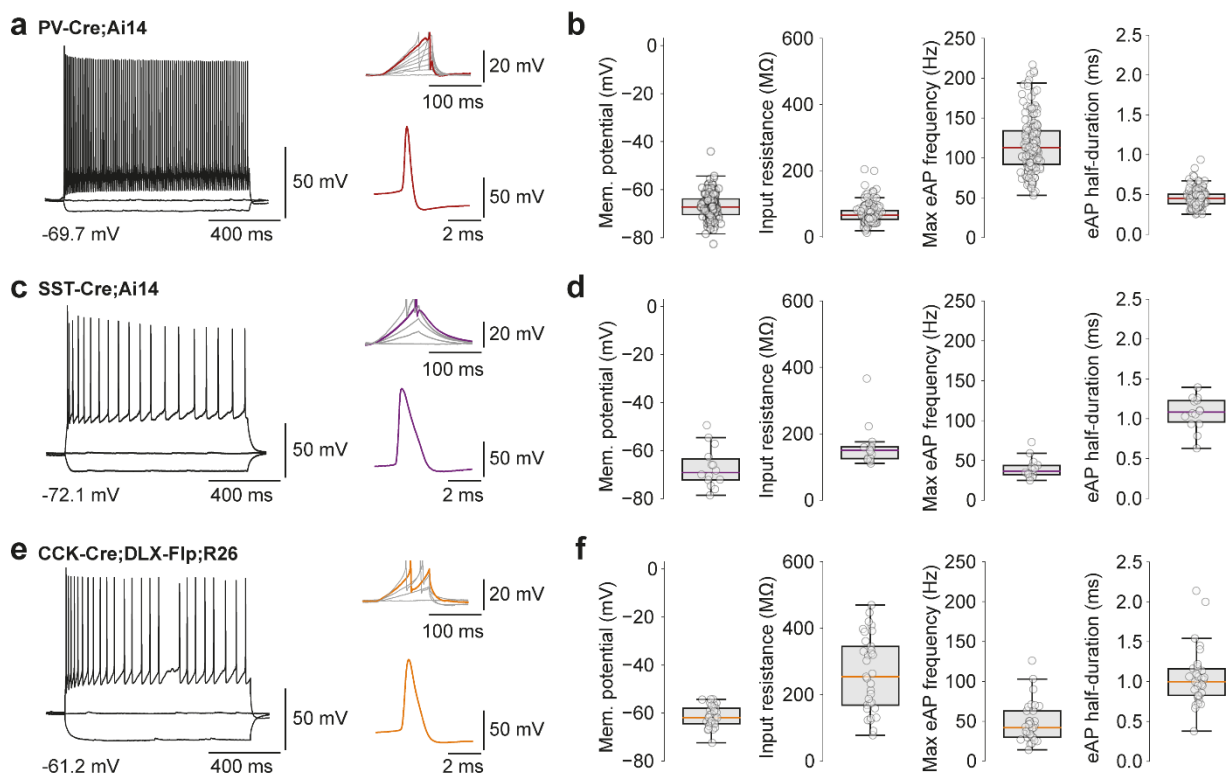
Figure 3.2: Action potential phenotype and membrane properties of different types of genetically identified interneurons in the dentate gyrus.
(**a**) Functional properties of identified PV$^+$ interneurons in the dentate gyrus. Left, voltage changes evoked by long depolarizing and hyperpolarizing current pulses (0.6, 0, and −0.1 nA) applied to the PV$^+$ interneuron. Fast-spiking phenotype (> 100 Hz) and low input resistance (< 100 MΩ) are characteristic. Right, single AP waveform evoked by a depolarizing current ramp. (**b**) Box plots of resting membrane potential (mean, −66.9 mV), input resistance (70.2 MΩ), maximal evoked AP frequency (116 Hz), and evoked AP half-duration (0.45 ms; 173 cells). PV$^+$ interneurons were identified in slices based on tdTomato labeling in PV-Cre;Ai14 mice. (**c, d**) Similar data as in (a, b), but for SST$^+$ interneurons. SST-Cre mice were used for labeling. (**e, f**) Similar data as in (a, b), but for CCK$^+$ interneurons. CCK-Cre;DLX 5/6-Flp mice were used for labeling. In (c, e), voltage changes were evoked by long depolarizing and hyperpolarizing current pulses (0.3, 0, and −0.1 nA). Box plots in (b, d, and f) show lower quartile (Q1), median (horizontal red line), and upper quartile (Q3). The interquartile range (IQR = Q3–Q1) is represented as the height of the box. Whiskers extend to the most extreme data point that is no more than 1.5 x IQR from the edge of the box (Tukey style). Data from individual cells are plotted on top of the corresponding box.
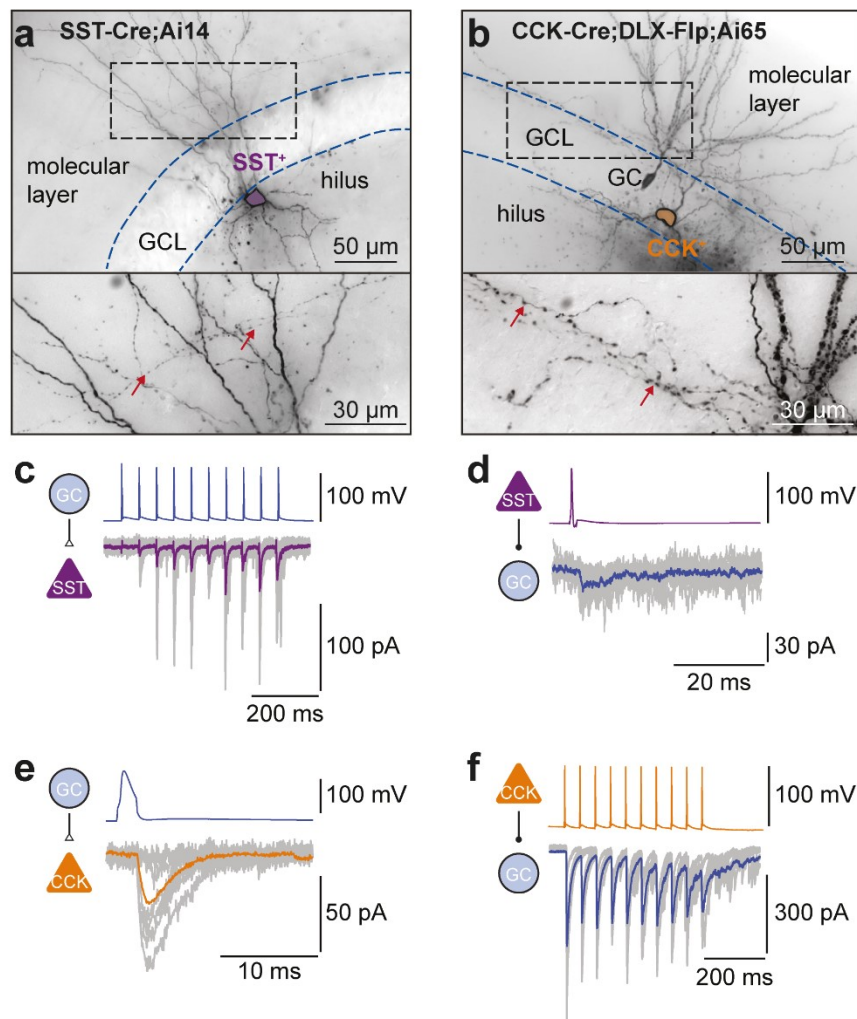
Figure 3.3: Synaptic connections of SST⁺ and CCK⁺ interneurons.
(**a**) Light micrograph of a SST⁺ interneuron filled with biocytin during recording, and visualized using 3,3′-diaminobenzidine as chromogen. Cells were identified by genetic labeling in SST-Cre mice. Axon branches in the molecular layer (red arrows) suggest that the cell was a HIPP or TML interneuron (Han et al., 1993; Hosp et al., 2014). GCL, granule cell layer. (**b**) Light micrograph of a CCK⁺ interneuron filled with biocytin. Cells were identified by genetic labeling in CCK-Cre;DLX 5/6-Flp mice. Axon branches in the inner molecular layer (red arrows) suggest that the cell was a HICAP interneuron (Han et al., 1993; Hefft and Jonas, 2005; Hosp et al., 2014). (**c, d**) Excitatory and inhibitory connectivity of SST⁺ interneurons. GC–SST⁺ interneuron unitary EPSCs are shown in (c), SST⁺ interneuron–GC IPSCs are illustrated in (d). Individual synaptic responses (gray) and average trace (magenta or blue, 15 traces) are shown overlaid. Note the facilitation of EPSCs during train stimulation in (c). (**e, f**) Excitatory and inhibitory connectivity of CCK⁺ interneurons. GC–CCK⁺ interneuron EPSCs are shown in (e), CCK⁺ interneuron–GC IPSCs are illustrated in (f). Note the asynchronous release during and after train stimulation in (f), which is highly characteristic of CCK⁺ interneuron output synapses (Hefft and Jonas, 2005).
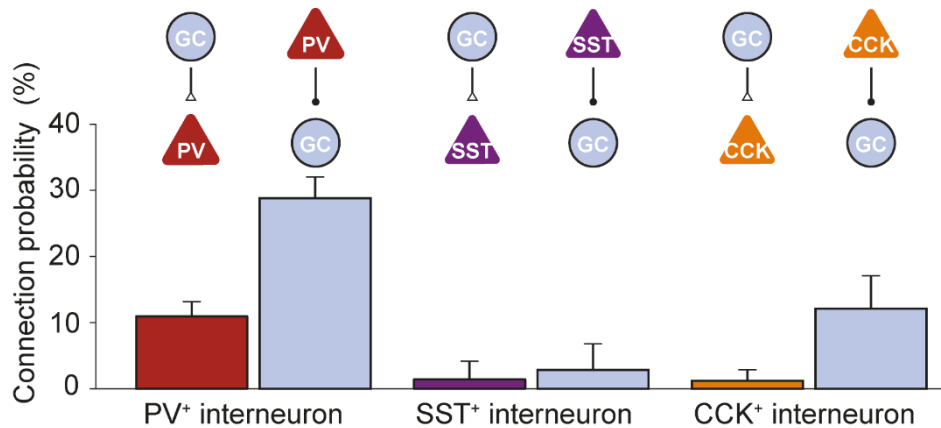
Figure 3.4: Hypoconnectivity of SST⁺ and CCK⁺ interneurons in comparison to PV⁺ interneurons.
Comparison of average connection probability for pairs with an intersomatic distance of ≤ 100 μm. Whereas PV⁺ interneurons were highly connected, SST⁺ and CCK⁺ interneurons showed markedly lower excitatory and inhibitory connectivity (number of tested connections 767, 71, and 165). Error bars represent 95%-confidence intervals estimated from a binomial distribution.

3.1.2 Connectivity rules for excitatory inputs of PV+ interneurons

A WTA mechanism mediated by recurrent inhibition requires sufficient excitatory connectivity of PV+ interneurons and sufficient strength of unitary synaptic inputs. To test these predictions, we examined the functional connectivity rules for PV+ interneuron excitatory input by measuring EPSCs (**Fig. 3.5a–c**). We found that PV+ interneurons were highly and locally connected to GCs. The connection probability showed a peak of 11.3%, and steeply declined as a function of intersomatic distance, with a space constant of 144 μm (**Fig. 3.5b**). In contrast, the EPSC peak amplitude showed no significant distance dependence (**Fig 3.5c**). To determine the efficacy of unitary GC–PV+ interneuron connections, we measured unitary excitatory postsynaptic potentials (EPSPs). Unitary EPSPs had a mean peak amplitude of 1.79 ± 0.3 mV (range: 0.30 to 7.16 mV; **Fig. 3.6a, b**); (Miles, 1990; Scharfman et al., 1990; Geiger et al., 1997). To assess the efficacy of these events in triggering spikes in the presence of ongoing synaptic activity from multiple sources, we performed *in vivo* whole-cell recordings from fast-spiking interneurons in the dentate gyrus in awake mice running on a linear treadmill (**Fig. 3.6c–g**). Under *in vivo* conditions, the difference between baseline membrane potential and threshold was 10.3 ± 1.8 mV (3 *in vivo* recordings from fast-spiking interneurons in dentate gyrus). Thus, although the largest unitary EPSPs were close to the threshold of AP initiation, they were insufficient to trigger a spike. However, the high focal GC–PV+ interneuron connectivity (**Fig. 3.5b**) may ensure activation of PV+ interneurons by spatial summation.
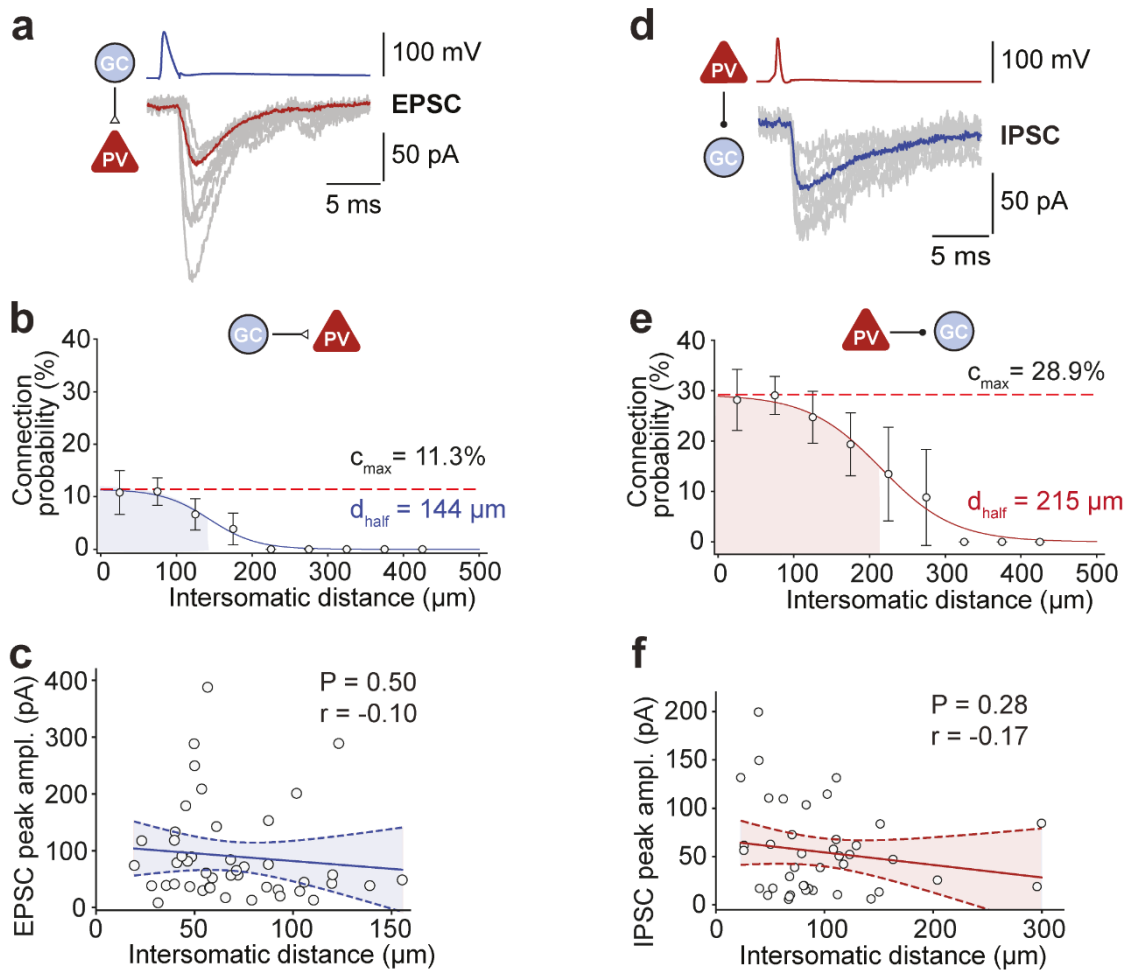
Figure 3.5: Rules of excitatory and inhibitory connectivity in GC–PV+ interneuron networks.
(**a–c**) Rules of GC–PV+ interneuron synapses in the dentate gyrus. (a) Unitary excitatory postsynaptic currents (EPSCs), with individual synaptic responses (gray) and average trace (red, 15 traces) in a representative GC–PV+ interneuron pair. (b) GC–PV+ interneuron connection probability plotted versus intersomatic distance. Connection probability was determined as the ratio of the number of found connections over that of all possible connections in a given distance range. Error bars represent 95%-confidence intervals estimated from a binomial distribution. Data points were fit with a sigmoidal function; shaded area indicates the distance width in which connection probability decayed to half-maximal value (space constant). Red dashed line, maximal connection probability. Maximal connection probability (c_{max}) was 11.3%, and space constant (d_{half}) was 144 µm. (c) Peak amplitude of unitary EPSCs at GC–PV+ interneuron synapses, plotted against intersomatic distance. Data points were fit by linear regression; dashed lines indicate 95%-confidence intervals. (**d–f**) Similar plots as shown in (a–c), but for inhibitory PV+ interneuron–GC synapses. Maximal connection probability was 28.9%, and space constant was 215 µm.

The high local connectivity allowed us to examine the rules of spatial summation of converging inputs (**Fig 3.7**; 9 connections with 2 converging inputs; 4 connections with 3 converging inputs). Summation of EPSPs was largely linear. On average, the summation factor was 1.007 ± 0.017 for two inputs and 1.160 ± 0.167 for three inputs, not significantly different from unity (P = 0.77 and P= 0.14; **Fig. 3.7c**). Furthermore, comparison of peak amplitudes of summated EPSPs evoked by simultaneous stimulation of converging inputs with the AP threshold in fast-spiking interneurons in the dentate gyrus in awake, behaving mice indicated that, on average, ~6 GCs need to be active to trigger APs in PV$^+$ interneurons (6.4; range 5.8–7.5 GCs; **Fig. 3.7d**). Thus, PV$^+$ interneurons in the dentate gyrus operate as coincidence detectors, sensing the synchronous activity of small local clusters of GCs.
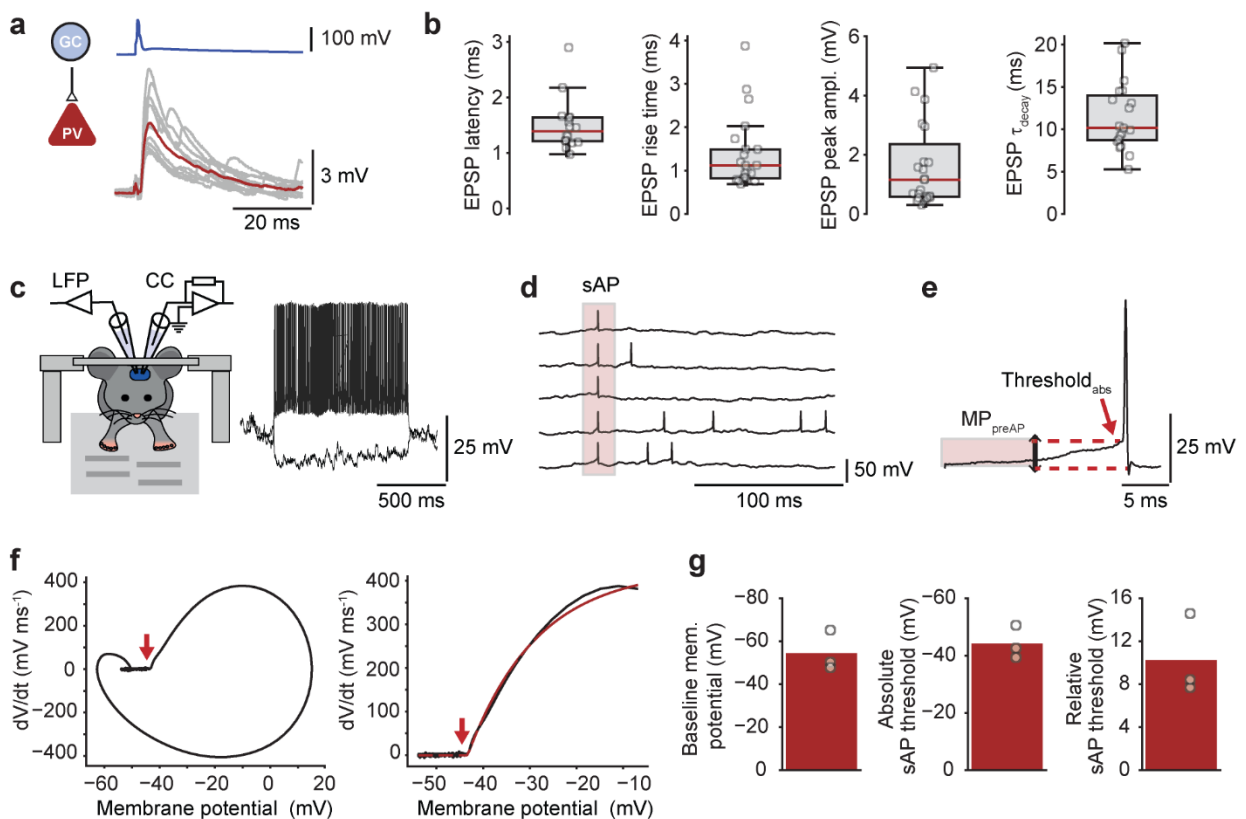
Figure 3.6: Coactivation of converging inputs from granule cells is required to initiate APs in PV⁺ interneurons.

(**a**) Unitary excitatory postsynaptic potentials (EPSPs), with individual synaptic responses (gray) and average trace (red, 15 traces) in a representative GC–PV⁺ interneuron pair. (**b**) Box plots of EPSP latency, 20–80% rise time, peak amplitude, and decay time constant. (**c**) AP properties of fast-spiking interneurons in the dentate gyrus *in vivo* in awake, behaving animals. Right, traces of membrane potential in response to depolarizing and hyperpolarizing current injections. (**d, e**) Superposition of five spontaneous APs (sAPs) aligned to the sAP peak (d) and expanded plot of a single AP (e). Light red area shows the time interval in which the baseline membrane potential before the spike was determined. (**f**) Left, phase plot analysis of the AP shown in (e). Right, fit of the rising component of the phase plot by an exponential function including a shift factor (red curve). Red arrows indicate the absolute threshold of sAP initiation determined from the shift. (**g**) Summary bar graph of baseline membrane potential (in time window 10–20 ms before the AP, left), absolute sAP threshold (center), and relative sAP threshold (relative threshold = absolute threshold – baseline membrane potential). LFP: local field potential; CC: current clamp; Threshold$_{abs}$: absolute threshold; MP$_{preAP}$: baseline membrane potential previous to an AP.
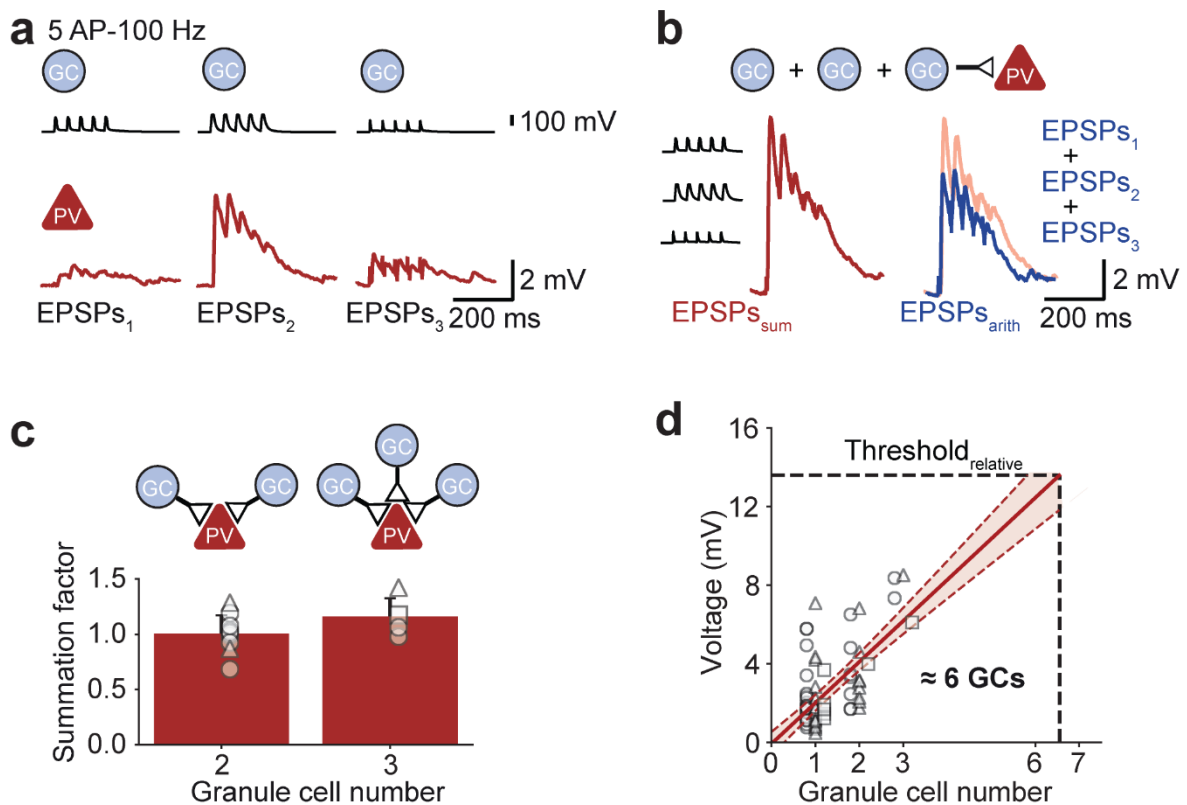
Figure 3.7: Spatial summation of granule cell inputs in PV⁺ interneurons.

(**a, b**) Convergence of three presynaptic GCs (blue) projecting to the same PV⁺ interneuron (red). Responses to trains of APs when individual GCs were stimulated in isolation (a) and when all individual GCs were stimulated together (b). When presynaptic neurons were stimulated together, synaptic responses summated slightly supralinearly in this example, indicated by the slightly larger response following joint stimulation (red trace) in comparison to the arithmetic sum following individual

stimulation (blue trace). (**c**) Summation factor for simultaneous stimulation of 2 or 3 inputs. Peak amplitude of EPSPs evoked by joint stimulation of 2 or 3 inputs over the arithmetic sum of individual EPSPs (summation factor). Circles, 50 Hz (9 multi-cell recordings); triangles, 100 Hz (3 recordings); squares, 200 Hz (1 recording). Data from 9 and 4 multi-cell recordings; 9 recordings with 50 Hz, 3 with 100 Hz, and 1 with 200 Hz stimulation frequency. Note that the summation factor was close to 1, suggesting that summation was largely linear. (**d**) Summated voltage signals induced by a different number (1 to 3) of simultaneous GCs firing. Extrapolation by linear regression of the voltage responses allowed us to predict that ~6 GC inputs (range: 5.8–7.5) were necessary to evoke an AP in a PV$^+$ interneuron (horizontal dashed lines indicates relative threshold from *in vivo* experiments showed in **Fig. 3.6g**).

3.1.3 Connectivity rules for inhibitory outputs of PV$^+$ interneurons

Next, we examined the functional connectivity rules for PV$^+$ interneuron inhibitory output by measuring IPSCs (**Fig 3.5d–f**). Similar to excitatory GC–PV$^+$ interneuron connectivity, inhibitory PV$^+$ interneuron–GC connectivity was distance-dependent (**Fig. 3.5e**). However, maximal connection probability was higher (28.9%) and the width of connectivity was wider (215 µm) than that of excitation. Bootstrap analysis revealed that both maximal connection, and space constant were significantly shorter for excitatory GC–PV$^+$ interneuron synapses than for inhibitory PV$^+$ interneuron–GC synapses ($P < 0.0001$ and $P = 0.0042$, respectively; **Fig. 3.8a**). Thus, different connectivity rules apply for excitatory and inhibitory GC–PV$^+$ interneuron connections (focal excitation versus broad inhibition).

To compare the connectivity rules in the dentate gyrus with those in other brain regions, we quantified the ratio of excitatory to inhibitory connection probability. We found that inhibition was much more abundant than excitation, with a connection probability ratio of 3.83, substantially higher than in other brain areas (**Table 2**). Furthermore, we quantified the abundance of lateral and recurrent motifs in pairs of neurons. In our total sample of 1,301 GC–PV$^+$ interneuron pairs, we found 296 unidirectional inhibitory connections, but only 32 bidirectional connections (**Fig. 3.8b**). Thus, the ratio of lateral inhibition to recurrent inhibition was 9.25, substantially higher than in other circuits (**Table 2**). These results indicate that connectivity rules of PV$^+$ interneurons in the dentate gyrus are unique in comparison to other previously examined circuits.
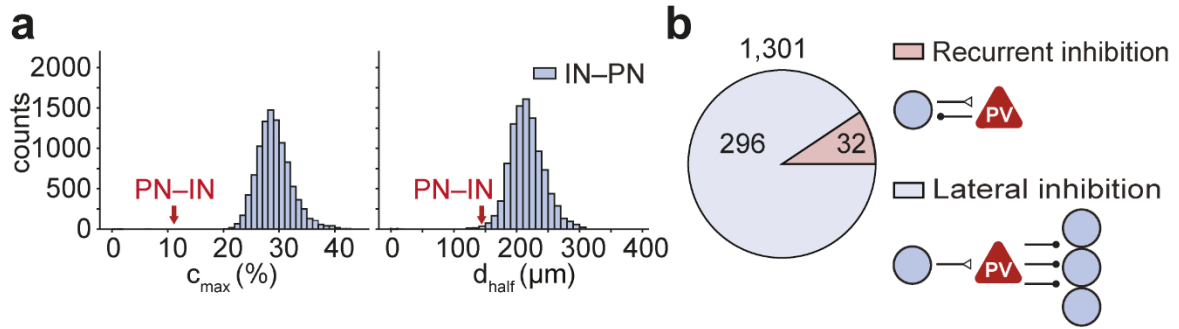
Figure 3.8: Predominant lateral inhibition in the dentate gyrus.
(**a**) Bootstrap analysis of maximal connection probability and space constant. Histograms indicate distributions of c_{max} (left) and d_{half} (right) for 10,000 bootstrap replications of the inhibitory PV$^+$ interneuron–GC connections (**Fig. 3.5**). Red arrows indicate experimental mean values for GC–PV$^+$ interneuron synapses. (**b**) Number of reciprocally coupled GC–PV$^+$ interneuron pairs (excitatory and inhibitory synapse; "recurrent inhibition motif") and unidirectionally coupled PV$^+$ interneuron–GC pairs (inhibitory synapse only; "lateral inhibition motif"). Note that the number of lateral inhibition motifs was almost 10-times higher than that of recurrent inhibition motifs, demonstrating the high abundance of lateral inhibition in the dentate gyrus microcircuit.

Brain region	p_{IE} / p_{EI}[a]	$n_{lateral}$ / $n_{recurrent}$[b]	Reference
Visual and somatosensory cortex	0.99	0.13	Holmgren et al., 2003
Visual cortex	2.5	2.0	Yoshimura and Callaway, 2005
Presubiculum superficial	1.04	1.3	Peng et al., 2017
Presubiculum deep	0.68	0.67	Peng et al., 2017
Entorhinal cortex	1.5	1.1	Couey et al., 2013
Dentate gyrus	3.7	10.0	This work

Table 2: Abundance of lateral inhibition in different brain regions.
(**a**) p_{IE} / p_{EI} indicates the ratio of mean inhibitory IN–PN to mean excitatory PN–IN connection probability. (**b**) $n_{lateral}$ / $n_{recurrent}$ represents the ratio of the number of lateral inhibition motifs and recurrent inhibition motifs in all recorded PN–IN pairs.

3.1.4 Connectivity rules for mutual inhibition of PV$^+$ interneurons

Then, we analyzed the functional connectivity rules for synapses between interneurons (**Fig. 3.9**). Chemical inhibitory synapses between PV$^+$ interneurons showed a connectivity pattern that was more focal than that of inhibitory PV$^+$ interneuron–GC synapses (**Fig. 3.9a, b**). Likewise, electrical synapses between PV$^+$ interneurons (Galarreta and Hestrin, 1999, 2001; Bartos et al., 2001) showed a focal innervation pattern (**Fig. 3.9c, d**). Bootstrap analysis revealed that maximal connectivity was significantly higher, while the space constant was significantly shorter for inhibitory PV$^+$–PV$^+$ interneuron synapses than for PV$^+$ interneuron–GC synapses (P = 0.0001 and P = 0.0036 respectively). Furthermore, recordings from GCs and multiple PV$^+$ interneurons provided direct evidence for the suggestion (Galarreta and Hestrin, 1999) that EPSPs propagate through gap junctions, although the peak amplitude is markedly attenuated (**Fig. 3.10**). Taken together these results indicate that connectivity rules in PN–IN microcircuits are synapse-specific. Different connectivity rules apply to excitatory and inhibitory synapses between PNs and INs (GC–PV$^+$ versus PV$^+$–GC), and to inhibitory synapses terminating on different postsynaptic target cells (PV$^+$–GC versus PV$^+$–PV$^+$ synapses).
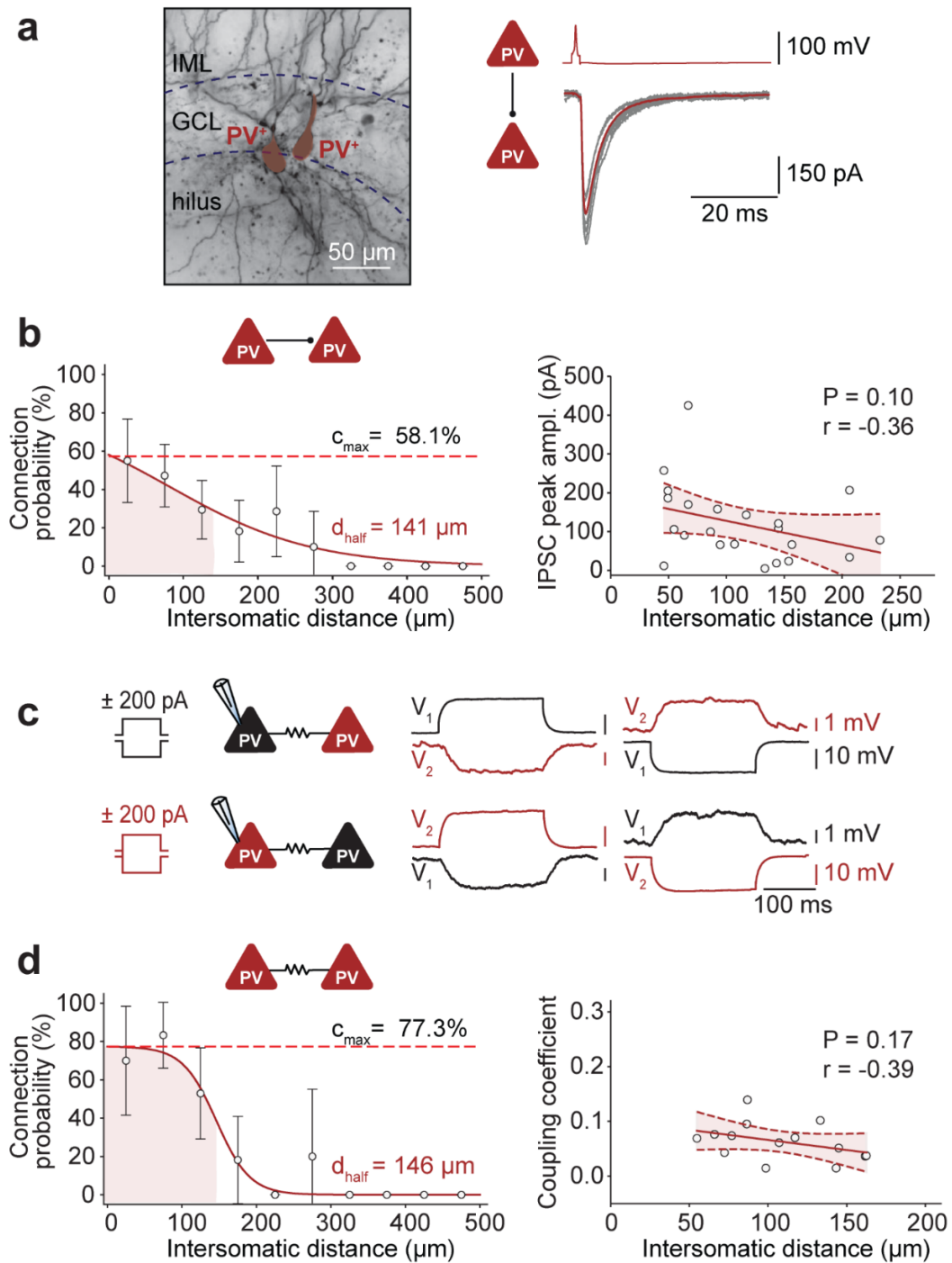
Figure 3.9: Connectivity rules for chemical and electrical connections between PV⁺ interneurons.

(**a**) Left, light micrograph of a biocytin-labeled PV⁺ interneuron–PV⁺ interneuron pair. Right, unitary inhibitory postsynaptic currents (IPSCs), with individual synaptic responses (gray) and average trace (red, 15 traces) in the same pair. (**b**) PV⁺ interneuron–PV⁺ interneuron chemical connection probability (left) and IPSC peak amplitude (right) plotted versus intersomatic distance. Connection probability data points were fit with a sigmoidal function; IPSC amplitude data were analyzed by linear regression. Maximal connection probability was 58.1%, and space constant was 141 µm. (**c**) Electrical coupling between two PV⁺ interneurons. Voltage changes in the pre- and postsynaptic cell caused by the injections of long polarizing current pulses (left, +200 pA; right, −200 pA; 200 ms) in one of the coupled cells. (**d**) PV⁺ interneuron–PV⁺ interneuron electrical connection probability (left) and coupling coefficient (right) plotted versus intersomatic distance. Maximal connection probability was 77.3%, and space constant was 146 µm. The coupling coefficient (CC) was calculated as the mean ratio of steady-state voltages (V_2 / V_1, V_1 / V_2) during application of current pulses in one of the cells (cell 1 and cell 2, respectively).

58

Figure 3.10: Propagation of evoked EPSPs in PV⁺ interneuron networks via gap junctions.
(**a**) Simultaneous recording from a GC and two PV⁺ interneurons. APs in the GC led to monosynaptic EPSPs (current-clamp conditions) or EPSCs (voltage-clamp conditions) in the first PV⁺ interneuron. (**b**) The two recorded PV⁺ interneurons were couples by gap junctions. (**c**) Propagation of EPSPs from PV⁺ interneuron 1 (red) to PV⁺ interneuron 2 (black). APs in the GC led to EPSCs with peak amplitude < 5 pA in the second PV⁺ interneuron. These excitatory synaptic events were apparently propagated via gap junctions (Galarreta and Hestrin, 1999).

Finally, to validate our distance-dependence measurements (**Fig. 3.5**), we further included a second method for analyzing connection probabilities across the dentate gyrus while considering the anatomy of the whole structure. Specifically, we measured the distance-dependence of the connectivity of a subset of pairs (GC–PV⁺ interneuron and PV⁺–PV⁺ interneuron pairs) taking into account that GCs are tightly packed forming a "c-shaped structure" (**Fig. 3.11**). These results were comparable to the one obtained with the tip-to-tip somatic assessments (**Fig. 3.5b, e and 3.9b**). Thus, together to the axon length analysis (**Fig. 2.1**), we further validate the measurements of our probabilistic distance connectivity.
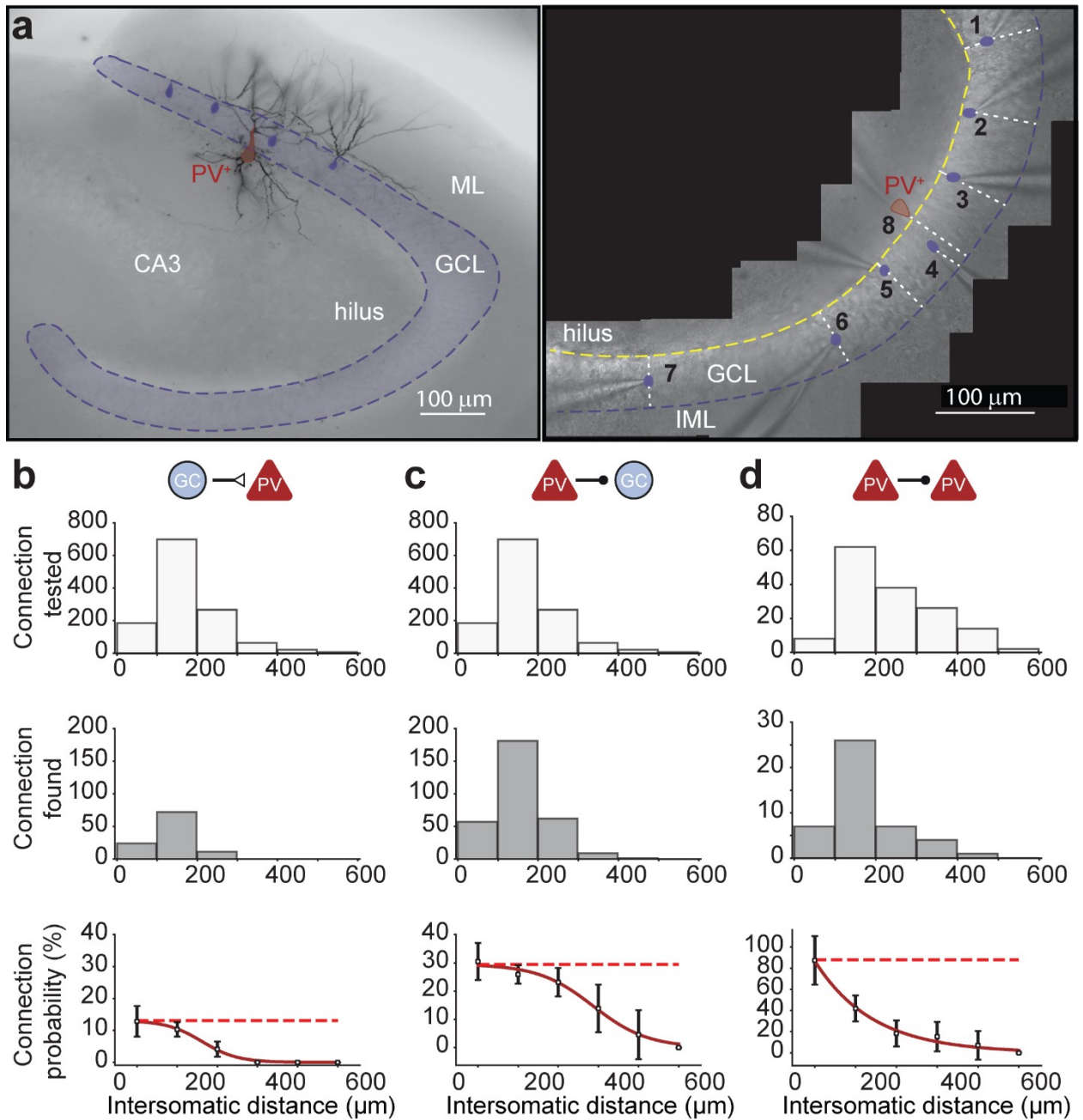
Figure 3.11: Distance-dependent measurements based on dentate gyrus shape.

(**a**) Light micrograph of a biocytin-labeled PV⁺ interneuron and four GCs (left). Note the curved shape of the granule cell layer (GCL). ML: molecular layer. Right collage of light micrographs in which eight pipettes are attached to seven GCs (1–7) and one PV⁺ interneuron (8), the somas are indicated by numbers. The intersomatic-distance between pairs was calculated using the mean of two values (d_1, d_2). d_1 corresponds to the sum of the perpendicular distance (white-dashed line) from the soma of neuron 1 to the outer-limit of the GCL (blue dashed-line), plus the perpendicular distance from the soma of neuron 2 to the outer-limit of the GCL, plus the outer-border of the

GCL that lies between the two measured neurons. d_2 was calculated as the sum of the perpendicular distance (white-dashed line) from the soma of the neuron 1 to the inner-limit of the GCL (yellow dashed-line), plus the perpendicular distance from the neuron 2 to the inner-border of the GCL, plus the inner-border of the GCL between the two measured cells. (**b**) From top to bottom: histograms for the number of connection tested versus intersomatic distance (corrected by the dentate gyrus "c" shape) and connection found versus corrected-intersomatic distance. Connection probabilities were calculated using the above information for GC–PV$^+$ interneuron pairs. (**c, d**) Same measurement than (b) but for PV$^+$ interneuron–GC pairs and PV$^+$– PV$^+$ interneuron pairs respectively. Note the shape of the curves for the connection probabilities of the three type of connections were similar to the curves obtained from intersomatic-distance estimated using the Euclidian tip-to-tip measurements (see **Fig. 3.5b, e, and 3.9b**).

3.1.5 Microscopic connectivity rules and connectivity motifs

Previous studies demonstrated that recurrent principal neuron–interneuron connectivity motifs are enriched above the chance level expected for a random network in several cortical microcircuits (Holmgren et al., 2003; Yoshimura et al., 2005; Larimer and Strowbridge, 2008; Couey et al., 2013; Peng et al., 2017). To test this hypothesis in the dentate gyrus, we analyzed the abundance of all 25 possible disynaptic connectivity motifs in our sample (**Fig 3.12**); (Schröter et al., 2017). To probe whether connectivity was random (Erdös and Rényi, 1959) or non-random (Song et al., 2005; Perin et al., 2011; Cossell et al., 2015; Jouhanneau et al., 2015; Guzman et al., 2016), we compared motif numbers in our experimental data to a simulated data set assuming random connectivity with experimentally determined distance-dependence connection probabilities (**Fig. 3.12a, b**).

Among the 25 possible disynaptic motifs, four types of motifs were significantly enriched above the chance level: 1) Gap junction connections between PV$^+$ interneurons, 2) mutual inhibition motifs (PV$^+$ interneuron–PV$^+$ interneuron connections) combined with gap junction connections (Rieubland et al., 2014), 3) convergence motifs (connections of multiple GCs on a single PV$^+$ interneuron), and 4) divergence motifs (connections of one PV$^+$ interneuron onto multiple GCs; **Fig. 3.12b**; $P < 0.05$ after Benjamini-Hochberg correction for multiple comparisons). Similar results were obtained for comparison with uniform and distance-dependent random models (Methods). Surprisingly, reciprocal GC–PV$^+$ interneuron motifs were not significantly enriched.

Previous studies further demonstrated that the amplitude of unitary IPSCs is higher in bidirectionally than in unidirectionally connected PN–IN pairs (Yoshimura et al., 2005). In contrast, in the dentate gyrus neither the amplitude of EPSCs nor that of IPSCs was significantly different between bidirectionally and unidirectionally connected GC–PV$^+$ interneuron pairs (**Fig. 3.12c**). However, the amplitude of IPSCs was significantly larger in PV$^+$ interneuron–PV$^+$ interneuron pairs coupled by reciprocal inhibitory synapses (**Fig. 3.12d**). Taken together, these results indicate that in the dentate gyrus, like in other cortical areas, synaptic connectivity of PV$^+$ interneurons is nonrandom. However, both the types of enriched motifs and the rules setting synaptic strength differ among circuits
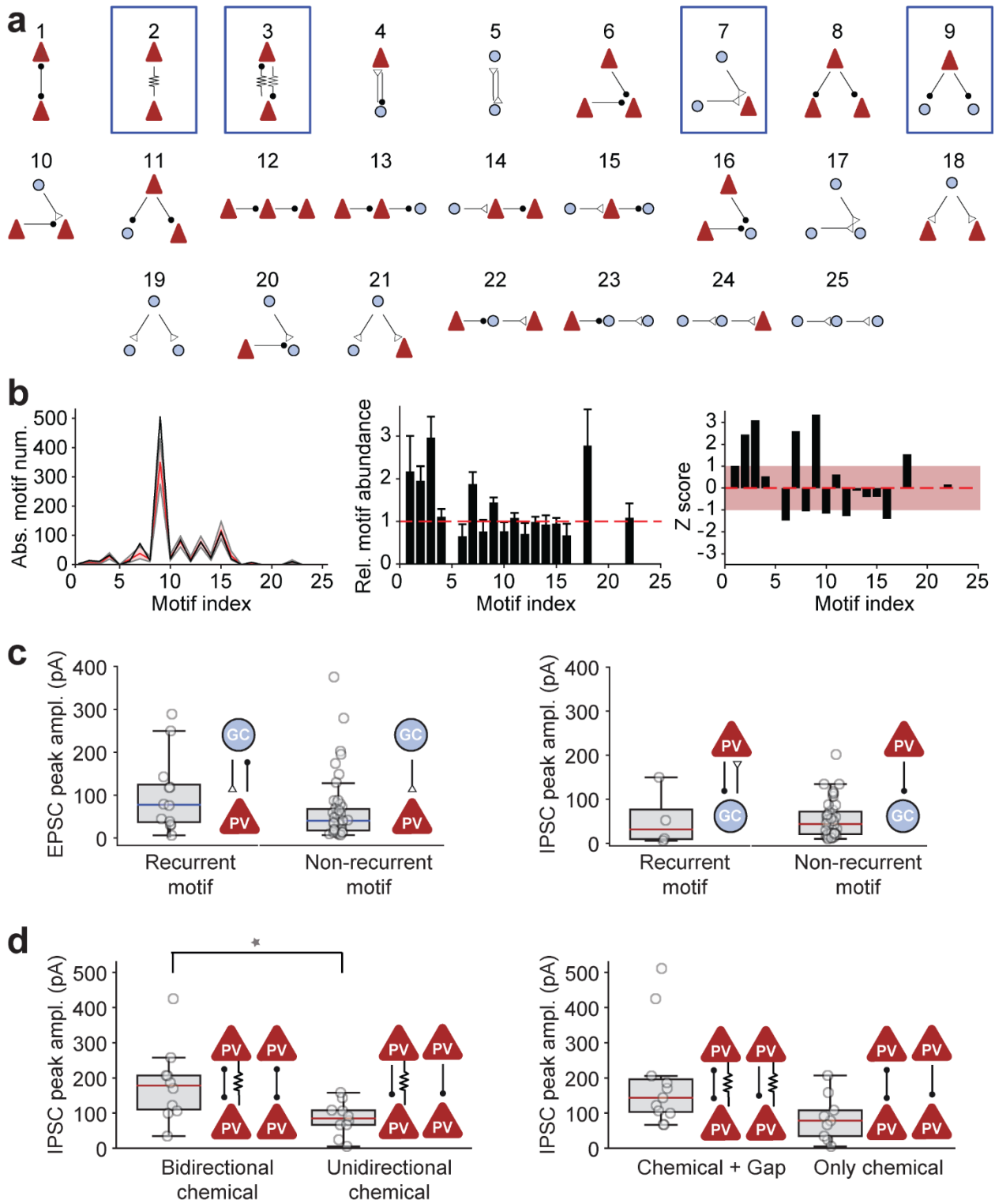
Figure 3.12: Overabundance of disynaptic connectivity motifs in GC–PV$^+$ interneuron networks and different functional properties of synaptic motifs.
(**a**) Graph analysis of disynaptic connectivity motifs. In total, there are five possible disynaptic connectivity motifs with two cells and 20 disynaptic motifs involving three cells. Arrows with open triangles indicate excitatory synapses, arrows with filled circles represent inhibitory synapses, and arrows with zigzag lines indicate gap junctions. Number indicates motif index. (**b**) Analysis of the number of motifs in 10,000 simulated data sets. Connection probability for the simulated data set was specified according to the experimentally determined spatial rules. Left, absolute motif number in experimental (black) and simulated data set (red, median; gray, 90%-confidence interval). Center, bar plot of relative abundance of various motifs (number of motifs in experimental data set over the mean number in simulated data set). Error bars were taken from bootstrap analysis. Right, bar plot of z score of the different motifs. Light red area indicates z score in the interval [−1, 1]. Motifs 2, 3, 7, and 9 were significantly enriched above the chance level (P = 0.03145, 0.0085, 0.0272, and 0.0068 after multiple comparison correction). In contrast, motifs 6, 8, 10, 12, and 16 were slightly, but not significantly underrepresented (P = 0.15 for motif 6). Note that motifs 5, 17, 19–21, and 23–25 were not encountered in the present data set, because of the lack of connectivity between GCs. (**c**) Comparison of EPSC peak amplitude (left) and IPSC peak amplitude (right) in bidirectionally versus unidirectionally coupled GC–PV$^+$ interneuron pairs. Peak amplitudes were not significantly different (P = 0.33 and 0.58, respectively). (**d**) Comparison of IPSC peak amplitude in PV$^+$ interneuron–PV$^+$ interneuron pairs connected by different chemical or electrical synapse motifs. IPSC peak amplitude was significantly larger in pairs with bidirectional inhibitory connections than with unidirectional connections (P = 0.016) and slightly higher in connections with than without gap junctions (P = 0.057). Asterisk indicates $P < 0.05$.

3.2 Computational results

3.2.1 Full-size network models to perform pattern separation

Our results demonstrate that the dentate gyrus has circuit-specific connectivity rules. Whether or not these rules support pattern separation is unclear. To address this question, we developed a realistic PN–IN network model of the dentate gyrus (**Fig. 3.13a, 2.2**). We simulated the network in full-size, with 500,000 GCs (Amrein et al., 2004); represented as integrate-and-fire (IF) neurons and 2,500 PV$^+$ interneurons (implemented as single-compartment conductance-based models). Connectivity rules of excitatory and inhibitory synapses in GC–PV$^+$ interneuron pairs, mutual inhibition, and gap junctions were implemented in accordance with experimental observations (**Fig 3.5, 3.9**). At the network input, 50,000 ECs were attached. The EC–GC connectivity was constrained by the width of the entorhinal cortex neuron axons (20% of the dentate gyrus along the longitudinal axis (Tamamaki and Nojyo, 1993) and the number of spines on the dendrites of GCs (~5,000; (Desmond and Levy, 1985; Schmidt-Hieber et al., 2007)). As gamma oscillations may contribute to WTA mechanism (de Almeida et al., 2009), an inhibitory conductance was initiated at the beginning of each simulation epoch (de Almeida et al., 2009). Since gamma oscillations show high power in the dentate gyrus (Pernía-Andrade and Jonas, 2014; Strüber et al., 2017), this also contributes to the realism of the model.

Simulation of pattern separation was performed in four steps (**Fig. 2.2**). First, hundred correlated binary activity patterns were applied in ECs. Second, corresponding patterns of driving current in GCs were computed from the upstream neuron activity vector and the connectivity matrix between ECs and GCs, representing the expansion of coding space from the entorhinal cortex to the dentate gyrus (Cayco-Gajic et al., 2017). Third, spiking activity (output patterns) was simulated for all patterns of driving current (input patterns). Then, pairwise correlation coefficients were computed for input and output patterns and plotted against each other. We quantified the network performance with three measures (methods). First, we measured the efficacy of patterns separation using a pattern separation index (ψ), defined as the normalized area between the data point and the identity line (**Fig. 2.2**). For the standard parameter set (**Table 1**), the plot of output versus input correlation was highly nonlinear, with a ψ of 0.560 (**Fig 3.13c**), as expected for an efficient pattern separator

(Leal and Yassa, 2018). Second, we computed the reliability of pattern separation ρ from the correlation of the ranked R values; for standard parameters, this value was 0.98 (**Fig. 3.13d**). Finally, we measured the maximal gain of pattern separation γ from the slope of the input-output correlation for $R_{in} \rightarrow 1$. In the standard model, γ was 11.1, implying that small differences in input patterns are converted into large differences in output patterns (**Fig. 3.13e**).

a

c_{EI} σ_{EI}

c_{IE} σ_{IE}

c_{IE} c_{EI}

b

500,000 GCs **A** **B**

500,000 GCs and 2,500 PV+ INs **A'** **B'**

c

Granule cell number
Time (ms)

Interneuron number
Time (ms)

d

Efficacy ψ = 0.560

Output correlation
Input correlation

Input (R_{in}) Output (R_{out})

a Pattern completion

b Pattern identity

c Pattern separation

e

Reliability ρ = 0.98

Output rank
Input rank

f

Gain γ = 11.1
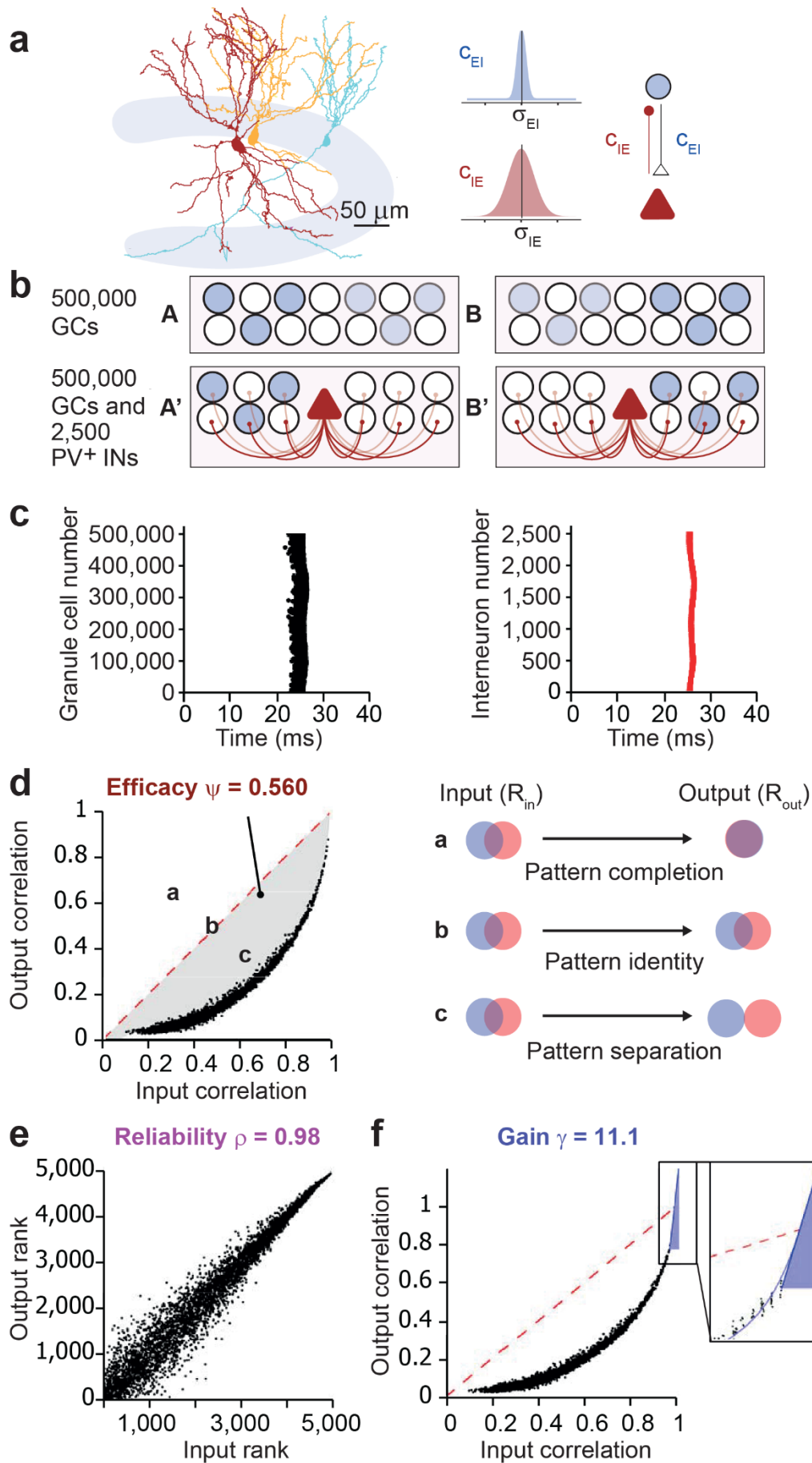
Output correlation
Input correlation

Figure 3.13: A biological realistic principal neuron–interneuron network generates efficient pattern separation.
(**a**) Schematic illustration of the structure of a biologically realistic model of the dentate gyrus. Left, partial reconstruction of one GCs and two PV$^+$ interneurons. Right, schematic of the connection probability distribution for excitation (light blue, c_{EI}) and inhibition (red, c_{IE}), these values were obtained for experimental data (**Fig. 3.5**) and incorporated in the model. (**b**) Schematic illustration of WTA mediated by lateral inhibition for pattern separation. Only GCs (circles) and INs (triangles) are depicted. Blue indicates cell activity, with intensity reflecting the level of excitatory synaptic drive. Left, activity pattern A, right, activity pattern B. Top, network in the absence of inhibition, bottom, network in the presence of inhibition. (**c**) Raster plots of AP generation in PNs (right, black) and INs (left, red). Each point represents an AP. (**d–f**) Output–input function in a network with standard parameter settings. Data points represent pairwise correlation coefficients between input patterns (excitatory drive, R_{in}) and corresponding output patterns (AP activity, R_{out}). (d) Left, dashed red line indicates identity. With standard parameter settings, ψ (determined from the area between data points and identity line) was 0.560, demonstrating efficient pattern separation. Left, illustration shows three different regimes in the graph (a, pattern completion; b, pattern identity; c, pattern separation). (e) Furthermore, the reliability of pattern separation ρ was computed as the correlation of ranked R_{out} versus ranked R_{in} data. (f) Finally, the gain γ of pattern separation, determined from the maximal slope of a polynomial function fit to the data for x → 1, was 11.2, demonstrating that the network amplifies small differences in the input patterns into large differences in the output patterns. Blue curve indicates fit function, and the blue line represents the corresponding tangent. For details, see Methods.

Similar results were obtained when the tonic EC–GC drive was replaced by fast excitatory synaptic waveforms (**Fig. 3.14a**). Likewise, efficient pattern separation was also observed in a network model that incorporated feedforward activation of interneurons; the value of ψ was even slightly higher than in the standard network (**Fig 3.14**). Taken together, a biologically realistic PN–IN network is able to efficiently and reliably perform pattern separation computations.
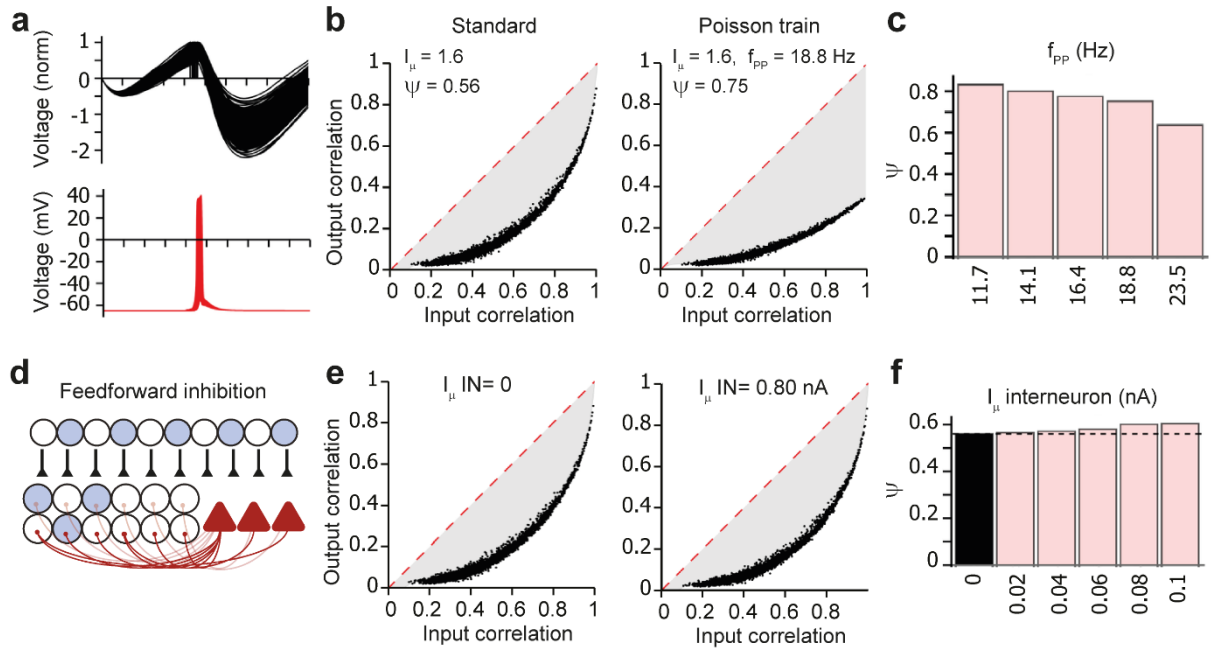
Figure 3.14: A network model with realistic EC–GC synaptic properties and feedforward inhibition can perform efficient pattern separation.
(**a**) Simulated membrane potentials of a principal neuron (top) and an interneuron (bottom) in a model with realistic EC–GC synaptic input represented by Poisson trains of APs at different frequencies. (**b**) Input-output correlation curves for standard model with tonic excitatory drive (left; $I_\mu = 1.6$) and a model in which excitatory drive was generated by Poisson trains of EPSPs in GCs (right; $f_{PP} = 18.8$ Hz, activation frequency was chosen to give $I_\mu \approx 1.6$). Note that the randomness of the input trains resulted in a drop of the output correlation for input correlation values approaching 1, because an additional random process is added to the system. (**c**) Dependence of ψ on activity frequency of the perforant path synapses. The synaptic weight of EC–GC synapses was set to $J_{EC–GC} = 0.002$ in all simulations. Activation frequency was chosen to approximately match $I_\mu = 1, 1.2, 1.4, 1.6$, and 2.0 in the standard model. (**d**) Schematic illustration of the network model incorporating feedforward inhibition. ECs innervate GCs and INs with similar connectivity rules. The tonic excitatory drive in an individual IN is computed from the drive from the nearest GC as: $I_{\mu I}[i] = I_{\mu E}[i / n_I \times n_E] / < I_{\mu E} > \times I_{\mu, I}$, $i = 1 … n_I$, where $I_{\mu I}[i]$ is the excitatory drive in the ith interneuron (unitless), $I_{\mu E}[i]$ is the excitatory drive in the ith GC, n_I is the number of INs, n_E is the number of GCs, $< I_{\mu E} >$ is the average excitatory drive overall GCs, and $I_{\mu, I}$ is the chosen excitatory drive in the INs (in pA). (**e**) Input-output correlation function in a control network (left) and in a network incorporating feedforward drive to INs (right). (**f**) Dependence of ψ on feedforward drive on INs. Black bar, default value (no feedforward drive); light red bars, larger values (increased feedforward drive). Note that ψ is slightly increased by the incorporation of feedforward excitation of INs.

3.2.2 Lateral inhibition is a primary mechanism underlying pattern separation

To identify the key mechanisms underlying pattern separation in the network model, we systematically varied the biologically relevant parameters (**Fig. 3.15**). First, we changed the amplitude of the excitatory synaptic drive (I_μ) and the inhibitory gamma input (J_{gamma}) in the network, parameters expected to affect thresholding properties of input-output conversion (**Fig. 3.15a**). Pattern separation was highly dependent on both parameters. Contour plot analysis revealed that the combination of small excitatory synaptic drive with small gamma input provided efficient pattern separation (**Fig. 3.15b**). As the excitatory drive was increased, a higher inhibitory gamma input was required to maintain the efficacy of pattern separation. Thus, the balance between excitatory drive and inhibitory gamma input determined the efficacy of pattern separation. Then, we tested the contribution of lateral inhibition to pattern separation in the network model (**Fig. 3.15c**). Reducing the strength of either excitatory EI or inhibitory IE connections (J_{EI}, J_{IE}) reduced pattern separation efficacy ψ substantially (**Fig. 3.15c**). Furthermore, complete elimination of both excitatory EI and inhibitory IE synapses severely impaired pattern separation. Contour plot analysis of ψ against I_μ and J_{gamma} in the absence of lateral inhibition revealed ψ values > 0.5 were only obtained in a small part of the parameter space (**Fig. 3.15d**).
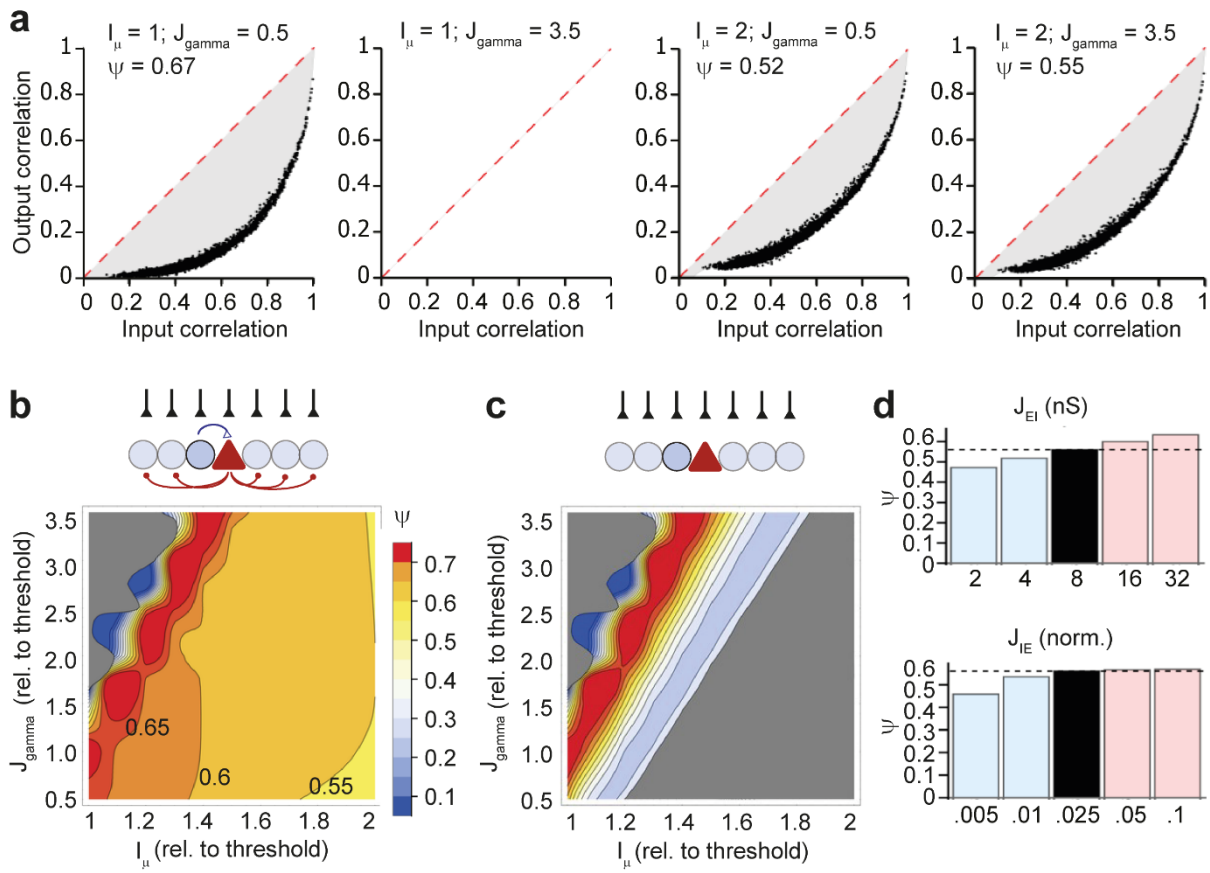
Figure 3.15: A winner-takes-all mechanism by lateral inhibition plays a critical role in pattern separation.
(**a**) Output–input functions for changes in network parameters in comparison to default values. Left to right, I_μ was set to 1, while external inhibitory gamma drive J_{gamma} was set to 0.5 or 3.5; then I_μ was set to 2.0 while changing J_{gamma} as before. Note that efficient pattern separation was observed in all scenarios except the condition with low excitatory drive and high J_{gamma} (where α activity was 0). (**b**) Contour plot of ψ against the mean excitatory drive (I_μ, abscissa) and amplitude of external inhibitory gamma drive (J_{gamma}). Contour lines indicate ψ; warm colors represent high values, and cold colors denote low values. In the gray part of the plot, the correlation between input and output patterns was $\rho < 0.1$ or activity α was > 0.8. Note efficient pattern separation in a large subregion of the I_μ–J_{gamma} parameter space. (**c,d**) Lateral inhibition is necessary for efficient pattern separation. (c) Contour plot of ψ against the mean excitatory drive (I_μ, abscissa) and amplitude of external inhibitory gamma drive (J_{gamma}) after complete elimination of lateral inhibition ($c_{EI} = 0$, $c_{IE} = 0$). Note efficient pattern separation in only a minimal subregion of the I_μ–J_{gamma} parameter space. (d) Effects of changes in synaptic strength of excitatory EI synapses (J_{EI}) and inhibitory IE synapses (J_{IE}). Black bars indicate ψ for standard parameter settings; light blue bars represent reduced values; light red bars indicate increased values in comparison to standard values. Note that the reduction in both J_{EI} and J_{IE} reduces the ψ value.

71

Next, we determined how the properties of the synaptic input from ECs contribute to pattern separation through the code expansion mechanism (Marr, 1969; Albus, 1971; Cayco-Gajic et al., 2017). To address this, we varied the number of entorhinal cells (n_{EC}), the average EC activity level (α_{EC}), and peak value and width of EC–GC connectivity ($c_{EC–GC}$ and $\sigma_{EC–GC}$; **Fig. 3.16b**). Increasing the number of ECs decreased ψ, whereas decreasing the number increased it. Likewise, increasing the average EC activity decreased ψ, whereas reducing the activity had the reverse effect. Furthermore, increasing the EC–GC connection probability and the width decreased ψ, whereas decreasing probability or width led to opposite changes (**Fig. 3.16b**). Effects of connection probability and width were similar when the GC drive values were shuffled, indicating that spatial correlations in the input played only a minor role in pattern separation (**Fig. 3.16c, d**). Taken together these results suggest that the properties of the excitatory synaptic input influence pattern separation, but quantitatively play a relatively minor role. Thus, these results emphasize the importance of lateral inhibition for the pattern separation computation.
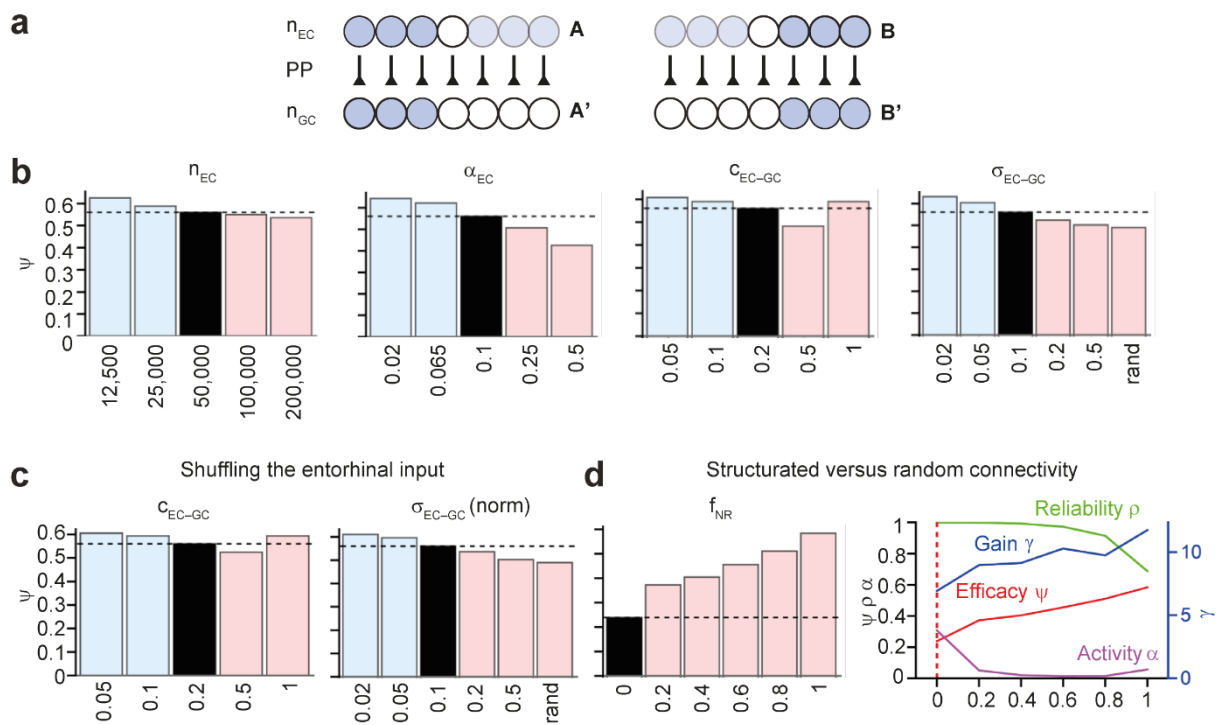
Figure 3.16: Effects of structured EC–GC connectivity on pattern separation.
Schematic illustration of the entorhinal cortex input to GCs. (**b**) Divergent connectivity between ECs and GCs is important for efficient pattern separation. From left to right, effects of changes in the number of ECs (n_{EC}), average activity (α_{EC}), maximal connection probability of EC–GC connectivity (c_{EC-GC}) and width of EC–GC connectivity (σ_{EC-GC}). Note that high expansion ratio (n_{GC} / n_{EC}), sparse activity (α_{EC}), and sparse EC–GC connectivity facilitate efficient pattern separation. (**c**) ψ for different values of peak connectivity probability (c_{EC-GC}, left) and width of entorhinal connectivity (σ_{EC-GC}, right) for a network in which the excitatory drive in GCs was shuffled. Note that the results are only minimally different from those in the standard network (b). (**d**) Effects of structural connectivity rules of EC–GC connections. EC–GC connectivity was either completely random, completely structured so that EC–GC synapses were formed within a full connectivity disc, or showed mixed properties. Left, bar graph of pattern separation efficiency ψ for different proportions of nonrandom connections. Black bar, fraction of nonrandom connections $f_{NR} = 0$; i.e. all connections random; light red bars, enhanced structured connectivity ($f_{NR} = 0.2$ to 1, 1 = all connections structured). Right, a plot of pattern separation efficiency ψ (red), reliability ρ (green), gain γ, and average activity α as a function of the fraction of nonrandom connections. PP (perforant path).

3.2.3 Focal connectivity and fast interneuron signaling ensure efficient pattern separation

The high pattern separation efficacy was surprising because the network model contains experimentally determined focal connectivity rules for both excitatory EI and inhibitory IE synapses (**Fig. 3.5**). In contrast, an efficient WTA mechanism may require lateral inhibition with long-range connectivity to ensure that a winner suppresses all non-winners in the network. To resolve this apparent contradiction, we explored the effects of focal EI and IE connectivity in the network model (**Fig. 3.17**). To address the effects of focal connectivity in isolation, we maintained the total connectivity (i.e., the area under the connection probability–distance curve) through compensatory changes of maximal connection probability and, if required, synaptic strength (**Fig. 3.17a**). Increasing the width of connectivity for both excitatory EI and inhibitory IE synaptic connections reduced ψ; particularly large changes were observed when focal connectivity was fully replaced by global connectivity. Thus, unexpectedly, focal PN–IN connectivity supported pattern separation more effectively than global connectivity.

Next, we examined the effects of combined changes in the width of excitatory EI and inhibitory IE connectivity (**Fig. 3.17b**). As in the previous set of simulations, we maintained the total connectivity. Contour plot analysis confirmed that focal connectivity supported pattern separation more effectively than broad connectivity.

However, the effects of changes in the width of excitatory EI and inhibitory IE connectivity were asymmetric. Thus, a high ψ was obtained in an asymmetric configuration in which the excitatory EI was more focal than the inhibitory IE connectivity (**Fig. 3.17b**). This effect was consistent with experimental observations that excitatory EI is more focal than inhibitory IE connectivity (**Fig. 3.5**). Thus, asymmetric connectivity effectively supported pattern separation.

Why does focal connectivity support pattern separation better than global connectivity? One possibility is that the effects of focal connectivity might be a consequence of changes in average latency, which are shorter in a focally connected network than in an equivalent random network. To test this hypothesis, we examined the effects of changes in axonal action AP velocity at excitatory EI and inhibitory IE synapses on pattern separation. Slower conduction velocity reduced ψ, whereas faster conduction velocity increased it, for both excitatory EI and inhibitory IE synapses (**Fig. 3.17c**, top). To test whether changes in synaptic latency fully account for the functional differences between focal and random networks, we changed the space constant while maintaining the kinetic properties of disynaptic inhibition through compensatory changes of the delay (**Fig. 3.17c**, middle, and bottom). Notably, differences in latency almost entirely compensated the effects of changes in connectivity. Thus, focal connectivity and fast biophysical signaling in GC–PV$^+$ interneuron microcircuits play synergistic roles in pattern separation (**Fig. 3.17d**).
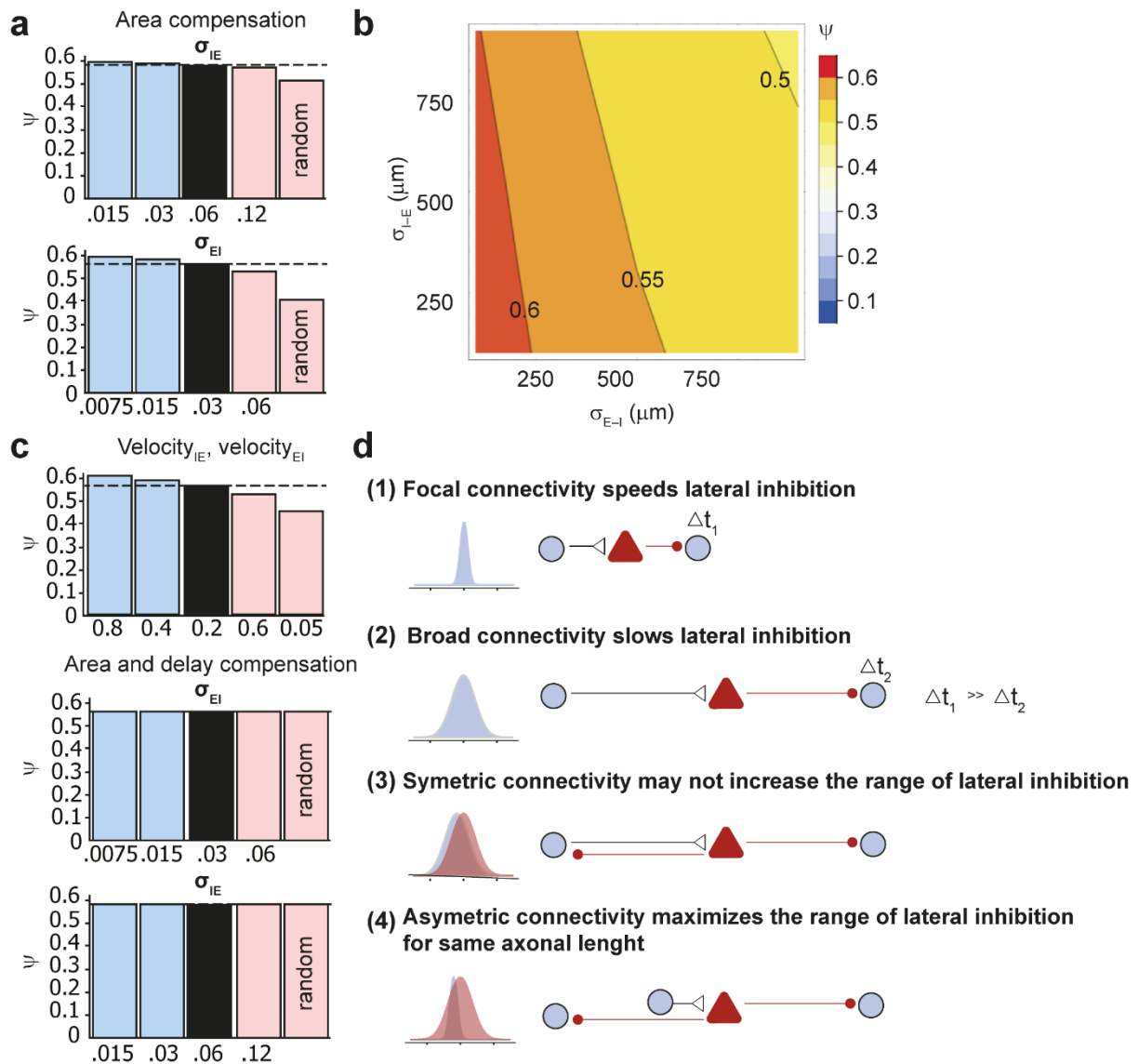
Figure 3.17: Focal connectivity and fast lateral inhibition enhance pattern separation performance.

(**a**) Effects of focal connectivity on pattern separation. Summary bar graph of ψ for different values of excitatory σ_{EI} (left) or inhibitory σ_{IE} (right) in the network. Right bar in each bar graph represents uniform random connectivity. Peak connectivity was adjusted to maintain the total number of synaptic connections (i.e., the integral under the connection probability–distance curve). (**b**) Contour plot of ψ against width of excitatory EI connectivity (σ_{EI}) and inhibitory connectivity (σ_{IE}). Note that networks with focal connectivity show more efficient pattern separation than networks with broad connectivity. Also, note that asymmetry in spatial connectivity rules supports pattern separation. This effect is consistent with the experimental observation of focal excitatory EI connectivity versus the broader inhibitory IE connectivity (Fig. 3.5). (**c**) Top, effects of fast interneuron signaling on pattern separation. Summary bar graph of ψ for different AP propagation velocity values for both excitatory EI (left) or inhibitory IE connectivity (right) in the network. Bottom, effects of focal connectivity and signaling speed are closely interrelated. Comparison of effects of changes in the width of EI and IE synapses after compensatory adjustment of both connectivity and delay to maintain the value under control conditions. Note that broadening of connectivity fails to reduce pattern separation performance in the presence of delay

adjustment. Thus, the beneficial effects of focal innervation are largely generated by faster signaling. (**d**) Schematic illustration of how spatial connectivity rules shape pattern separation. (1) Focal connectivity speeds lateral inhibition and enhances the efficacy of the WTA mechanism. (2) Broad connectivity slows lateral inhibition and reduces the efficacy of the WTA mechanism. (3) Symmetric connectivity with similar spatial rules of excitatory PN–IN synapses and inhibitory IN–PN synapses may fail to increase the range of lateral inhibition, because excitatory PN–IN synapses and inhibitory IN–PN synapses may statistically run in opposite directions. (4) Asymmetric connectivity with different spatial rules for excitatory PN–IN synapses and inhibitory IN–PN synapses efficiently increases the range of lateral inhibition for the same axon length.

3.3 Silencing the activity of PV$^+$ interneurons *in vivo* impairs pattern separation

Our previous results show that inhibition is highly relevant for decorrelating neuronal activity patterns in the dentate gyrus. Moreover, we showed that PV$^+$ interneurons are highly connected to GCs through lateral inhibition (**Fig. 3.4**) and our network simulations show that fast signaling is highly relevant for pattern separation through WTA mechanism (**Fig. 3.17**). These findings strongly support the involvement of PV$^+$ interneurons in pattern separation. To test the behavioral relevance of these findings, we selectively silenced the activity PV$^+$ interneurons by pharmacogenetics. Bilateral injections of AAV encoding an inhibitory DREADD (hM4Di) into the dentate gyrus of PV-Cre adult male mice postnatal day 60–90 were performed in the experimental group. In contrast, the control group received AAV injections encoding only a fluorophore (mCherry) (**Fig. 3.18a**). After two weeks of the intracranial injections, mice performed in a fear contextual discrimination task, in which the level of freezing was measured as an indicator for discriminating between an environment A (where a foot-shock was delivered) and a similar environment B (**Fig. 3.18b**). All mice (from the experimental and control group) received a daily dose of CNO, 30 minutes before the behavioral trails started.

When PV$^+$ interneurons were silenced, mice exhibit normal acquisition and retrieval of fear memories (**Fig. 3.18c, d**), but failed to discriminate between similar environments, when they were acutely exposed to both contexts (during the same test day) (**Fig. 3.18e**). However, after repeated exposure to the environments the difference between experimental and control group was lost (**Fig. 3.18f**). These results are preliminary, and further experiments needed to study the effects of fear

generalization on pattern separation and the long-term relevance of PV$^+$ interneurons (or other interneuron types) on contextual pattern discrimination.
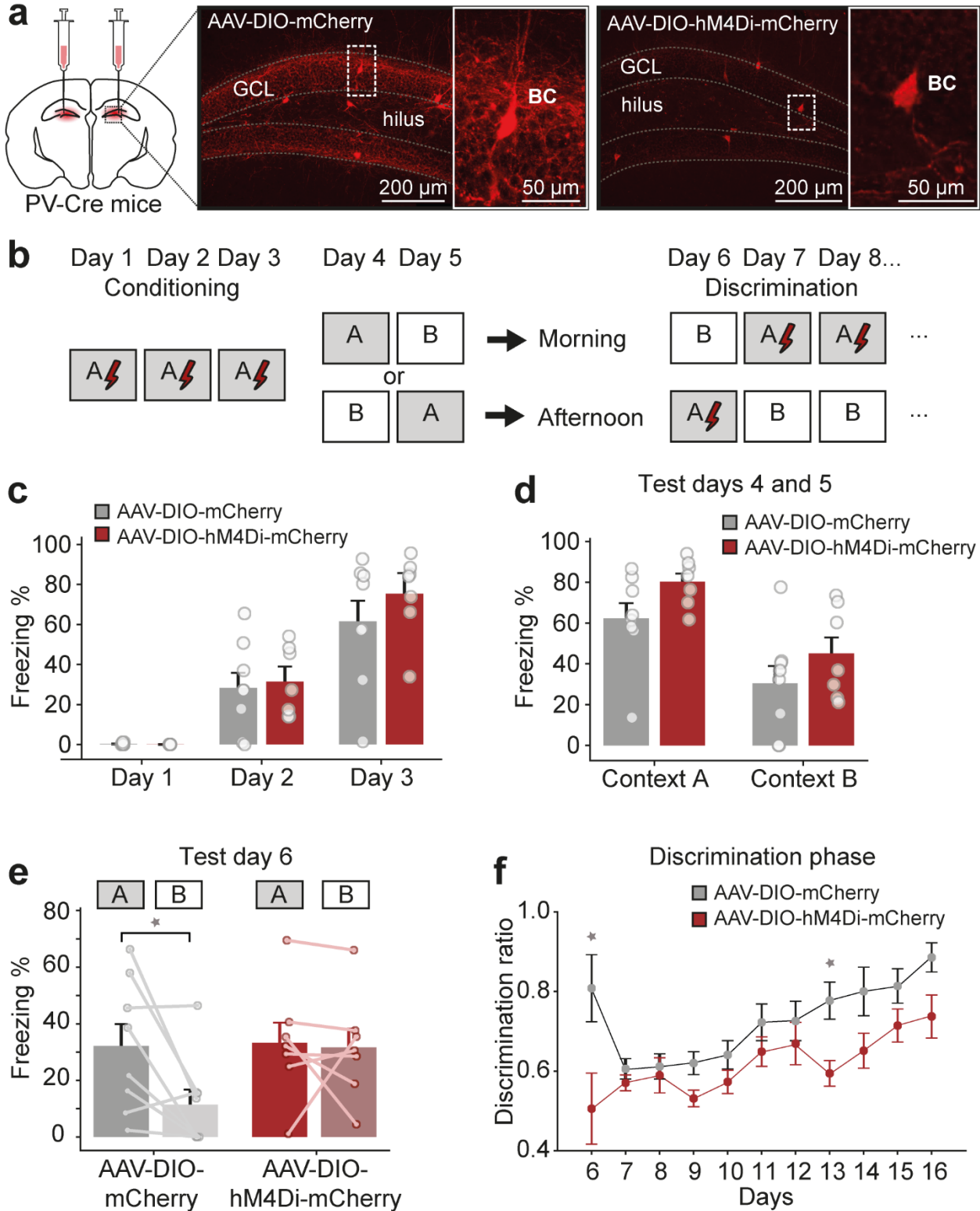
Figure 3.18: Silencing the activity of PV⁺ interneurons *in vivo* acutely impairs discrimination between similar contexts.
(**a**) Illustration of bilateral virus injection into the dentate gyrus and confocal images of coronal sections of the dentate gyrus. Middle, labeling of basket cells (BC) in PV-Cre mice injected with AAV_{dj}-DIO-mCherry (control group). Right, mice injected with AAV_{dj}-DIO-hM4Di-mCherry (experimental group). (**b**) Illustration of the behavioral protocol. (**c**) Contextual fear conditioning during three consecutive days showed no difference in the acquisition of fear memories between experimental and control. (**d**) Due to the similitude of the contexts, moderate fear generalization occurred in the experimental and control group, since animals showed the same freezing levels in both contexts (A and B). (**e**) Day 6 corresponds to the first exposition to both environment A and B during the same day. Control group showed statistically significant less freezing in context B in comparison to A, indicating discrimination between contexts. However, in mice with silenced PV⁺ interneuron activity, no difference in the freezing level was observed between the contexts, indicating impairment in contextual fear discrimination test. (**f**) Discrimination ratio ($Freezing_{context\ A}$ / ($Freezing_{context\ A}$ + $Freezing_{context\ B}$) during ten consecutive days. There was no statistically significant difference between groups (except for the days 6 and 13). However, mice with silenced PV⁺ interneuron activity tended to show lower discrimination ratios than the control group.

Chapter 4
DISCUSSION

The identification of the structural bases of complex behaviors has inspired scientific curiosity from the beginning of the neuroscience field (Ramón y Cajal, 1911). Pattern separation is a form of information processing underlying neuronal representations that in the context of episodic memory, the dentate gyrus has a prominent role. Moreover, the dentate gyrus circuit underneath a unique property of the hippocampus: memory traces are created and maintained as temporary repositories that can be recalled from a network with limited storage capacity (Marr, 1971). These constraints could be overcome by decorrelating firing patterns, which not only improve the discrimination of similar behavioral relevant experiences but also increase the number of events that can be stored. Based on our experimental and computational approaches, we provide evidence that the local circuits of the dentate gyrus are optimized for accomplishing efficient pattern separation, with behavioral relevant consequences. Specifically, we showed that local GCs–PV$^+$ interneuron circuit is organized to maximize the separation of input patterns using WTA as the primary mechanism. At the connectivity level, we found PV$^+$ interneurons mediating strong lateral inhibition, having an asymmetric distribution of the excitatory and inhibitory connectivity, and organized in specific disynaptic motifs of PNs and INs. At the theoretical level, we showed that fast inhibitory signaling mediated by PV$^+$ interneurons, together with structured PN–INs connectivity rules work in synergy with the input properties of the dentate gyrus for efficient pattern separation. Finally, these findings were supported by behavioral data showing the involvement of PV$^+$ interneurons in the emergence of pattern separation in a behavioral task.

4.1 Synapse-specific connectivity of PV[+] interneuron networks

Despite PV[+] interneurons constituting only 15% of the GABAergic interneurons in the hippocampus (Hosp et al., 2014), they predominantly connect to GCs in comparison to other interneuron types (**Fig. 3.4**). Besides, the synaptic strength of excitatory and inhibitory synapses involving PV[+] interneurons is higher than those containing CCK[+] and SST[+] interneurons (**Fig. 3.3c; 3.5a, d**), as previously described (Bartos and Elgueta, 2012; Pfeffer et al., 2013). However, we cannot exclude the possibility that for distal SST[+]–GC synapses connectivity may be underestimated, because of substantial attenuation of synaptic signals by cable filtering. Nonetheless, our results demonstrate that the rules of functional connectivity of GC–PV[+] interneuron networks in the dentate gyrus fundamentally differ from those in other cortical circuits (**Table 2**). Thus, the main structural properties of the dentate gyrus can be summarized in distance dependence GC–PV[+] interneurons connectivity (**Fig. 3.5b, e**) associated to an asymmetrical distribution of connections (**Fig. 3.17d**) with a predominance of lateral inhibition (**Fig. 3.5h**).

The distance dependence of connectivity seems to be a topological organization, circuit-specific and strongly related to the structure of the input (Levy and Reyes, 2012). Previous patch-clamp recordings have shown in layer 2/3 of the somatosensory and visual cortex that PN–PN connectivity decreases from 10% (< 25 µm) to less than 1% for distances further than 200 µm apart (Holmgren et al., 2003). Similarly, in layer V of the somatosensory cortex, the drop-off the connectivity goes from 20% to 5% for the same distances (Perin et al., 2011). In general, these probabilistic distributions have a bell-shaped profile that drops to near zero with broad intersomatic distances. Interestingly, this probabilistic connectivity distribution is absent among PNs in the CA3 network (Guzman et al., 2016). Regarding the mapping of the interneuron connectivity across brains regions, several techniques have been used such as patch-clamp, calcium imaging and optogenetics, which could explain the difference in the reported results. High connectivity has been shown in PNs–PV[+] interneurons networks in the V1 (Holmgren et al., 2003; Ko et al., 2011), decreasing slowly with the distance (Holmgren et al., 2003), similarly to our results. Interestingly, one study using two-photon glutamate uncaging reported differences in the connection probabilities of PNs–PV[+] interneurons pairs for intersomatic-distances inferior to 200 µm while comparing different neocortical regions (Packer and Yuste, 2011). However,

the same study highlights the presence of random connectivity between PV[+] interneurons–PNs.

In addition, our results show that the local excitatory connectivity associated with broad inhibitory connectivity leads to an asymmetrical distribution of connections (**Fig. 3.5b, e, 3.17d**). In our biological inspired model, this topology seems to be highly relevant for pattern separation computation, as it is further discussed in the next section **(Fig. 3.17)**. Finally, the unidirectional inhibitory connections are ~10-times more frequent than reciprocal connections, demonstrating a strong prevalence of feedback thought lateral inhibition, which seems to be specific to the dentate gyrus (**Table 2**). In contrast, in presubiculum, visual, somatosensory, and entorhinal cortex reciprocal connections are equally or more abundant than unidirectional connections, implying feedback inhibition mediated by recurrent inhibition (**Table 1**). This finding makes us questioning about the functional meaning of two forms of feedback inhibition involving the same interneuron type. The predominance of feedback inhibition with reciprocal PNs–PV[+] interneurons connections may respond to a specific form of information processing. In sensory circuits, the abundance of reciprocal connections is observed between neuronal pairs sharing similar receptive fields or common intra\inter-laminar inputs (Yoshimura et al., 2005; Ko et al., 2011; Cossell et al., 2015). Also, in the neocortex, the high activity of PN requires a mechanism to establish excitation–inhibition balance; reciprocal PN–IN connectivity seems well suited for this purpose (Wiechert et al., 2010). In contrast, in the dentate gyrus, the PN activity is low, and such a balancing function may not be required (Pernía-Andrade and Jonas, 2014; Pilz et al., 2016; Danielson et al., 2017; GoodSmith et al., 2017; Senzai and Buzsáki, 2017). Regarding the synchronization of neuronal activity, feedback networks mediated by reciprocal PN–IN connectivity could contribute to the generation of slower network oscillations in these brain regions (such as lower gamma or beta frequency range), which are characteristic for the neocortex.

4.2 More about non-random organization, connectivity motifs

Connectivity motifs correspond to topological patterns of neuronal organization that may be related to specific forms of information processing. Modeling work has suggested a functional role in modulating the dynamical properties of a network, synchronization, and transition between periodic to chaotic behaviors of a neuronal system (Zhigulin, 2004; Prill et al., 2005; D'Huys et al., 2016). Thus, neuronal motifs, together with the description of probabilistic connectivity distribution may reflect not only the architectural nature but also the intrinsic functional properties of a network.

In the dentate gyrus, while analyzing all possible disynaptic connectivity motifs, we observed that convergence, divergence and mutual inhibition motifs are statistically overrepresented **(Fig. 3.11a, b)**. This above-chance representation of disynaptic motifs has also been found in cerebellar networks, where feedforward triplets and overlap of chemical and electrical synapses is also described (Rieubland et al., 2014). Divergent and convergent motifs have received more attention in the microcircuits of the inner retina, in which asymmetric wiring motif of the bipolar cells contribute to the feature-oriented representation of the visual world (Euler et al., 2014). In the central nervous system, the high abundance of convergence and divergence motifs are consistent with scale-free structural properties, which may enhance the robustness of network computations, as previous modeling work suggested (Barabási and Albert, 1999; Albert et al., 2000). Additionally, this fine-circuit design seems to be early specified during the development, as it is evidenced by hub GABAergic neurons sharing same cellular progenitors (Bonifazi et al., 2009).

Regarding the functional role of the mutual inhibition motifs, the connectivity rules of networks involving PV$^+$ interneurons may be related to the generation of network oscillations in the dentate gyrus (Bartos et al., 2007). The dense and focal electrical–chemical connectivity may explain the high power and frequency of gamma oscillations in the dentate gyrus (Bartos et al., 2007; Strüber et al., 2017). Previous modeling work suggested that the small-world interneuron network architecture will support the emergence of coherent gamma oscillations (Watts and Strogatz, 1998; Buzsáki et al., 2004). Our results support this notion since the high abundance of electrical–chemical mutual inhibition motifs would be consistent with small-world architectural properties (Song and Wang, 2014). The establishment of a robust gamma oscillation circuit may, conversely, be necessary for the pattern separation

process. Proposed models of pattern separation imply that the separation of patterns takes place in the period during the recovery from a preceding gamma cycle (de Almeida et al., 2009). In concordance to that, in our biological inspired-model was tested the coexistence of the pattern separation computation and the generation of gamma oscillations **(Fig. 2.2, 3.14)**.

A functional fine-network organization may explain why other previously described motifs where not overrepresented or even did not exist in the dentate gyrus (chain motifs or motifs involving only GCs) **(Fig. 3.11).** In CA3, for example, chain motifs are critical for the emergence of efficient pattern completion computation (Guzman et al., 2016). In the neocortex, recurrent motifs increase the signal of inputs, shape receptive fields (Lee et al., 2016) and response properties such as orientation selectivity (Cossell et al., 2015). Moreover, a theoretical work had hypothesized that different distributions of motifs across brain regions might account for different forms of information storage, being the overrepresentation of recurrent PN–PN motifs a type of network optimization for maximizing the storage of attractor states (Brunel, 2016). In the dentate gyrus, such a mechanism may not exist since in more of 5,000 PN–PN tested pairs any connection was found. Nevertheless, mossy cells contribution to this specific neuronal computation remains to be tested.

Together these findings indicate that the fine-scale topological organization of the network in precise connectivity motifs are circuit specific and may relate to very well define network functions. Thus, the GC–PV⁺ interneuron networks of the dentate gyrus are characterized for a feedback circuit of lateral inhibition with overrepresented embedded convergent, divergent and recurrent inhibitory motifs.

4.3 Winner-takes-all as a mechanism for pattern separation in the dentate gyrus

Our *in vitro* measurements suggest that the dentate gyrus network obeys unique connectivity rules, probably as an adaptation to specific network functions implemented in this brain region. A major function of the dentate gyrus is pattern separation (Leutgeb et al., 2007; Rolls, 2016), thought to be generated by a WTA mechanism (Majani et al., 1988; de Almeida et al., 2009; Tetzlaff et al., 2012; Faghihi and Moustafa, 2015). In an ideal pattern separation circuit, a small population of activated "winner cells" must be able to efficiently and rapidly inhibit a large population of "non-winner cells" (**Fig. 1.5**). Thus, this phenomenon is highly dependent on the synaptic properties (e.g., synaptic strength, synaptic location, latency) and the circuit architecture (recurrent versus lateral inhibition). Previous theoretical work has shown that lateral inhibition will suit this function in biological inspired networks (Coultrip et al., 1992; Shoemaker, 2015). In agreement with this finding, our experimental data showed that dentate gyrus connectivity rules seem to be well suited for these functions. First, lateral inhibition efficiently suppresses non-winners, whereas winners remain unaffected. Second, the combination of local connectivity and the rapid axonal signaling mechanisms of PV$^+$ interneurons (Hu et al., 2014) implements a high-speed suppression mechanism, as required for efficient pattern separation. Thus, we decided directly test the role of inhibition for pattern separation in a biologically realistic model of the dentate gyrus.

The implementation of a full-size network model allowed us to test whether the properties of synapses and microcircuits in the dentate gyrus support pattern separation while dissecting the mechanisms underlying this computation. In this regard, our main contributions were first to provide evidence that biologically realistic network model incorporating lateral inhibition is a highly efficient pattern separator. Second, we showed that focal connectivity and fast biophysical signaling properties of PV$^+$ interneurons are necessary for efficient pattern separation. Finally, our results suggest that specific features of the input region of the dentate gyrus (entorhinal input) acting in synergy with winner-takes-all mechanism mediated by lateral inhibition are the most important mechanisms underlying pattern separation within the dentate gyrus.

Classical work in the cerebellum suggested code expansion as the key mechanism underlying pattern separation (Marr, 1969; Albus, 1971; Cayco-Gajic et

al., 2017). Our computational analysis confirms that the connectivity rules between ECs and GCs play an important role in pattern separation in the dentate gyrus. First, the number of ECs is relevant, with a smaller number of neurons resulting in more efficient pattern separation (**Fig. 3.16b**). This finding is consistent with previous models, that emphasized the role of code expansion (Marr, 1969; Albus, 1971; Babadi and Sompolinsky, 2014; Cayco-Gajic et al., 2017). Second, the average EC–GC connectivity is important, with sparse connectivity enhancing pattern separation performance (**Fig. 3.16b**). Although this is also true for the cerebellum (Cayco-Gajic et al., 2017), the mechanisms may be different in the hippocampus, because GCs receive a much higher number of synaptic inputs (> 1,000; (Desmond and Levy, 1985; Schmidt-Hieber et al., 2007) compared to GCs in cerebellum (~5; (Cayco-Gajic et al., 2017)). Finally, a mix of structured and random EC–GC connectivity is optimal for the pattern separation mechanism (**Fig. 3.16d**).

However, the effects of these parameters on pattern separation efficacy are moderate. Thus, the rules of EC–GC connectivity, although important, are not the main determinants of pattern separation. Previous studies suggested a role of inhibition in pattern separation in the olfactory bulb of mammals and zebrafish and the equivalent mushroom body of Drosophila (Wiechert et al., 2010; Lin et al., 2014; Gschwend et al., 2015). Furthermore, a role of inhibition has been suggested in the hippocampus (Engin et al., 2015; Faghihi and Moustafa, 2015). In concordance with previous reports (Coultrip et al., 1992; Shoemaker, 2015), we show that lateral inhibition inserted into a biologically inspired network model of the dentate gyrus generates an efficient WTA mechanism, in which both excitatory EI synapses and inhibitory IE synapses are necessary for pattern separation (**Fig. 3.15c, d**).

Our results reveal two novel determinants of the efficacy of pattern separation. The first key factor is focal connectivity between PNs and INs, which substantially enhances pattern separation. This is counter-intuitive, because a long-range divergent output may be useful to suppress non-winners (Majani et al., 1988; Maass, 2000). However, our simulations show that networks with focal connectivity are much more effective than networks with wide connectivity (**Fig. 3.17b**). Furthermore, the pattern separation mechanism works well if the connectivity is asymmetric, with excitatory EI synapses showing narrower connectivity and inhibitory IE synapses wider connectivity, as observed experimentally. Intuitively, asymmetric connectivity avoids a situation in which the axon of the excitatory connection travels in one direction, and

that of the inhibitory connection travels oppositely. Such a connectivity pattern would fail to extend the range of lateral inhibition but would increase the total axonal wiring length involved in the disynaptic pathway, introducing unnecessary conduction delays into the circuit (**Fig. 3.17d**).

A second key factor is fast signaling in GABAergic cells. It is known that PV$^+$ interneurons express an extensive repertoire of fast biophysical signaling mechanisms at the level of synaptic input, action potential initiation, and synaptic output (Hu et al., 2014). Our results put these fast biophysical signaling mechanisms of PV$^+$ interneurons into the context of higher network computations.

What about the other mechanisms of pattern separation? Besides the expansion coding mechanism, provided by the EC–GCs connectivity and the WTA showed to be mediated by lateral inhibition, other mechanisms such as adult neurogenesis, thresholding and sparseness are thought to contribute to pattern separation. Thus, the prominent role of adult neurogenesis in pattern separation may be explained by preferential innervation to inhibitory synapses (Markwardt et al., 2009). However, this hypothesis is still controversial (Temprana et al., 2015) and require further validation. Regarding the thresholding mechanism, because together with inhibition directly affect the firing activity of PNs, their contribution is tightly related, as it was shown in our modeling work (**Fig 3,15a**). Finally, sparseness in the dentate gyrus is observed not only in the low spontaneous firing rate of GCs (Pernía-Andrade and Jonas, 2014) but also their connectivity, that as we showed nonexistent. A recent study in the cerebellum showed the importance of this mechanism for decorrelating input patterns (Cayco-Gajic et al., 2017). Thus, the whole architecture of the dentate gyrus seems to be maximally optimized for performing pattern separation.

Overall, from the results of our modeling work, we contribute to the emerging view that PV$^+$ interneurons are not only involved in basic microcircuit functions, such as feedforward and feedback inhibition but also contribute to higher-order computations in neuronal networks (Hu et al., 2014) with plausible behavioral implications. Consistent with this idea, we decided to make a further step and study how inhibition plays a role in pattern separation from a behavioral perspective.

4.4 Pattern separation in a behavioral paradigm

Pattern separation in the context of episodic memory is the ability to distinguish between similar experiences or events for the guidance of future adaptive behaviors (Leal and Yassa, 2018). In this regard, the nervous system needs to process highly complex information enriched in spatiotemporal, perceptual and motivational content, which occurs at different brain levels. Thus, memories with negative valence (associated to aversive emotions of experiences) are processed in the hippocampus and amygdala, which together create strong contextual memories with long-lasting periods of extinction (Chaaya et al., 2018). These properties together to their relatively simple implementation, make fear conditioning paradigms very suitable models for testing memory-related mechanisms (Tovote et al., 2015).

Therefore, for assessing pattern separation, we selected a behavioral task based on contextual fear discrimination that has also been previously validated by several groups (McHugh et al., 2007; Sahay et al., 2011; Choi et al., 2015; Engin et al., 2015). Previous studies have shown that contextual fear learning requires the hippocampus (ventral and dorsal), for processing the multisensorial information of the context, and the basolateral amygdala complex for the association with an unconditional stimulus (foot-shock) (Fanselow, 2009; Chaaya et al., 2018). The discrimination part of the task is dentate gyrus dependent. Our behavioral results show that silencing PV^+ interneuron activity in the dentate gyrus do not affect the acquisition and the consolidation of fear memories since during the training sessions no difference in freezing levels was observed between groups (**Fig. 3.18c, d**). This finding is concordant with the idea that contextual fear memory consolidation requires CA1 and CA3 but not the dentate gyrus (Chaaya et al., 2018).

In contrast, our data suggest that PV^+ interneurons may be involved in the discrimination between similar contexts when the exposition is acute (**Fig. 3.16e**). The role of inhibition in a pattern separation task has been previously explored by assessing contextual discrimination on knockout mice lacking the expression of the alpha 5 subunit of the GABA$_A$-Rs in GCs (α5DGKO mice) (Engin et al., 2015). Even though impairment in pattern separation was reported, the contribution of α subunit-containing GABA$_A$-Rs mediating either tonic or phasic inhibition is yet controversial

(Sun et al., 2018). Our results support the contribution of inhibition in pattern separation and additionally identify PV$^+$ interneurons as the direct mediators.

However, our paradigm is not exempt from disadvantages. We cannot ignore the effects of the aversive response on memory processing and excessive fear generalization may difficult the interpretation of our results. We observed that after the day 7 control mice drastically decreased the discrimination between the contexts (**Fig. 3.18f**). Thus, our paradigm does not allow us to exclude a further fear overgeneralization phenomenon by the foot-shock taking place during the consecutive testing days (**Fig. 3.18b, f**). Generalization is an adaptive mechanism that enables an organism to respond to novel and possible harmful experiences by extrapolating the features of a known threatened stimulus (pattern completion). Thus, this mechanism is oppositely related to pattern separation (in rodents and humans), suggesting that a loss of this balance could lead to pathological behaviors such as anxiety and posttraumatic disorders (Lange et al., 2017). More exhaustive behavioral paradigms are needed to clarify the effects of fear generalization and the long-term effects of inhibition on discrimination, when other simultaneous mechanisms of pattern separation may also be having a prominent role (e.g., plasticity (McHugh et al., 2007) and adult neurogenesis (Sahay et al., 2011)). Moreover, the assessment of pattern separation using novel object recognition based paradigms (van Hagen et al., 2015; van Goethem et al., 2018) could provide complementary information since they rely mostly on the natural curiosity of the mice, with the behavior not being affected by aversive responses.

What about the function of SST$^+$ and CCK$^+$ interneurons in the dentate gyrus? Besides pattern separation, the dentate gyrus is also involved in grid-to place code conversion and processing of context information (de Almeida et al., 2009; Kesner, 2018). Thus, SST$^+$ interneurons may coordinate the temporal activity of GCs that have been directed by activity patterns originated in the medial septum (Lovett-Barron et al., 2014), and control the size of engrams and the stability of associative memories (Stefanelli et al., 2016). Regarding specifically to contextual fear learning, in CA1, SST$^+$ interneurons provide the dendritic inhibition required for encoding conditioned stimulus during fear memory formation (Lovett-Barron et al., 2014). However, their contribution to the dentate gyrus has not been tested yet. In general, in the dentate gyrus, SST$^+$ interneurons are diverse, with different input-output projections and

plasticity properties, which makes them suitable for participating in various modalities of information processing (Yuan et al., 2017).

Regarding the activity of CCK$^+$ interneurons *in vivo*, less information is available. Nevertheless, their strong modulation by neurotransmitters related to motivational circuits (serotonin and cholinergic system) make them very suitable for participating in motivational aspects of the behavior. A recent article showed that the *in vivo* manipulation of the CCK$^+$ interneurons in the dentate gyrus affected the inhibition-excitation balance of the local circuit and modulate anxiety levels when mice performed in the forced swim test (Medrihan et al., 2017). Further research needs to be conducted to identify the role of different neuronal types and their precise form of interaction for allowing the emergence of specific behaviors.

Overall, the present results contribute to the emerging view that local connectivity rules are major determinants of higher computations in neuronal networks across multiple circuits. We provide experimental evidence supported by theoretical information showing that in the dentate gyrus GC–PV$^+$ interneuron connectivity rules provide the architectural structure for efficient pattern separation in the dentate gyrus. Besides, we showed for the first time the involvement of PV$^+$ interneurons in a behavioral task of pattern separation, which highlights the relevance of PV$^+$ interneurons for processing information with behavioral relevant consequences.

REFERENCES

Aimone JB, Deng W, Gage FH (2011) Resolving new memories: a critical look at the dentate gyrus, adult neurogenesis, and pattern separation. Neuron 70:589–596.

Albert R, Jeong H, Barabási AL (2000) Error and attack tolerance of complex networks. Nature 406:378–382.

Albus J (1971) A theory of cerebellar function. Math Biosci 10:25–61.

Amaral DG (1978) A golgi study of cell types in the hilar region of the hippocampus in the rat. J Comp Neurol 182:851–914.

Amaral DG, Scharfman HE, Lavenex P (2007) The dentate gyrus: fundamental neuroanatomical organization (dentate gyrus for dummies). Prog Brain Res 163:3–22.

Amit DJ, Gutfreund H, Sompolinsky H (1987) Statistical mechanics of neural networks near saturation. Ann Phys (N Y) 173:30–67.

Amrein I, Slomianka L, Lipp HP (2004) Granule cell number, cell death and cell proliferation in the dentate gyrus of wild-living rodents. Eur J Neurosci 20:3342–3350.

Andersen P (1975) Organization of the hippocampal neurons and their interconnections. In: The hippocampus (Isaacson RL, Pribram KH, eds). Springer, Boston, MA.

Babadi B, Sompolinsky H (2014) Sparseness and expansion in sensory representations. Neuron 83:1213–1226.

Barabási AL, Albert R (1999) Emergence of scaling in random networks. Science 286:509–512.

Bartos M, Elgueta C (2012) Functional characteristics of parvalbumin- and cholecystokinin-expressing basket cells. J Physiol 590:669–681.

Bartos M, Vida I, Frotscher M, Geiger JR, Jonas P (2001) Rapid signaling at inhibitory synapses in a dentate gyrus interneuron network. J Neurosci 21:2687–2698.

Bartos M, Vida I, Jonas P (2007) Synaptic mechanisms of synchronized gamma oscillations in inhibitory interneuron networks. Nat Rev Neurosci 8:45–56.

Bausch SB, He S, Yu D (2010) Inverse relationship between seizure expression and extrasynaptic NMDAR function following chronic NMDAR inhibition. Epilepsia 51:102–105.

Benjamini Y, Hochberg Y (1995) Controlling the false discovery rate: a practical and powerful approach to multiple testing. J Royal Stat Soc 57:289–300.

Billings G, Piasini E, Lorincz A, Nusser Z, Silver RA (2014) Network structure within the cerebellar input layer enables lossless sparse encoding. Neuron 83:960–974.

Bischofberger J, Engel D, Frotscher M, Jonas P (2006a) Timing and efficacy of transmitter release at mossy fiber synapses in the hippocampal network. Pflugers Arch 453:361–372.

Bischofberger J, Engel D, Li L, Geiger JRP, Jonas P (2006b) Patch-clamp recording from mossy fiber terminals in hippocampal slices. Nat Protoc 1:2075–2081.

Blackstad TW, Kjaerheim A (1961) Special axo-dendritic synapses in the hippocampal cortex: electron and light microscopic studies on the layer of mossy fibers. J Comp Neurol 117:133–159.

Bonifazi P, Goldin M, Picardo MA, Jorquera I, Cattani A, Bianconi G, Represa A, Ben-Ari Y, Cossart R (2009) GABAergic hub neurons orchestrate synchrony in developing hippocampal networks. Science 326:1419–1424.

Brunel N (2016) Is cortical connectivity optimized for storing information? Nat Neurosci 19:749–757.

Bullmore E, Sporns O (2009) Complex brain networks: Graph theoretical analysis of structural and functional systems. Nat Rev Neurosci 10:186–198.

Bullmore E, Sporns O (2012) The economy of brain network organization. Nat Rev Neurosci 13:336–349.

Butt SJB, Fuccillo M, Nery S, Noctor S, Kriegstein A, Corbin JG, Fishell G (2005) The temporal and spatial origins of cortical interneurons predict their physiological subtype. Neuron 48:591–604.

Buzsáki G (2015) Hippocampal sharp wave-ripple: a cognitive biomarker for episodic memory and planning. Hippocampus 1188:1073–1188.

Buzsáki G, Geisler C, Henze DA, Wang XJ (2004) Interneuron diversity series: circuit complexity and axon wiring economy of cortical interneurons. Trends Neurosci 27:186–193.

Buzsáki G, Mizuseki K (2014) The log-dynamic brain: how skewed distributions affect network operations. Nat Rev Neurosci 15:264–278.

Cayco-Gajic NA, Clopath C, Silver RA (2017) Sparse synaptic connectivity is required for decorrelation and pattern separation in feedforward networks. Nat Commun 8:1116.

Chaaya N, Battle AR, Johnson LR (2018) An update on contextual fear memory mechanisms: transition between amygdala and hippocampus. Neurosci Biobehav Rev 92:43–54.

Chavlis S, Poirazi P (2017) Pattern separation in the hippocampus through the eyes of computational modeling. Synapse 71.

Chen Y (2017) Mechanisms of winner-take-all and group selection in neuronal spiking networks. Front Comput Neurosci 11.

Chevaleyre V, Siegelbaum SA (2010) Strong CA2 pyramidal neuron synapses define a powerful disynaptic cortico-hippocampal loop. Neuron 66:560–572.

Choi S-Y, Han K, Cutforth T, Chung W, Park H, Lee D, Kim R, Kim M-H, Choi Y, Shen K, Kim E (2015) Mice lacking the synaptic adhesion molecule Neph2 / Kirrel3 display moderate hyperactivity and defective novel object preference. Front Cell Neurosci 9:283.

Chow SF, Wick SD, Riecke H (2012) Neurogenesis drives stimulus decorrelation in a model of the olfactory bulb. PLoS Comput Biol 8.

Clelland CD, Choi M, Romberg C, Clemenson, Jr GD, Fragniere A, Tyers P, Jessberger S, Saksida LM, Barker RA, Gage FH, Bussey TJ (2009) A functional role for adult hippocampal neurogenesis in spatial pattern separation. Science 325:210–213.

Clemenson GD, Lee SW, Deng W, Barrera VR, Iwamoto KS, Fanselow MS, Gage FH (2015) Enrichment rescues contextual discrimination deficit associated with immediate shock. Hippocampus 25:385–392.

Cohen MR, Maunsell JHR (2009) Attention improves performance primarily by reducing interneuronal correlations. Nat Neurosci 12:1594–1600.

Cossell L, Iacaruso MF, Muir DR, Houlton R, Sader EN, Ko H, Hofer SB, Mrsic-Flogel TD (2015) Functional organization of excitatory synaptic strength in primary visual cortex. Nature 518:399–403.

Couey JJ, Witoelar A, Zhang SJ, Zheng K, Ye J, Dunn B, Czajkowski R, Moser MB, Moser EI, Roudi Y, Witter MP (2013) Recurrent inhibitory circuitry as a mechanism for grid formation. Nat Neurosci 16:318–324.

Coultrip R, Granger R, Lynch G (1992) A cortical model of winner-take-all competition via lateral inhibition. Neural Networks 5:47–54.

Curzon P, Rustay NR, Browman KE (2009) Chapter 2: cued and contextual fear conditioning for rodents. In: Methods of Behavior Analysis in Neuroscience, Second. (Boca R, ed). Boca Raton (FL): CRC Press/Taylor & Francis.

Cushman JD, Maldonado J, Kwon EE, Garcia AD, Fan G, Imura T, Sofroniew M V., Fanselow MS (2012) Juvenile neurogenesis makes essential contributions to adult brain structure and plays a sex-dependent role in fear memories. Front Behav Neurosci 6:3.

D'Huys O, Vicente R, Erneux T, Danckaert J, Fischer I (2016) Synchronization properties of network motifs: influence of coupling delay and symmetry. Chaos 18:037116.

Danielson NB, Turi GF, Ladow M, Chavlis S, Petrantonakis PC, Poirazi P, Losonczy A (2017) In vivo imaging of dentate gyrus mossy cells in behaving mice. Neuron 93:552–559.

Davis P, Zaki Y, Maguire J, Reijmers LG (2017) Cellular and oscillatory substrates of fear extinction learning. Nat Neurosci 20:1624–1633.

de Almeida L, Idiart M, Lisman JE (2009) A second function of gamma frequency oscillations: an E%-max winner-take-all mechanism selects which cells fire. J Neurosci 29:7497–7503.

De la Rocha J, Doiron B, Shea-Brown E, Josić K, Reyes A (2007) Correlation between neural spike trains increases with firing rate. Nature 448:802–807.

Dere E, Huston JP, De Souza Silva MA (2005) Integrated memory for objects, places, and temporal order: Evidence for episodic-like memory in mice. Neurobiol Learn Mem 84:214–221.

Desmond NL, Levy WB (1985) Granule cell dendritic spine density in the rat hippocampus varies with spine shape and location. Neurosci Lett 54:219–224.

Doischer D, Hosp JA, Yanagawa Y, Obata K, Jonas P, Vida I, Bartos M (2008) Postnatal differentiation of basket cells from slow to fast signaling devices. J Neurosci 28:12956–12968.

Douglas R, Koch J, Mahowald M, Martin K, Suarez H (1995) Recurrent excitation in neocortical circuits. Science 269:981–985.

Ecker AS, Berens P, Keliris GA, Bethge M, Logothetis N, Tolias AS (2010) Decorrelated neuronal firing in cortical microcircuits. Science 327:584–587.

Efron B, Tibshirani RJ (1998) An introduction to the bootstrap. London: Chapman and Hall/CRC.

Eichenbaum H (2017) On the integration of space, time, and memory. Neuron 95:1007–1018.

Engin E, Zarnowska ED, Benke D, Tsvetkov E, Sigal M, Keist R, Bolshakov VY, Pearce RA, Rudolph U (2015) Tonic inhibitory control of dentate gyrus granule cells by α5-containing $GABA_A$ receptors reduces memory interference. J Neurosci 35:13698–13712.

Erdös P, Rényi A (1959) On random graphs I. Publ Math 6:290–297.

Ermentrout B (1996) Type I membranes, phase ressetting curves, and synchrony. Neural Comput 8:979–1001.

Ermentrout GB, Cowan JD (1979) A mathematical theory of visual hallucination patterns. Biol Cybern 34:137–150.

Euler L (1736) Solutio problematis ad geometrian situs pertinentis. Coment Acad Sci Imp petropolitanae 8:128–140.

Euler T, Haverkamp S, Schubert T, Baden T (2014) Retinal bipolar cells : elementary building blocks of vision. Nat Rev Neurosci 15:507–519.

Faghihi F, Moustafa AA (2015) A computational model of pattern separation efficiency in the dentate gyrus with implications in schizophrenia. Front Syst Neurosci 9:42.

Fanselow MS (2009) From contextual fear to a dynamic view of memory systems. Trends Cogn Sci 14:7:14.

Fanselow MS, Dong HW (2010) Are the dorsal and ventral hippocampus functionally distinct structures? Neuron 65:1–25.

França TFA, Bitencourt AM, Maximilla NR, Barros DM, Monserrat JM (2017) Hippocampal neurogenesis and pattern separation: a meta-analysis of behavioral data. Hippocampus 27:937–950.

Freeman WJ, Breakspear M (2007) Scale-free neocortical dynamics. Scholarpedia 2(2)1357.

Freund TF, Buzsáki G (1996) Interneurons of the hippocampus. Hippocampus 6:347–470.

Friedrich RW, Wiechert MT (2014) Neuronal circuits and computations: pattern decorrelation in the olfactory bulb. FEBS Lett 588:2504–2513.

Galarreta M, Hestrin S (1999) A network of fast-spiking cells in the neocortex connected by electrical synapses. Nature 402:72–75.

Galarreta M, Hestrin S (2001) Spike transmission and synchrony detection in networks of GABAergic interneurons. Science 292:2295–2299.

Geiger JRP, Lübke J, Roth A, Frotscher M, Jonas P (1997) Submillisecond AMPA receptor-mediated signaling at a principal neuron- interneuron synapse. Neuron 18:1009–1023.

Gilbert PE, Kesner RP, Lee I (2001) Dissociating hippocampal subregions: a double dissociation between dentate gyrus and CA1. Hippocampus 11:626–636.

Glickfeld LL, Scanziani M (2006) Distinct timing in the activity of cannabinoid-sensitive and cannabinoid-insensitive basket cells. Nat Neurosci 9:807–815.

Gomez JL, Bonaventura J, Lesniak W, Mathews WB, Sysa-Shah P, Rodriguez LA, Ellis RJ, Richie CT, Harvey BK, Dannals RF, Pomper MG, Bonci A, Michaelides M (2017) Chemogenetics revealed: DREADD occupancy and activation via converted clozapine. Science 357:503–507.

GoodSmith D, Chen X, Wang C, Kim SH, Song H, Burgalossi A, Christian KM, Knierim JJ (2017) Spatial representations of granule cells and mossy cells of the dentate gyrus. Neuron 93:677–690.

Groves JO, Leslie I, Huang G-J, McHugh SB, Taylor A, Mott R, Munafò M, Bannerman DM, Flint J (2013) Ablating adult neurogenesis in the rat has no effect on spatial processing: evidence from a novel pharmacogenetic model. PLoS Genet 9:e1003718.

Gschwend O, Abraham NM, Lagier S, Begnaud F, Rodriguez I, Carleton A (2015) Neuronal pattern separation in the olfactory bulb improves odor discrimination learning. Nat Neurosci 18:1474–1482.

Gulyás AI, Megías M, Emri Z, Freund TF (1999) Total number and ratio of excitatory and inhibitory synapses converging onto single interneurons of different types in the CA1 area of the rat hippocampus. J Neurosci 19:10082–10097.

Guzman SJ, Schlögl A, Frotscher M, Jonas P (2016) Synaptic mechanisms of pattern completion in the hippocampal CA3 network. Science 353:1117–1123.

Guzman SJ, Schlögl A, Schmidt-Hieber C (2014) Stimfit: quantifying electrophysiological data with Python. Front Neuroinform 8:1–10.

Han Z, Buhl EH, Lörinczi Z, Somogyi P (1993) A high degree of spatial selectivity in the axonal and dendritic domains of physiologically identified local- circuit neurons in the dentate gyrus of the rat hippocampus. Eur J Neurosci 5:395–410.

Harris EW, Carl WC (1986) Long-term potentiation of guinea pig mossy fiber responses is not blocked by N-methyl D-aspartate antagonists. Neurosci Lett 7:132–137.

Hefft S, Jonas P (2005) Asynchronous GABA release generates long-lasting inhibition at a hippocampal interneuron-principal neuron synapse. Nat Neurosci 8:1319–1328.

Hitti FL, Siegelbaum SA (2014) The hippocampal CA2 region is essential for social memory. Nature 508:88–92.

Holmgren C, Harkany T, Svennenfors B, Zilberter Y (2003) Pyramidal cell communication within local networks in layer 2/3 of rat neocortex. J Physiol 551:139–153.

Hopfield JJ (1982) Neural networks and physical systems with emergent collective computational abilities. Proc Natl Acad Sci 79:2554–2558.

Hosp JA, Strüber M, Yanagawa Y, Obata K, Vida I, Jonas P, Bartos M (2014) Morpho-physiological criteria divide dentate gyrus interneurons into classes. Hippocampus 24:189–203.

Houser CR (2007) Interneurons of the dentate gyrus: an overview of cell types, terminal fields and neurochemical identity. Prog Brain Res 163:217–233.

Hu H, Gan J, Jonas P (2014) Fast-spiking, parvalbumin+ GABAergic interneurons: from cellular design to microcircuit function. Science 345:1255263.

Hu H, Jonas P (2014) A supercritical density of Na+ channels ensures fast signaling in GABAergic interneuron axons. Nat Neurosci 17:686–693.

Huckleberry KA, Ferguson LB, Drew MR (2016) Behavioral mechanisms of context fear generalization in mice. Learn Mem 23:703–709.

Jeanne JM, Wilson RI (2015) Convergence, divergence, and reconvergence in a feedforward network improves neural speed and accuracy. Neuron 88:1014–1026.

Johnston ST, Shtrahman M, Parylak S, Gonçalves JT, Gage FH (2016) Paradox of pattern separation and adult neurogenesis: a dual role for new neurons balancing memory resolution and robustness. Neurobiol Learn Mem 129:60–68.

Jonas P, Buzsáki G (2007) Neural inhibition. Scholarpedia 2(9)3286.

Jonas P, Lisman JE (2014) Structure, function, and plasticity of hippocampal dentate gyrus microcircuits. Front Neural Circuits 8:2013–2014.

Jouhanneau J-S, Kremkow J, Dorrn ALL, Poulet JFA (2015) In vivo monosynaptic excitatory transmission between layer 2 cortical pyramidal neurons. Cell Rep 13:2098–2106.

Jouhanneau J-S, Kremkow J, Poulet JFA (2018) Single synaptic inputs drive high-precision action potentials in parvalbumin expressing GABA-ergic cortical neurons in vivo. Nat Commun 9:1540.

Katona I, Sperlágh B, Sík A, Käfalvi A, Vizi ES, Mackie K, Freund TF (1999) Presynaptically located CB1 cannabinoid receptors regulate GABA release from axon terminals of specific hippocampal internenurons. J Neurosci 19:4544–4558.

Kepecs A, Fishell G (2014) Interneuron cell types are fit to function. Nature 505:318–326.

Kesner RP (2018) An analysis of dentate gyrus function (an update). Behav Brain Res 354:84–91.

Kesner RP, Rolls ET (2015) A computational theory of hippocampal function, and tests of the theory: new developments. Neurosci Biobehav Rev 48:92–147.

Khan AG, Poort J, Chadwick A, Blot A, Sahani M, Mrsic-Flogel TD, Hofer SB (2018) selectivity and interactions of GABAergic interneuron classes in visual cortex. Nat Neurosci 21:851–859.

Kitamura T, Sun C, Kitch LJ, Mark J, Kitamura T, Sun C, Martin J, Kitch LJ, Schnitzer MJ, Tonegawa S (2015) Entorhinal cortical ocean cells encode specific contexts and drive context-specific fear memory. Neuron 87:1317–1331.

Klausberger T, Marton LF, O'Neill J, Huck JHJ, Dalezios Y, Fuentealba P, Suen WY, Papp E, Kaneko T, Watanabe M, Csicsvari J, Somogyi P (2005) Complementary roles of cholecystokinin- and parvalbumin-expressing GABAergic neurons in hippocampal network oscillations. J Neurosci 25:9782–9793.

Klausberger T, Somogyi P (2008) Neuronal diversity and temporal dynamics: the unity of hippocampal circuit operations. Science 321:53–57.

Ko H, Hofer SB, Pichler B, Buchanan K, Sjöström PJ, Mrsic-Flogel TD (2011) Functional specificity of local synaptic connections in neocortical networks. Nature 473:87–91.

Lange I, Goossens L, Michielse S, Bakker J, Lissek S, Papalini S, Verhagen S, Leibold N, Marcelis M, Wichers M, Lieverse R, van Os J, van Amelsvoort T, Schruers K (2017) Behavioral pattern separation and its link to the neural mechanisms of fear generalization. Soc Cogn Affect Neurosci 12:1720–1729.

Larimer P, Strowbridge BW (2008) Nonrandom local circuits in the dentate gyrus. J Neurosci 28:12212–12223.

Leal SL, Yassa MA (2018) Integrating new findings and examining clinical applications of pattern separation. Nat Neurosci 21:163–173.

Lee SH, Kwan AC, Zhang S, Phoumthipphavong V, Flannery JG, Masmanidis SC, Taniguchi H, Huang ZJ, Zhang F, Boyden ES, Deisseroth K, Dan Y (2012) Activation of specific interneurons improves V1 feature selectivity and visual perception. Nature 488:379–383.

Lee WA, Bonin V, Reed M, Graham BJ, Hood G, Glattfelder K, Reid RC (2016) Anatomy and function of an excitatory network in the visual cortex. Nature 532:370–374.

Leranth C, Hajszan T (2007) Extrinsic afferent systems to the dentate gyrus. Prog Brain Res 163:63–85.

Leroy F, Park J, Asok A, Brann DH, Meira T, Boyle LM, Buss EW, Kandel ER, Siegelbaum SA (2018) A circuit from hippocampal CA2 to lateral septum disinhibits social aggression. Nature 564:213–218.

Letzkus JJ, Wolff SBE, Meyer EMM, Tovote P, Courtin J, Herry C, Lüthi A (2011) A disinhibitory microcircuit for associative fear learning in the auditory cortex. Nature 480:331–335.

Leutgeb JK, Leutgeb S, Moser M, Moser EI, Moser I (2007) Pattern separation in the dentate gyrus and CA3 of the hippocampus. Science 315:961–966.

Levy RB, Reyes AD (2012) Spatial profile of excitatory and inhibitory synaptic connectivity in mouse primary auditory cortex. J Neurosci 32:5609–5619.

Lin AC, Bygrave AM, De Calignon A, Lee T, Miesenböck G (2014) Sparse, decorrelated odor coding in the mushroom body enhances learned odor discrimination. Nat Neurosci 17:559–568.

Lovett-Barron M, Kaifosh P, Kheirbek MA, Danielson NB, Zaremba JD, Turi GF, Hen R, Zemelman B V, Losonczy A (2014) Dendritic inhibition in the hippocampus supports fear learning. Science 343:857–864.

Lovett-Barron M, Turi GF, Kaifosh P, Lee PH, Bolze F, Sun X, Nicoud J, Zemelman B V, Sternson SM, Losonczy A (2012) Regulation of neuronal input transformations by tunable dendritic inhibition. Nat Neurosci 15:423–430.

Maass W (2000) On the computational power of winner-take-all. Neural Comput 12:2519–2535.

Majani E, Erlarson R, Abu-Mostafa Y (1988) On the k-winners-takes-all network. Adv Neural Inf Process Syst I:634–642.

Marek R, Jin J, Goode TD, Giustino TF, Wang Q, Acca GM, Holehonnur R, Ploski JE, Fitzgerald PJ, Lynagh T, Lynch JW, Maren S, Sah P (2018) Hippocampus-driven feed-forward inhibition of the prefrontal cortex mediates relapse of extinguished fear. Nat Neurosci 21:384–392.

Markram H (1997) A Network of tufted layer 5 pyramidal neurons. Cereb Cortex 7:523–533.

Markwardt SJ, Wadiche JI, Overstreet-Wadiche LS (2009) Input-specific GABAergic signaling to newborn neurons in adult dentate gyrus. J Neurosci 29:15063–15072.

Marr D (1969) A theory of cerebellar cortex. J Physiol 202:437–470.

Marr D (1971) Simple memory: a theory for archicortex. Philos Trans R Soc B Biol Sci 262:23–81.

Mátyás F, Freund TF, Gulyás AI (2004) Convergence of excitatory and inhibitory inputs onto CCK-containing basket cells in the CA1 area of the rat hippocampus. Eur J Neurosci 19:1243–1256.

McHugh TJ, Jones MW, Quinn JJ, Balthasar N, Coppari R, Elmquist JK, Lowell BB, Fanselow MS, Wilson MA, Tonegawa S (2007) Dentate gyrus NMDA receptors mediate rapid pattern separation in the hippocampal network. Science 317:94–100.

McNaughton LB, Morris MRG (1987) Hippocampal synaptic enhancement and information storage within a distributed memory system. TINS 10:408–415.

Medrihan L, Sagi Y, Inde Z, Krupa O, Daniels C, Peyrache A, Greengard P (2017) Initiation of behavioral response to antidepressants by cholecystokinin neurons of the dentate gyrus. Neuron 95:564–576.

Mesulam M (1998) From sensation to cognition. Brain 121:1013–1052.

Miles R (1990) Synaptic excitation of inhibitory cells by single CA3 hippocampal pyramidal cells of the guinea-pig in vitro. J Physiol 428:61–77.

Mott DD, Turner DA, Okazaki MM, Lewis D (1997) Interneurons of the dentate-hilus border of the rat dentate gyrus: morphological and electrophysiological heterogeneity. J Neurosci 17:3990–4005.

Myers CE, Scharfman HE (2009) A role for hilar cells in pattern separation in the dentate gyrus: a computational approach. Hippocampus 19:321–337.

Nakashiba T, Cushman JD, Pelkey KA, Renaudineau S, Buhl DL, McHugh TJ, Barrera VR, Chittajallu R, Iwamoto KS, McBain CJ, Fanselow MS, Tonegawa S (2012) Young dentate granule cells mediate pattern separation, whereas old granule cells facilitate pattern completion. Cell 149:188–201.

Neves G, Cooke SF, Bliss TVP (2012) Synaptic plasticity, memory and the hippocampus: a neural network approach to causality. Nat Rev Neurosci 9:65–75.

Nörenberg A, Hu H, Vida I, Bartos M, Jonas P (2010) Distinct nonuniform cable properties optimize rapid and efficient activation of fast-spiking GABAergic interneurons. Proc Natl Acad Sci 107:894–899.

O'Reilly RCO, McClelland JL (1994) Hippocampal conjunctive encoding, storage, and recall: avoiding a trade-off. Hippocampus 4:661–682.

Obermayer J, Heistek TS, Kerkhofs A, Goriounova NA, Kroon T, Baayen JC, Idema S, Testa-Silva G, Couey JJ, Mansvelder HD (2018) Lateral inhibition by Martinotti interneurons is facilitated by cholinergic inputs in human and mouse neocortex. Nat Commun 9:4101.

Olshausen BA, Field DJ (2004) Sparse coding of sensory inputs. Curr Opin Neurobiol 14:481–487.

Oswald A-MM, Doiron B, Rinzel J, Reyes AD (2009) Spatial profile and differential recruitment of $GABA_B$ modulate oscillatory activity in auditory cortex. J Neurosci 29:10321–10334.

Packer AM, Yuste R (2011) Dense, unspecific connectivity of neocortical parvalbumin-positive interneurons: a canonical microcircuit for inhibition? J Neurosci 31:13260–13271.

Pala A, Petersen CCH (2015) In vivo measurement of cell-type-specific synaptic connectivity and synaptic transmission in layer 2/3 mouse barrel cortex. Neuron 85:68–76.

Passingham RE, Stephan KE, Kötter R (2002) The anatomical basis of functional localization in the cortex. Nat Rev Neurosci 3:606–616.

Peng Y, Tomás FJB, Klisch C, Vida I, Geiger JRP (2017) Layer-specific organization of local excitatory and inhibitory synaptic connectivity in the rat presubiculum. Cereb Cortex 27:2435–2452.

Perin R, Berger TK, Markram H (2011) A synaptic organizing principle for cortical neuronal groups. Proc Natl Acad Sci 108:5419–5424.

Pernía-Andrade AJ, Jonas P (2014) Theta-gamma-modulated synaptic currents in hippocampal granule cells in vivo define a mechanism for network oscillations. Neuron 81:140–152.

Pfeffer CK, Xue M, He M, Huang ZJ, Scanziani M (2013) Inhibition of inhibition in visual cortex: the logic of connections between molecularly distinct interneurons. Nat Neurosci 16:1068–1076.

Pilz G-A, Carta S, Stauble A, Ayaz A, Jessberger S, Helmchen F (2016) Functional imaging of dentate granule cells in the adult mouse hippocampus. J Neurosci 36:7407–7414.

Prill RJ, Iglesias PA, Levchenko A (2005) Dynamic properties of network motifs contribute to biological network organization. PLoS Biol 3:e343.

Ramón y Cajal S (1911) Histologie du système nerveux de l'homme et des vertébrés.

Rieubland S, Roth A, Häusser M (2014) Structured connectivity in cerebellar inhibitory networks. Neuron 81:913–929.

Rolls ET (2013) The mechanisms for pattern completion and pattern separation in the hippocampus. Front Syst Neurosci 7:1–21.

Rolls ET (2016) Pattern separation, completion, and categorisation in the hippocampus and neocortex. Neurobiol Learn Mem 129:4–28.

Royer S, Zemelman B V., Losonczy A, Kim J, Chance F, Magee JC, Buzsáki G (2012) Control of timing, rate and bursts of hippocampal place cells by dendritic and somatic inhibition. Nat Neurosci 15:769–775.

Sahay A, Scobie KN, Hill AS, O'Carroll CM, Kheirbek MA, Burghardt NS, Fenton AA, Dranovsky A, Hen R (2011) Increasing adult hippocampal neurogenesis is sufficient to improve pattern separation. Nature 472:466–473.

Savanthrapadian S, Meyer T, Elgueta C, Booker SA, Vida I, Bartos M (2014) Synaptic properties of SOM- and CCK-expressing cells in dentate gyrus interneuron networks. J Neurosci 34:8197–8209.

Scharfman HE, Kunkel DD, Schwartzkroin PA (1990) Synaptic connections of dentate granule cells and hilar neurons: results of paired intracellular recordings and intracellular horseradish peroxidase injections. Neuroscience 37:693–707.

Schmidt-Hieber C, Jonas P, Bischofberger J (2004) Enhanced synaptic plasticity in newly generated granule cells of the adult hippocampus. Nature 429:184–187.

Schmidt-Hieber C, Jonas P, Bischofberger J (2007) Subthreshold dendritic signal processing and coincidence detection in dentate gyrus granule cells. J Neurosci 27:8430–8441.

Schröter M, Paulsen O, Bullmore ET (2017) Micro-connectomics: probing the organization of neuronal networks at the cellular scale. Nat Rev Neurosci 18:131–146.

Senzai Y, Buzsáki G (2017) Physiological properties and behavioral correlates of hippocampal granule cells and mossy cells. Neuron 93:691–704.

Shimono M, Beggs JM (2015) Functional clusters, hubs, and communities in the cortical microconnectome. Cereb Cortex 25:3743–3757.

Shoemaker PA (2015) Neuronal networks with NMDARs and lateral inhibition implement winner-takes-all. Front Comput Neurosci 9:1–13.

Sik A, Penttonen M, Buzsáki G (1997) Interneurons in the hippocampal dentate gyrus: an in vivo intracellular study. Eur J Neurosci 9:573–588.

Silberberg G, Markram H (2007) Disynaptic inhibition between neocortical pyramidal cells mediated by martinotti cells. Neuron 53:735–746.

Sippy T, Yuste R (2013) Decorrelating action of inhibition in neocortical networks. J Neurosci 33:9813–9830.

Somogyi J, Baude Á, Omori Y, Shimizu H, Mestikawy S El, Fukaya M, Shigemoto R, Watanabe M, Somogyi P (2004) GABAergic basket cells expressing cholecystokinin contain vesicular glutamate transporter type 3 (VGLUT3) in their synaptic terminals in hippocampus and isocortex of the rat. Eur J Neurosci 19:552–569.

Song HF, Wang XJ (2014) Simple, distance-dependent formulation of the Watts-Strogatz model for directed and undirected small-world networks. Phys Rev E - Stat Nonlinear, Soft Matter Phys 90:1–5.

Song S, Sjöström PJ, Reigl M, Nelson S, Chklovskii DB (2005) Highly nonrandom features of synaptic connectivity in local cortical circuits. PLoS Biol 3:0507–0519.

Sporns O (2011) Networks of the brain, MIT press. Cambridge, Massachussetts.

Sporns O (2018) Graph theory methods: applications in brain networks. Dialogues Clin Neurosci 20:111–121.

Stam FJ, Callaway EM, Goulding M, Li Y, Gage FH, Aimone JB (2013) Molecular layer perforant path-associated cells contribute to feed-forward inhibition in the adult dentate gyrus. Proc Natl Acad Sci 110:9106–9111.

Stefanelli T, Lüscher C, Bertollini C, Muller D, Mendez P (2016) Hippocampal somatostatin interneurons control the size of neuronal memory ensembles. Neuron 89:1074–1085.

Sterling P, Laughlin S (2015) Principles of neural design. Massachusetts: MIT Press.

Strange BA, Witter MP, Lein ES, Moser EI (2014) Functional organization of the hippocampal longitudinal axis. Nat Rev Neurosci 15:655–669.

Strüber M, Sauer JF, Jonas P, Bartos M (2017) Distance-dependent inhibition facilitates focality of gamma oscillations in the dentate gyrus. Nat Commun 8:758.

Suh J, Rivest AJ, Nakashiba T, Tominaga T, Tonegawa S (2011) Entorhinal cortex layer III input to the hippocampus is crucial for temporal association memory. Science 334:1415–1421.

Sun XM, Shu H, Benz A, Bracamontes J, Akk XG, Zorumski CF, Steinbach JH, Mennerick XSJ (2018) Chemogenetic isolation reveals synaptic contribution of δ GABA$_A$ receptors in mouse dentate granule neurons. J Neurosci 38:8128–8145.

Takesian AE, Bogart LJ, Lichtman JW, Hensch TK (2018) Inhibitory circuit gating of auditory critical-period plasticity. Nat Neurosci 21:218–227.

Tallent MK (2007) Somatostatin in the dentate gyrus. Prog Brain Res 163:265–284.

Tamamaki N, Nojyo Y (1993) Projection of the entorhinal layer II neurons in the rat as revealed by intracellular pressure-injection of neurobiotin. Hippocampus 3:471–480.

Taniguchi H, He M, Wu P, Kim S, Paik R, Sugino K, Kvitsani D, Fu Y, Lu J, Lin Y, Miyoshi G, Shima Y, Fishell G, Nelson SB, Huang ZJ (2011) A resource of Cre driver lines for genetic targeting of GABAergic neurons in cerebral cortex. Neuron 71:995–1013.

Temprana SG, Mongiat LA, Yang SM, Trinchero MF, Alvarez DD, Kropff E, Giacomini D, Beltramone N, Lanuza GM, Schinder AF (2015) Delayed coupling to feedback inhibition during a critical period for the integration of adult-born granule cells. Neuron 85:116–131.

Tetzlaff T, Helias M, Einevoll GT, Diesmann M (2012) Decorrelation of neural-network activity by inhibitory feedback. PLoS Comput Biol 8:e1002596.

Tovote P, Fadok JP, Lüthi A (2015) Neuronal circuits for fear and anxiety. Nat Rev Neurosci 16:317–331.

Tozzi A, Peters JF (2018) Multidimensional brain activity dictated by winner-take-all mechanisms. Neurosci Lett 678:83–89.

Treves A, Rolls ET (1992) Computational constraints suggest the need for two distinct input systems to the hippocampal CA3 network. Hippocampus 2:189–199.

Urban-Ciecko J, Barth AL (2016) Somatostatin-expressing neurons in cortical networks. Nat Rev Neurosci 17:401–409.

Valero M, Cid E, Averkin RG, Aguilar J, Sanchez-Aguilera A, Viney TJ, Gomez-Dominguez D, Bellistri E, Menendez L, Prida D (2015) Determinants of different deep and superficial CA1 pyramidal cell dynamics during sharp-wave ripples. Nat Neurosci 18:1281–1290.

van Goethem NP, van Hagen BTJ, Prickaerts J (2018) Assessing spatial pattern separation in rodents using the object pattern separation task. Nat Protoc 13:1763–1792.

van Hagen BTJ, van Goethem NP, Lagatta DC, Prickaerts J (2015) The object pattern separation (OPS) task: A behavioral paradigm derived from the object recognition task. Behav Brain Res 285:44–52.

Wang X-J, Buzsáki G (1996) Gamma oscillation by synaptic inhibition in a hippocampal interneuronal network model. J Neurosci 16:6402–6413.

Wang X (2002) Probabilistic decision making by slow reverberation in cortical circuits. Neuron 36:955–968.

Watts DJ, Strogatz SH (1998) Collectivedynamics of "small-world" networks. Nature 393:440–442.

Wiechert MT, Judkewitz B, Riecke H, Friedrich RW (2010) Mechanisms of pattern decorrelation by recurrent neuronal circuits. Nat Neurosci 13:1003–1010.

Wiegert JS, Mahn M, Prigge M, Printz Y, Yizhar O (2017) Silencing neurons: tools, applications, and experimental constraints. Neuron 95:504–529.

Wilson NR, Runyan CA, Wang FL, Sur M (2012) Division and subtraction by distinct cortical inhibitory networks in vivo. Nature 488:343–348.

Witter MP (2007) The perforant path: projections from the entorhinal cortex to the dentate gyrus. Prog Brain Res 163:43–61.

Witter MP, Doan TP, Jacobsen B, Nilssen ES, Ohara S (2017) Architecture of the entorhinal cortex a review of entorhinal anatomy in rodents with some comparative notes. Front Syst Neurosci 11:1–12.

Wolff SBE, Gründemann J, Tovote P, Krabbe S, Jacobson GA, Mu C, Herry C, Ehrlich I, Friedrich RW, Letzkus JJ, Lüthi A (2014) Amygdala interneuron subtypes control fear learning through disinhibition. Nature 509:453–574.

Xia F, Richards BA, Tran MM, Josselyn SA (2017) Parvalbumin-positive interneurons mediate neocortical-hippocampal interactions that are necessary for memory consolidation. Elife 6:e27868.

Xu Q, Cobos I, De La Cruz E, Rubenstein JL, Anderson SA (2004) Origins of cortical interneuron subtypes. J Neurosci 24:2612–2622.

Yoshimura Y, Dantzker JLM, Callaway EM (2005) Excitatory cortical neurons from fine-scale functional networks. Nature 5:2005–2005.

Yuan M, Meyer T, Benkowitz C, Savanthrapadian S, Ansel-bollepalli L, Foggetti A, Wulff P, Alcami P, Elgueta C, Bartos M (2017) Somatostatin-positive interneurons in the dentate gyrus of mice provide local- and long-range septal synaptic inhibition. Elife 6:e21105.

Zeng H, Sanes JR (2017) Neuronal cell-type classification: challenges, opportunities and the path forward. Nat Rev Neurosci 18:530–546.

Zhao L, Beverlin B, Netoff T, Nykamp DQ (2011) Synchronization from second order network connectivity statistics. Front Comput Neurosci 5:1–16.

Zhigulin VP (2004) Dynamical motifs: building blocks of complex dynamics in sparsely connected random networks. Phys Rev Lett 92:238701.

Parvalbumin$^+$ interneurons obey unique connectivity rules and establish a powerful lateral-inhibition microcircuit in dentate gyrus

Claudia Espinoza [1], Segundo Jose Guzman [2], Xiaomin Zhang[1] & Peter Jonas [1]

Parvalbumin-positive (PV$^+$) GABAergic interneurons in hippocampal microcircuits are thought to play a key role in several higher network functions, such as feedforward and feedback inhibition, network oscillations, and pattern separation. Fast lateral inhibition mediated by GABAergic interneurons may implement a winner-takes-all mechanism in the hippocampal input layer. However, it is not clear whether the functional connectivity rules of granule cells (GCs) and interneurons in the dentate gyrus are consistent with such a mechanism. Using simultaneous patch-clamp recordings from up to seven GCs and up to four PV$^+$ interneurons in the dentate gyrus, we find that connectivity is structured in space, synapse-specific, and enriched in specific disynaptic motifs. In contrast to the neocortex, lateral inhibition in the dentate gyrus (in which a GC inhibits neighboring GCs via a PV$^+$ interneuron) is ~10-times more abundant than recurrent inhibition (in which a GC inhibits itself). Thus, unique connectivity rules may enable the dentate gyrus to perform specific higher-order computations.

---

[1] IST Austria (Institute of Science and Technology Austria), Am Campus 1, 3400 Klosterneuburg, Austria. [2] Present address: Institute for Molecular Biotechnology (IMBA), Dr. Bohr-Gasse 3, 1030 Wien, Austria. Correspondence and requests for materials should be addressed to P.J. (email: peter.jonas@ist.ac.at)

Throughout the brain, fast-spiking, parvalbumin-expressing (PV$^+$) GABAergic interneurons play a key role in several higher functions, such as feedforward and feedback inhibition, high-frequency network oscillations, and pattern separation[1]. Understanding how PV$^+$ interneurons contribute to these complex computations requires a detailed and quantitative analysis of their synaptic connectivity. While early studies suggested that connectivity of PV$^+$ interneurons is random[2], more recent work highlighted several specific connectivity rules[3–7] (Supplementary Table 1). Analysis of principal neuron (PN)–interneuron (IN) connectivity in the neocortex revealed that reciprocally connected pairs occurred much more frequently than expected in a random network[3–7]. Moreover, synaptic strength appeared to be higher in these reciprocally connected motifs[4,6]. Whether these connectivity rules also apply in other microcircuits, such as the hippocampus, has not been determined yet.

Pattern separation is a fundamental network computation in which PV$^+$ interneurons are likely to be involved. Pattern separation is thought to be particularly important in the dentate gyrus, where conversion of overlapping synaptic input patterns into non-overlapping action potential (AP) output patterns[8–12] may facilitate reliable storage of information in the downstream CA3 network[9,13,14]. Previous studies suggested a model of pattern separation based on a winner-takes-all mechanism mediated by feedback inhibition[15–19]. Such a model has received experimental support in the olfactory system[20–22]. While some studies suggested that similar mechanisms may operate in the dentate gyrus[23,24], it is not clear whether the rules of PN–IN connectivity are adequate to support such a model. Specifically, two forms of feedback inhibition need to be distinguished: recurrent inhibition, in which an active PN inhibits itself via reciprocal PN–IN connections, and lateral inhibition, in which an active PN inhibits neighboring PNs but not itself[25,26]. A winner-takes-all mechanism likely requires lateral inhibition; recurrent inhibition may be counter-productive, because it could suppress potential winners[17,26,27]. However, in both neocortex and brain areas directly connected to the hippocampus, recurrent inhibition and lateral inhibition are equally abundant[3–7] (Supplementary Table 1). Such a circuit design would seem incompatible with efficient pattern separation.

To resolve this apparent contradiction, we examined the functional connectivity rules in PN–IN networks in the dentate gyrus, using simultaneous recordings from up to seven granule cells (GCs) and up to four GABAergic interneurons. Our experiments reveal a uniquely high abundance of lateral inhibition mediated by PV$^+$ interneurons.

Results

Octuple recordings from neurons in the dentate gyrus.
To determine the functional connectivity rules between PNs and INs in the dentate gyrus, we performed simultaneous whole-cell recordings from up to eight neurons (up to seven GCs and up to four INs) in vitro (Fig. 1a, b). PV$^+$ interneurons, somatostatin-positive (SST$^+$), and cholecystokinin-positive (CCK$^+$) interneurons were identified in genetically modified mice, obtained by crossing Cre or Flp recombinase-expressing lines with tdTomato or EGFP reporter lines. PV$^+$ interneurons showed the characteristic fast-spiking AP phenotype during sustained current injection, whereas both SST$^+$ and CCK$^+$ interneurons generated APs with lower frequency, corroborating the reliability of the genetic labeling (Supplementary Figure 1).

To probe synaptic connectivity, we stimulated presynaptic neurons under current-clamp conditions, and recorded excitatory postsynaptic currents (EPSCs) or inhibitory postsynaptic currents (IPSCs) in postsynaptic neurons in the voltage-clamp

configuration (Fig. 1c–e, Fig. 2). In total, we tested 9098 possible connections in 50 octuples, 72 septuples, 68 sextuples, 48 quintuples, 17 quadruples, 10 triples, and 5 pairs in 270 slices. Interestingly, PV$^+$ interneurons showed a much higher connectivity than both SST$^+$ and CCK$^+$ interneurons. For GC–PV$^+$ interneuron pairs with intersomatic distance ≤ 100 μm, the mean connection probability was 11.0% for excitatory GC–PV$^+$ interneuron and 28.8% for inhibitory PV$^+$ interneuron–GC connectivity (Fig. 2g). In contrast, for both SST$^+$ interneurons and CCK$^+$ interneurons, the mean connection probability was substantially lower (1.4 and 2.8% for SST$^+$ interneurons, 1.2 and 12.1% for CCK$^+$ interneurons; Fig. 2g). Excitatory interactions between GCs were completely absent, and disynaptic inhibitory interactions between GCs[28,29] were extremely sparse (0.124%). These results indicate that in the dentate gyrus PV$^+$ interneurons show a markedly higher connectivity than SST$^+$ and CCK$^+$ interneurons, extending previous observations in the neocortex[30].

Connectivity rules for excitatory input of PV$^+$ interneurons.
As PV$^+$ interneurons showed the highest input and output connectivity, we focused our functional connectivity analysis on this interneuron subtype. We first examined the rules of excitatory synaptic connectivity between GCs and PV$^+$ interneurons by measuring EPSCs (Fig. 3a–c). We found that PV$^+$ interneurons were highly and locally connected to GCs. The connection probability showed a peak of 11.3%, and steeply declined as a function of intersomatic distance, with a space constant of 144 μm (Fig. 3b). In contrast, the EPSC peak amplitude showed no significant distance dependence (Fig. 3c). To determine the efficacy of unitary GC–PV$^+$ interneuron connections, we measured unitary excitatory postsynaptic potentials (EPSPs). Unitary EPSPs had a mean peak amplitude of 1.79 ± 0.36 mV (range: 0.30–7.16 mV; Supplementary Figure 2a, b)[28,31,32]. To assess the efficacy of these events in triggering spikes in the presence of ongoing synaptic activity from multiple sources, we performed in vivo whole-cell recordings from fast-spiking interneurons in the dentate gyrus in awake mice running on a linear treadmill (Supplementary Figure 2c–g). Under in vivo conditions, the difference between baseline membrane potential and threshold was 10.3 ± 1.8 mV (three in vivo recordings from fast-spiking interneurons in dentate gyrus). Thus, although the largest unitary EPSPs were close to the threshold of AP initiation, they were insufficient to trigger a spike. However, the high focal GC–PV$^+$ interneuron connectivity (Fig. 3b) may enable activation of PV$^+$ interneurons by spatial summation.

Connectivity rules for inhibitory output of PV$^+$ interneurons.
Next, we examined the rules of inhibitory synaptic connectivity between GCs and PV$^+$ interneurons by measuring IPSCs (Fig. 3d–f). Similar to excitatory GC–PV$^+$ interneuron connectivity, inhibitory PV$^+$ interneuron–GC connectivity was distance-dependent (Fig. 3e). However, maximal connection probability was higher (28.9%) and the range of connectivity was wider (215 μm) than that of excitation. Bootstrap analysis revealed that both maximal connectivity and space constant were significantly shorter for excitatory GC–PV$^+$ interneuron synapses than for inhibitory PV$^+$ interneuron–GC synapses ($P < 0.0001$ and $P = 0.0042$, respectively; Fig. 3g). Thus, different connectivity rules apply for excitatory and inhibitory GC –PV$^+$ interneuron connections (focal excitation versus broad inhibition).

To compare the connectivity rules in the dentate gyrus with those in other brain regions, we quantified the ratio of excitatory to inhibitory connection probability. We found that inhibition was much more abundant than excitation, with a connection probability ratio of 3.83, substantially higher than in other brain
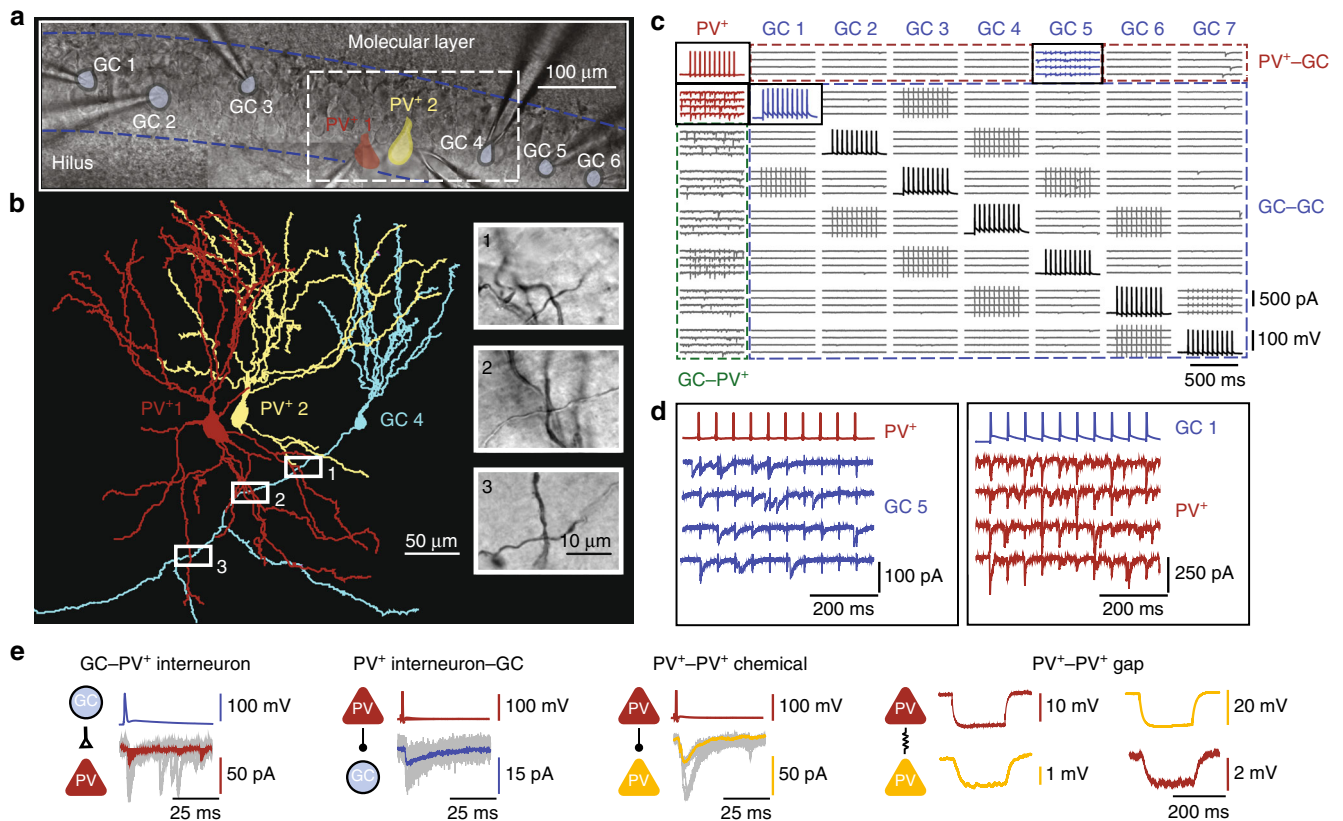
Fig. 1 Octuple recording from GCs and PV$^+$ interneurons in the dentate gyrus. **a** Octuple recording from five GCs and two PV$^+$ interneurons (seven cells successfully recorded). Infrared differential interference contrast video micrograph of the dentate gyrus in a 300-µm slice preparation, with eight recording pipettes. Shaded areas represent the 2D projections of cell bodies (blue, GCs; red and yellow, PV$^+$ interneurons). Blue dashed lines, boundaries of GC layer. **b** Partial reconstruction of one GC and two PV$^+$ interneurons in the same recording as shown in (**a**). Cells were filled with biocytin during recording and visualized using 3,3'-diaminobenzidine as chromogen. For clarity, only the somatodendritic domains were drawn for the PV$^+$ interneurons. Insets, biocytin-labeled putative synaptic contacts, corresponding to boxes in main figure. **c** Connectivity matrix of an octuple recording (all eight cells successfully recorded). Subpanels on the diagonal (AP traces) represent the presynaptic cells, subpanels outside the diagonal (EPSC or IPSC traces) indicate postsynaptic cells. In this example, 56 connections were tested; 7 excitatory GC–PV$^+$ interneuron connections, 7 inhibitory PV$^+$ interneuron-GC connections, and 42 connections between GCs. Brief transients in a subset of traces represent capacitive coupling artifacts, as shown in previous publications[5, 14]. **d** Expanded view of presynaptic APs and postsynaptic currents, corresponding to the boxed areas in (**c**). In this octuple recording, an inhibitory synaptic connection was identified between the PV$^+$ interneuron (red) and GC 5 (blue) and an excitatory synaptic connection was found between GC 1 (blue) and the PV$^+$ interneuron (red). The presence of a unidirectional excitatory GC–PV$^+$ interneuron connection and a unidirectional inhibitory PV$^+$ interneuron-GC connection documents the existence of lateral inhibition in this recording. **e** Coexistence of different synapses in an octuple recording. In this recording, an excitatory GC–PV$^+$ interneuron connection, an inhibitory PV$^+$ interneuron-GC connection, a chemical inhibitory connection between the PV$^+$ interneurons, and an electrical connection between the PV$^+$ interneurons were found (from left to right). Same recording as in (**a**) and (**b**)

areas (Supplementary Table 1). Furthermore, we quantified the abundance of lateral and recurrent motifs in pairs of neurons. In our total sample of 1301 GC–PV$^+$ interneuron pairs, we found 296 unidirectional inhibitory connections, but only 32 bidirectional connections (Fig. 3h). Thus, the ratio of lateral inhibition to recurrent inhibition was 9.25, substantially higher than in other circuits (Supplementary Table 1). These results indicate that connectivity rules of PV$^+$ interneurons in the dentate gyrus are unique in comparison to other previously examined circuits.

Connectivity rules for mutual inhibition of PV$^+$ interneurons. Finally, we analyzed the functional connectivity rules for synapses between interneurons (Fig. 4). Chemical inhibitory synapses between PV$^+$ interneurons showed a connectivity pattern that was more focal than that of inhibitory PV$^+$ interneuron-GC synapses (Fig. 4a, b). Likewise, electrical synapses between PV$^+$ interneurons[33–35] showed a focal connectivity pattern (Fig. 4c, d). Bootstrap analysis revealed that the maximal connectivity was significantly higher, while the space constant was significantly shorter

for inhibitory PV$^+$–PV$^+$ interneuron synapses than for PV$^+$ interneuron-GC synapses ($P = 0.0001$ and $P = 0.0036$, respectively). Furthermore, recordings from GCs and multiple PV$^+$ interneurons provided direct evidence for the suggestion[33] that EPSPs propagate through gap junctions, although the peak amplitude is markedly attenuated (Supplementary Figure 3). Taken together, these results indicate that connectivity rules in PN–IN microcircuits are synapse-specific. Different connectivity rules apply to excitatory and inhibitory synapses between PNs and INs (GC–PV$^+$ versus PV$^+$–GC), and to inhibitory synapses terminating on different postsynaptic target cells (PV$^+$–GC versus PV$^+$–PV$^+$ synapses).

Disynaptic connectivity motifs. Previous studies demonstrated that recurrent PN–PV$^+$ interneuron connectivity motifs are enriched above the chance level expected for a random network in several cortical microcircuits[3–7,36]. To test this hypothesis, we analyzed the abundance of all 25 possible disynaptic connectivity motifs in our sample (Fig. 5)[37]. To probe whether connectivity
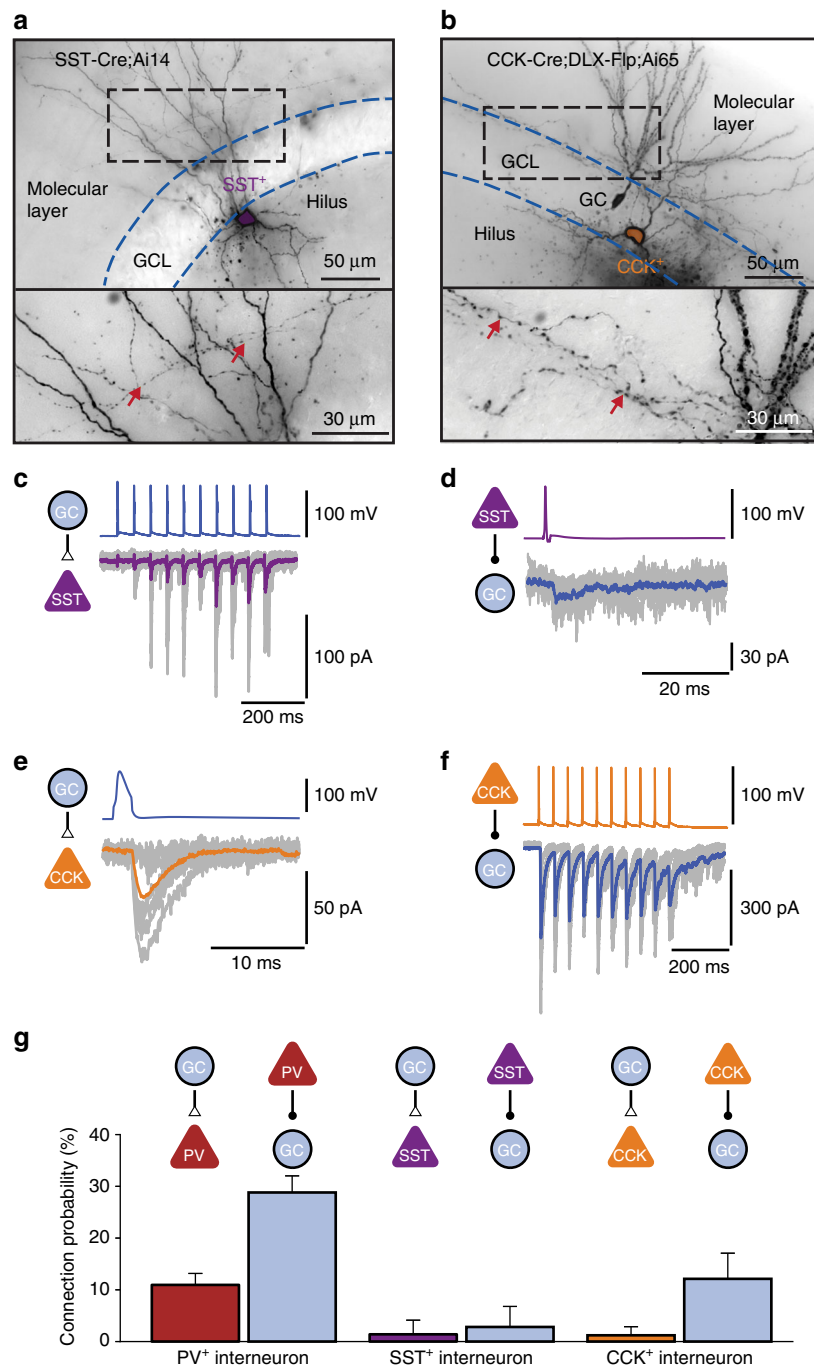
Fig. 2 Differential connectivity of PV[+], CCK[+], and SST[+] interneurons in the dentate gyrus. **a** Light micrograph of a SST[+] interneuron filled with biocytin during recording, and visualized using 3,3′-diaminobenzidine as chromogen. Cells were identified by genetic labeling in SST-Cre mice. Axon branches in the molecular layer (red arrows) suggest that the cell was a HIPP or TML interneuron[68, 69]. GCL, granule cell layer. **b** Light micrograph of a CCK[+] interneuron filled with biocytin. Cells were identified by genetic labeling in CCK-Cre;DLX 5/6-Flp mice. Axon branches in the inner molecular layer (red arrows) suggest that the cell was a HICAP interneuron[68-70]. **c, d** Excitatory and inhibitory connectivity of SST[+] interneurons. GC–SST[+] interneuron unitary EPSCs are shown in (**c**), SST[+] interneuron–GC IPSCs are illustrated in (**d**). Individual synaptic responses (gray) and average trace (magenta or blue, 15 traces) are shown overlaid. Note the facilitation of EPSCs during train stimulation in (**c**). **e, f** Excitatory and inhibitory connectivity of CCK[+] interneurons. GC–CCK[+] interneuron EPSCs are shown in (**e**), CCK[+] interneuron–GC IPSCs are illustrated in (**f**). Note the asynchronous release during and after train stimulation in (**f**), which is highly characteristic of CCK[+] interneuron output synapses[70]. **g** Comparison of average connection probability for pairs with an intersomatic distance of ≤100 μm. Whereas PV[+] interneurons were highly connected, SST[+] and CCK[+] interneurons showed a markedly lower excitatory and inhibitory connectivity (number of tested connections 767, 71, and 165). Error bars represent 95%-confidence intervals estimated from a binomial distribution
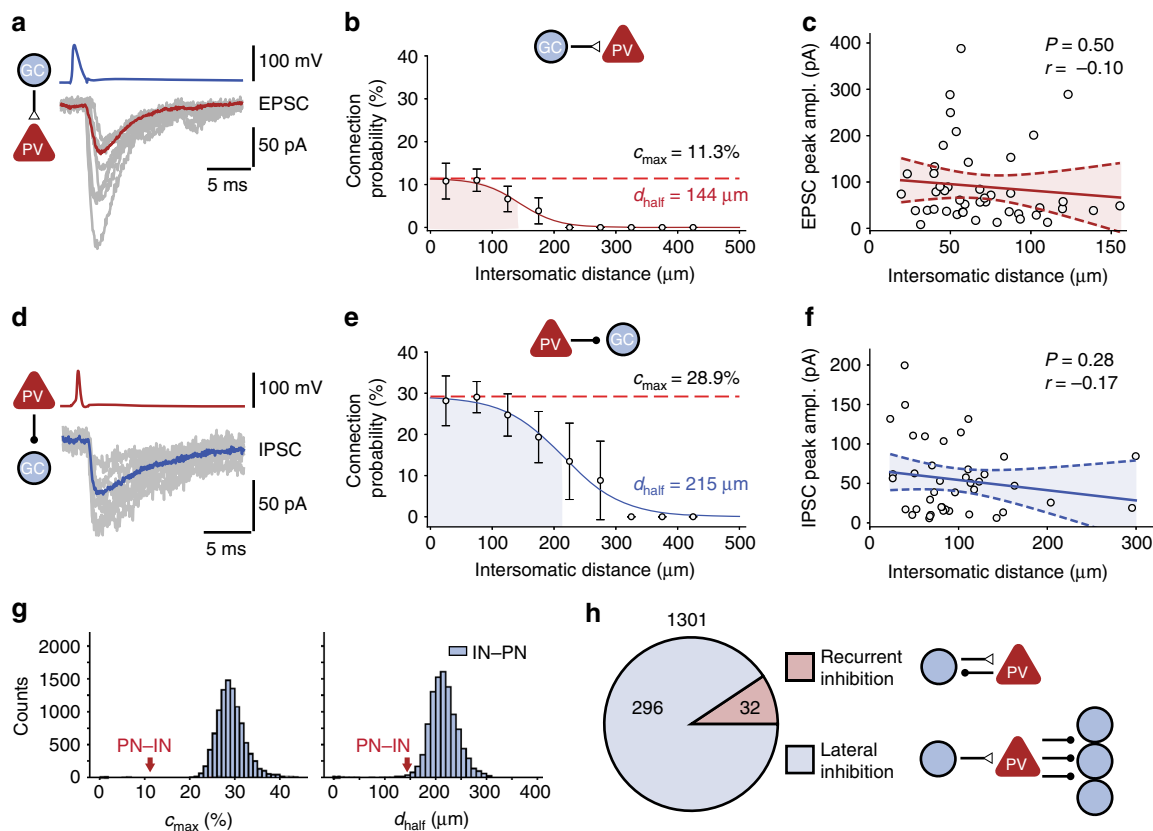
Fig. 3 Rules of excitatory and inhibitory connectivity in GC–PV+ interneuron networks. **a** Unitary EPSCs, with individual synaptic responses (gray) and average trace (red, 15 traces) in a representative GC–PV+ interneuron pair. **b** GC–PV+ interneuron connection probability plotted versus intersomatic distance. Connection probability was determined as the ratio of the number of found connections over that of all possible connections in a given distance range. Error bars represent 95%-confidence intervals estimated from a binomial distribution. Data points were fit with a sigmoidal function; shaded area indicates the distance range in which connection probability decayed to half-maximal value (space constant). Red dashed line, maximal connection probability. Maximal connection probability (c_{max}) was 11.3%, and space constant (d_{half}) was 144 μm. **c** Peak amplitude of unitary EPSCs at GC–PV+ interneuron synapses, plotted against intersomatic distance. Data points were fit by linear regression; dashed lines indicate 95%-confidence intervals. **d–f** Similar plots as shown in (**a–c**), but for IPSCs generated at inhibitory PV+ interneuron–GC synapses. Maximal connection probability was 28.9%, and space constant was 215 μm. **g** Bootstrap analysis of maximal connection probability and space constant. Histograms indicate distributions of c_{max} (left) and d_{half} (right) for 10,000 bootstrap replications of the inhibitory PV+ interneuron–GC connections. Red arrows indicate experimental mean values for GC–PV+ interneuron synapses. **h** Number of reciprocally coupled GC–PV+ interneuron pairs (excitatory and inhibitory synapse; "recurrent inhibition motif") and unidirectionally coupled PV+ interneuron–GC pairs (inhibitory synapse only; "lateral inhibition motif"). Note that the number of lateral inhibition motifs was almost 10-times higher than that of recurrent inhibition motifs, demonstrating the high abundance of lateral inhibition in the dentate gyrus microcircuit

was random[38] or nonrandom[14,39–42], we compared motif numbers in our experimental data to a simulated data set assuming random connectivity with experimentally determined distance-dependent connection probabilities (Fig. 5a, b).

Among the 25 possible disynaptic motifs, four types of motifs were significantly enriched above the chance level: (1) Gap junction connections between PV+ interneurons, (2) mutual inhibition motifs (PV+ interneuron–PV+ interneuron connections) combined with gap junction connections[43], (3) convergence motifs (connections of multiple GCs on a single PV+ interneuron), and (4) divergence motifs (connections of one PV+ interneuron onto multiple GCs; Fig. 5b; $P < 0.05$ after correction for multiple comparisons). Surprisingly, reciprocal GC–PV+ interneuron motifs were not significantly enriched.

Previous studies further demonstrated that the amplitude of unitary IPSCs is higher in bidirectionally than in unidirectionally connected PN–IN pairs[4,6]. In contrast, in the dentate gyrus neither the amplitude of EPSCs nor that of IPSCs was significantly different between bidirectionally and unidirectionally connected GC–PV+ interneuron pairs (Fig. 5c). However, the amplitude of IPSCs was significantly larger in PV+

interneuron–PV+ interneuron pairs coupled by reciprocal inhibitory synapses (Fig. 5d). Taken together, these results indicate that in the dentate gyrus, like in other cortical areas, synaptic connectivity of PV+ interneurons is nonrandom. However, both the types of enriched motifs and the rules setting synaptic strength differ from those in other circuits[3,4].

Discussion

Our results demonstrate that the rules of functional connectivity in the PN–IN network of the dentate gyrus fundamentally differ from those in other cortical circuits. In the dentate gyrus, unidirectionally inhibitory connections are ~10-times more frequent than reciprocal connections, demonstrating a massive prevalence of lateral inhibition in this circuit (Supplementary Table 1). In contrast, in neocortex, entorhinal cortex, and presubiculum, reciprocal connections are equally or more abundant than unidirectional connections, implying powerful recurrent inhibition[3–7] (Supplementary Table 1). Furthermore, in the dentate gyrus mutual inhibition motifs, convergence motifs, and divergence motifs are statistically overrepresented. In contrast, in the
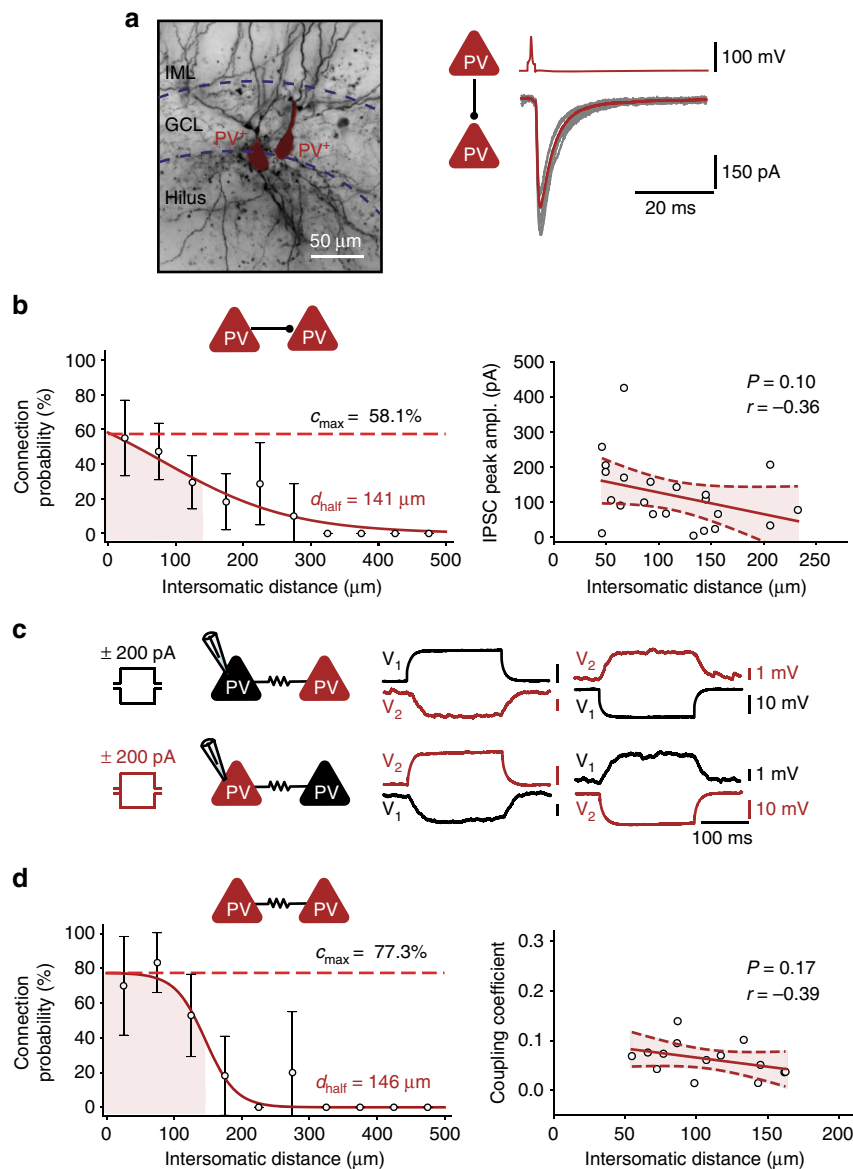
Fig. 4 Rules of chemical and electrical connectivity between PV+ interneurons. **a** Left, light micrograph of a biocytin-labeled PV+ interneuron–PV+ interneuron pair. Right, unitary IPSCs, with individual synaptic responses (gray) and average trace (red, 15 traces) in the same pair. GCL, granule cell layer; IML, inner molecular layer. **b** PV+ interneuron–PV+ interneuron chemical connection probability (left) and IPSC peak amplitude (right) plotted versus intersomatic distance. Connection probability data points were fit with a sigmoidal function, IPSC amplitude data were analyzed by linear regression. Maximal connection probability was 58.1%, and space constant was 141 μm. **c** Electrical coupling between two PV+ interneurons. Voltage changes in the pre- and postsynaptic cell caused by the injections of long polarizing current pulses (left, + 200 pA; right, −200 pA; 200 ms) in one of the coupled cells. **d** PV+ interneuron–PV+ interneuron electrical connection probability (left) and coupling coefficient (right) plotted versus intersomatic distance. Maximal connection probability was 77.3%, and space constant was 146 μm. The coupling coefficient (CC) was calculated as the mean ratio of steady-state voltages (V_2/V_1, V_1/V_2) during application of current pulses in one of the cells (cell 1 and cell 2, respectively)

neocortex, interneuron connectivity has been suggested to be largely random[2]. Collectively, these results suggest that the dentate gyrus network obeys unique connectivity rules.

The specific connectivity rules of the dentate circuit raise the intriguing possibility that these rules represent an adaptation to specific network functions implemented in this brain region. A major function of the dentate gyrus is pattern separation[8–12], thought to be generated by a "winner-takes-all" mechanism[15–19]. In an ideal pattern separation circuit, a small population of activated "winner cells" must be able to efficiently and rapidly inhibit a large population of "non-winner cells". The dentate gyrus connectivity rules are well suited for these functions. First, powerful lateral inhibition efficiently suppresses non-winners,

whereas winners remain unaffected. Second, the combination of local connectivity and rapid axonal signaling mechanisms of PV+ interneurons[1,44] implements a high-speed suppression mechanism, as required for efficient pattern separation. Previous modeling work suggested that scale-free network organization and the presence of hub neurons may enhance the robustness of network computations[45,46]. Our results may support this view, since the high abundance convergence and divergence motifs are consistent with scale-free architectural properties.

Furthermore, the connectivity rules of the PN–IN network may be important for the generation of network oscillations in dentate gyrus[47]. In particular, the high chemical and electrical IN–IN connectivity establishes an efficient gamma oscillator circuit. The
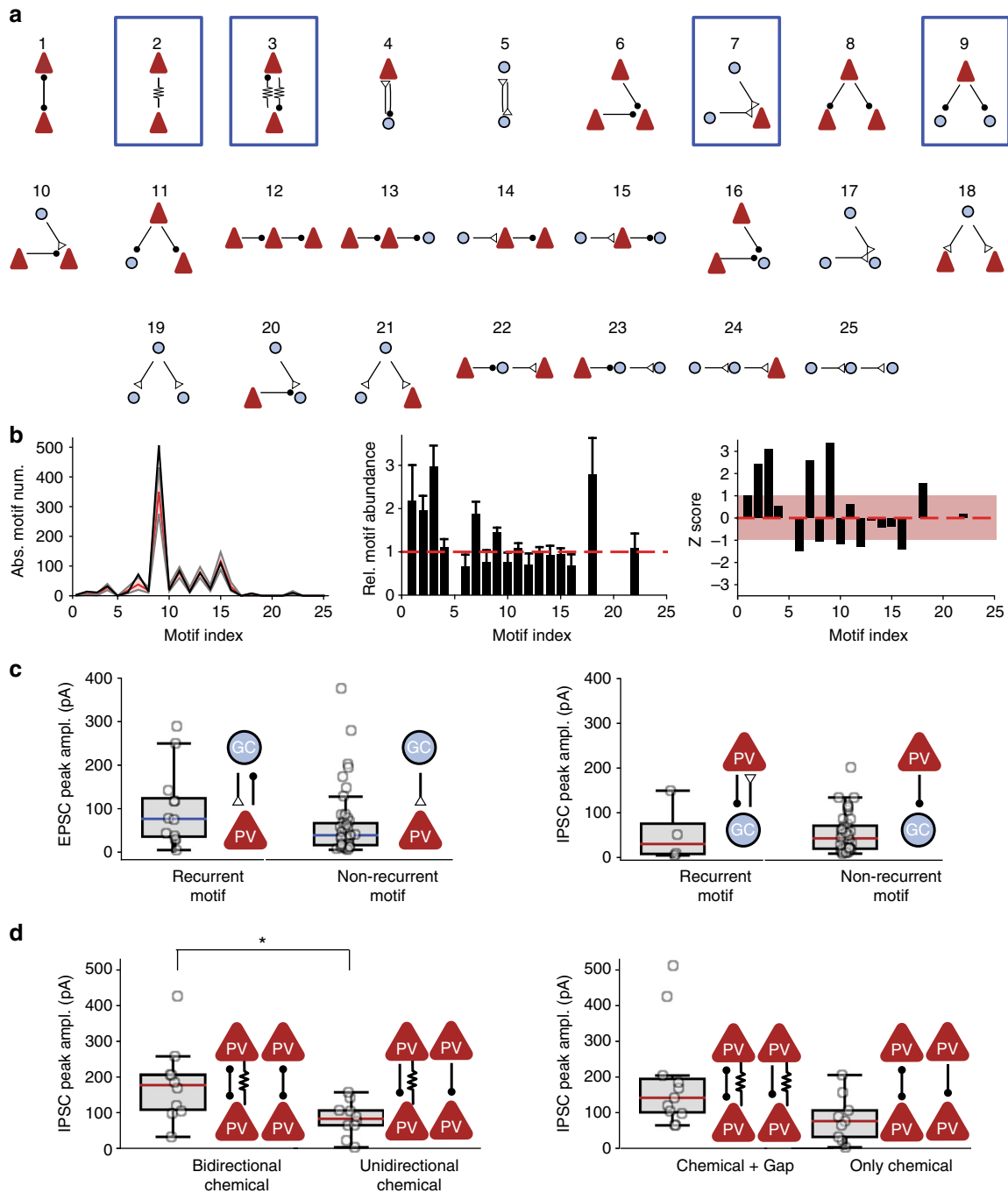
Fig. 5 Overabundance of disynaptic connectivity motifs in GC–PV+ interneuron networks and different functional properties of synapses embedded in motifs. **a** Graph analysis of disynaptic connectivity motifs. In total, there are five possible disynaptic connectivity motifs with two cells and 20 disynaptic motifs involving three cells. Arrows with open triangles indicate excitatory synapses, arrows with filled circles represent inhibitory synapses, and arrows with zigzag lines indicate gap junctions. Number indicates motif index. **b** Analysis of the number of motifs in 10,000 simulated data sets. Connection probability for the simulated data set was specified according to the experimentally determined spatial rules. Left, absolute motif number in experimental (black) and simulated data set (red, median; gray, 90%-confidence interval). Center, bar plot of relative abundance of various motifs (number of motifs in experimental data set over mean number in simulated data set). Error bars were taken from bootstrap analysis. Right, bar plot of z score of the different motifs. Light red area indicates z score in the interval [−1, 1]. Motifs 2, 3, 7, and 9 were significantly enriched above the chance level ($P = 0.03145$, 0.0085, 0.0272, and 0.0068 after multiple comparison correction). In contrast, motifs 6, 8, 10, 12, and 16 were slightly, but not significantly underrepresented ($P = 0.15$ for motif 6). Note that motifs 5, 17, 19–21, and 23–25 were not encountered in the present data set, because of the lack of connectivity between GCs. **c** Comparison of EPSC peak amplitude (left) and IPSC peak amplitude (right) in bidirectionally versus unidirectionally coupled GC–PV+ interneuron pairs. Peak amplitudes were not significantly different ($P = 0.33$ and 0.58, respectively). **d** Comparison of IPSC peak amplitude in PV+ interneuron–PV+ interneuron pairs connected by different chemical or electrical synapse motifs. IPSC peak amplitude was significantly larger in pairs with bidirectional inhibitory connections than with unidirectional connections ($P = 0.016$) and slightly higher in connections with than without gap junctions ($P = 0.057$). Asterisk indicates $P < 0.05$

dense and focal electrical–chemical connectivity may explain the high power and frequency of gamma oscillations in the dentate gyrus[47–49]. Previous modeling work suggested that the small-world interneuron network architecture will support the emergence of coherent gamma oscillations[50,51]. Our results support this notion, since the high abundance of electrical–chemical IN–IN motifs would be consistent with small-world architectural properties[52]. The establishment of a robust gamma oscillation circuit may, conversely, be important for the pattern separation process. Proposed models of pattern separation imply that the separation of patterns takes place in the time period during the recovery from a preceding gamma cycle[17]. Whether and how the pattern separation computation and the generation of gamma oscillations can coexist in the same circuit remains to be determined.

Our results suggest the possibility that the uniquely high abundance of lateral inhibition in dentate gyrus may contribute to pattern separation (Supplementary Table 1). What then is the function of recurrent inhibition in all other brain areas, such as the neocortical circuits? In the neocortex, PN activity is high, which requires a mechanism to establish excitation–inhibition balance; reciprocal PN–IN connectivity seems well suited for this purpose[7,20]. In contrast, in the dentate gyrus PN activity is low, and such a balancing function may not be required[53–57]. Additionally, reciprocal PN–IN connectivity could contribute to the generation of slower network oscillations in these brain regions, for example in the lower gamma or beta frequency range, which are characteristic for the neocortex.

Our results are consistent with the idea that local connectivity rules can shape diverse network computations across multiple circuits. In the dentate gyrus, the unique PN–IN connectivity rules may determine the properties of pattern separation, grid-to-place code conversion, or processing of context information[17,58]. In the neocortex, PN–IN connectivity may determine network stability and excitation–inhibition balance[7,20]. In the hippocampal CA3 network, functional PN–PN connectivity rules shape pattern completion[14], whereas in the neocortex functional PN–PN connectivity may shape response properties such as orientation selectivity[41]. Thus, the present results contribute to the emerging view that local connectivity rules are major determinants of higher computations in neuronal networks. Future work will be needed to test this hypothesis in both network models and behavioral experiments.

Methods

Hippocampal slice preparation. Experiments on genetically modified mice were performed in strict accordance with institutional, national, and European guidelines for animal experimentation and were approved by the Bundesministerium für Wissenschaft, Forschung und Wirtschaft of Austria (A. Haslinger, Vienna; BMWFW-66.018/0007-WF/II/3b/2014; BMWF-66.018/0010-WF/V/3b/2015; BMWFW-66.018/0020-WF/V/3b/2016).

To genetically label PV+ interneurons, C57BL/6 J PV-Cre knockin mice (http://jaxmice.jax.org/strain/008069) crossed with Ai14 loxP-flanked red fluorescent protein tdTomato reporter mice (https://www.jax.org/strain/007914) were used. To identify SST+ interneurons, somatostatin-ires-Cre mice (C-SSTtm1Npa; kindly provided by H. van der Putten; Novartis Pharma; MTD37295, Basel, Switzerland) were crossed with Ai14 tdTomato reporter mice. Finally, to label CCK+ interneurons, CCK-ires-Cre;DLX 5/6-Flp mice (https://www.jax.org/strain/012706 and https://www.jax.org/strain/010815) were crossed with dual reporter mice expressing either EGFP or tdTomato (RCE = R26R CAG boosted EGFP mice, https://www.jax.org/strain/010812; Ai65, https://www.jax.org/strain/021875)[59]. Mice (20- to 44-days-old; mostly postnatal day 20–25) of either sex were lightly anesthetized with isoflurane (Forane, AbbVie, Vienna). For animals up to postnatal day 30, mice were sacrificed by decapitation. For animals older than 30 days, transcardial perfusion was performed with ice-cold sucrose-artificial cerebrospinal fluid (sucrose-ACSF) solution. Animals were deeply anesthetized with isoflurane followed by the intraperitoneal injection of a mixture of xylazine (0.5 ml, 2%), ketamine (1 ml, 10%), acepromazine (0.3 ml, 1.4%), and physiological NaCl solution (1.5 ml, 0.9%). Anesthetics were applied at a dose of 0.033 ml/10 g body

weight. The depth of the anesthesia was verified by the absence of toe pinch reflexes.

For preparing slices, the brain was rapidly removed and immersed in ice-cold sucrose-ACSF solution during dissection. A block of tissue containing the hippocampus was transferred to a vibratome (VT 1200, Leica) and transverse slices of 300-μm thickness were cut with blade oscillation amplitude of 1.25 mm and blade forward movement velocity of 0.03 mm s^{-1}[60]. Finally, slices were incubated at ~35 °C in standard artificial cerebrospinal fluid (ACSF) for 30 minutes and subsequently maintained at ~22 °C for maximally 5 h before transfer into the recording chamber.

Solutions and chemicals. The ACSF used for in vitro recordings contained 125 mM NaCl, 25 mM NaHCO$_3$, 25 mM glucose, 2.5 mM KCl, 1.25 mM NaH$_2$PO$_4$, 2 mM CaCl$_2$, and 1 mM MgCl$_2$. The sucrose-ACSF used for dissection contained 64 mM NaCl, 25 mM NaHCO$_3$, 10 mM glucose, 120 mM sucrose, 2.5 mM KCl, 1.25 mM NaH$_2$PO$_4$, 0.5 mM CaCl$_2$, and 7 mM MgCl$_2$. The osmolarity of the solutions was 290–310 mOsm and the pH was maintained at ~7.3 when equilibrated with a 95% O$_2$/5% CO$_2$ gas mixture. The intracelluar solution for in vitro recordings contained 120 mM K-gluconate, 40 mM KCl, 2 mM MgCl$_2$, 2 mM Na$_2$ATP, 10 mM HEPES, 0.1 mM EGTA, and 0.3% biocytin, pH adjusted to 7.28 with KOH. Chemicals were purchased from Merck or Sigma-Aldrich.

Multi-cell recordings. Glass micropipettes were fabricated from thick-walled borosilicate tubing (2 mm outer diameter, 1 mm inner diameter) and had open-tip resistances of 3–8 MΩ. They were manually positioned with eight LN mini 25 micromanipulators (Luigs and Neumann) under visual control[14] provided by a modified Olympus BX51 microscope equipped with a 60x water-immersion objective (LUMPlan FI/IR, NA = 0.90, Olympus, 2.05 mm working distance) and infrared differential interference contrast video microscopy and epifluorescence. To preserve connectivity, cell bodies ~30–120 μm below the surface of the slice were targeted for recording. Interneurons were identified on the basis of tdTomato or EGFP fluorescence in epifluorescence illumination and the AP phenotype upon 1-s current pulses (>50 Hz in a series of pulses of 100–1,200 pA for PV+ interneurons). Mature GCs were identified on the basis of morphological appearance in the infrared image and on the basis of passive and active membrane properties. Cells with input resistance > 500 MΩ, potentially representing newborn GCs[61], were not included in the analysis. Cells with resting potentials more positive than −55 mV were immediately discarded. In total, the number of successfully recorded cells per recording varied between eight and two. Recording temperature was ~22 °C (range: 20–24 °C, room temperature).

Electrical signals were acquired with four two-channel Multiclamp 700B amplifiers (Molecular Devices), low-pass filtered at 6–10 kHz, and digitized at 20 kHz with a Cambridge Electronic Design 1401 mkII AD/DA converter using custom-made stimulation-acquisition scripts running under Signal 6.0 software (CED). For current-clamp recordings, pipette capacitance was ~80% compensated and series resistance was balanced by the bridge circuit of the amplifier; settings were readjusted throughout the experiment when necessary. For voltage-clamp recordings, series resistance was not compensated, but repeatedly monitored using 2-mV hyperpolarizing pulses.

To test for synaptic connections, a presynaptic neuron was stimulated with a train of five or ten current pulses (2 ms, 1–2 nA) at frequencies of 20 or 50 Hz, while all other neurons were voltage-clamped at −70 mV (Fig. 1c). A connection was defined as monosynaptic if synaptic currents had latencies ≤ 4.0 ms and peak amplitudes were larger than 2.5 times the standard deviation of the baseline of the average trace (computed from 15–30 individual traces). Events with latencies > 4.0 ms were considered polysynaptic. For distal SST+–GC synapses, connectivity may be underestimated, because of substantial attenuation of synaptic signals by cable filtering.

Data analysis. Recordings were analyzed using Stimfit and Python-based scripts[62]. Synaptic latency was measured from the peak of the presynaptic AP to the onset of the postsynaptic potential or current. Kinetic analysis of EPSCs or IPSCs was performed in pairs with series resistance of < 15 MΩ. Distance was measured from soma center to soma center. Analysis of the axonal arbor of PV+ interneurons and GCs revealed that the axonal length was 2.21 ± 0.20 and 1.59 ± 0.07 times larger than the corresponding intersomatic distance (Supplementary Figure 4). Connection probability was calculated as number of connected pairs over total number of tested pairs in each 50-μm distance interval. 95%-confidence intervals were obtained according to binomial distributions. Distance dependence of connectivity was fit with a sigmoidal function $f(x) = A [1 + Exp[(x – B)/C]^{-1}$, where x is absolute distance, and A, B, and C are fitted parameters. Throughout the text, the maximal connection probability (c_{max}) was determined as $f(0)$, and the space constant (d_{half}) was determined as the x' value that specified the condition $f(x')/f(0)$ = 0.5. To test whether connectivity differed between synapses, 10,000 bootstrap replications of the inhibitory PV+ interneuron–GC data set were obtained, and the mean values of the GC–PV+ interneuron and PV+ interneuron–PV+ interneuron experimental data sets were compared against the simulated distribution[63]. Values are given as mean ± standard error of the mean (S.E.M.). Box plots show lower quartile (Q1), median (horizontal line), and upper quartile (Q3). The interquartile range (IQR = Q3–Q1) is represented as the height of the box. Whiskers extend to

the most extreme data point that is no more than 1.5 x IQR from the edge of the box (Tukey style). Statistical comparisons were done either with a non-parametric Mann–Whitney U two-sided test or by linear regression, testing whether the slope was significantly different from 0.

To test whether disynaptic motifs[64] occurred significantly more frequently than expected by chance, we simulated the entire set of recording configurations including PV$^+$ interneurons (41 octuples, 62 septuples, 54 sextuples, 37 quintuples, 14 quadruples, 7 triples, and 3 pairs in 218 slices) 10,000 times, assuming random connectivity[14,38,64]. The connection probabilities were set to the experimentally determined distance-dependent values. For each simulated data set, we counted the number of all 25 possible disynaptic motifs (Fig. 5a). From the 10,000 bootstrap replications, mean, median, and confidence intervals for these counts were determined. P values were calculated as the number of replications in which the motif number was equal to or larger than the empirical number, divided by the number of replications. If a motif was never encountered in the 10,000 replications, P was assumed as < 0.0001. For assessing statistical significance, correction for multiple testing was performed using a Benjamini–Hochberg method that controls the false discovery rate[65]. P values for m comparisons were sorted in increasing order ($P_1 \leq P_2 \leq \ldots \leq P_m$), the first P_i value that satisfied the condition $P_i \leq i$ / m 0.05 was identified (starting with P_m), and the motifs corresponding to P_j values with $1 \leq j \leq i$ were considered significant. For illustration purposes, P values were converted into z scores, using the quantiles of a standard normal distribution.

Morphological analysis. Neurons that were filled with biocytin (0.3%) for >1 h were processed for morphological analysis. After withdrawal of the pipettes, resulting in the formation of outside-out patches at the pipette tips, slices were fixed for 12–24 h at 4 °C in a 0.1 M phosphate buffer (PB) solution containing 2.5% paraformaldehyde, 1.25% glutaraldehyde, and 15% (v/v) saturated picric acid solution. After fixation, slices were treated with hydrogen peroxide (1%, 10 min) to block endogenous peroxidases, and rinsed in PB several times. Membranes were permeabilized with 1% Triton X100 in PB for 1 h. Slices were then transferred to a PB solution containing 1% avidin-biotinylated horseradish peroxidase complex (ABC, Vector Laboratories) and 1% Triton X100 for ~ 12 h. Excess ABC was removed by several rinses in PB and the slices were developed with 0.05% 3,3′-diaminobenzidine tetrahydrochloride (DAB) and subsequently hydrogen peroxide. Finally, slices were embedded in Mowiol (Sigma-Aldrich).

In vivo recordings from dentate gyrus PV$^+$ interneurons. Whole-cell patch-clamp recordings in vivo were performed in male 35- to 63-day-old mice as described previously[53]. Animals were in the head-fixed, fully awake configuration, and were running on a linear belt treadmill[66,67]. The head-bar implantation and craniotomy were performed under anesthesia by intraperitoneal injection of 80 mg/kg ketamine (Intervet) and 8 mg/kg xylazine (Graeub), followed by local anesthesia with lidocaine. A custom-made steel head-bar was attached to the skull using superglue and dental cement. The day before recording, two small (~0.5 mm in diameter) craniotomies, one for the patch electrode and one for a local field potential (LFP) electrode, were drilled at the following coordinates: 2.0 mm caudal, 1.2 mm lateral for whole-cell recording; 2.5 mm caudal, 1.2 mm lateral for the LFP recording. The dura was left intact, and craniotomies were covered with silicone elastomer (Kwik-Cast, World Precision Instruments). Pipettes were fabricated from borosilicate glass capillaries (1.75 mm outer diameter, 1.25 mm inner diameter). Long-taper whole-cell patch electrodes (9–12 MΩ) were filled with a solution containing: 130 mM K-gluconate, 2 mM KCl, 2 mM MgCl$_2$, 2 mM Na$_2$ATP, 0.3 mM NaGTP, 10 mM HEPES, 18 mM sucrose, 10 or 0.1 mM EGTA, and 0.3% biocytin, pH adjusted to 7.28 with KOH. Whole-cell patch electrodes were advanced through the cortex with 500–600 mbar of pressure to prevent the electrode tip from clogging. After passing the hippocampus CA1 subfield, the pressure was reduced to 20 mbar. After the blind whole-cell recording was obtained, series resistance was calculated by applying a test pulse (+ 50 mV and −10 mV) under voltage-clamp conditions. Recordings were immediately discarded if series resistance exceeded 100 MΩ. After the bridge balance was compensated, step currents from −100 pA to 400 pA were injected to calculate input resistance and maximal firing frequency of the recorded cells. All the recordings were done in current-clamp experiment configuration without holding current injection using a Heka EPC double amplifier. Signals were low-pass filtered at 10 kHz (Bessel) and sampled at 25 kHz with Heka Patchmaster acquisition software. After recording, the patch pipettes were slowly withdrawn to form an outside-out patch, verifying the integrity of the seal. Data included were obtained from three fast-spiking cells in the dentate gyrus, which generated APs during sustained current injection at a frequency of >100 Hz. To determine the relative AP threshold, spontaneous action potentials (sAPs) were detected, using either a single sAP or the first AP in a burst. The membrane potential preceding the sAP was measured in a 10–20 ms time window before the sAP. sAP absolute threshold was determined from a dV/dt–V phase plot; the rising phase was fit with an exponential function including a shift factor, and the intersection of the fit curve with the baseline was defined as threshold.

References

1. Hu, H., Gan, J. & Jonas, P. Interneurons. Fast-spiking, parvalbumin$^+$ GABAergic interneurons: from cellular design to microcircuit function. *Science* **345**, 1255263 (2014).
2. Packer, A. M. & Yuste, R. Dense, unspecific connectivity of neocortical parvalbumin-positive interneurons: a canonical microcircuit for inhibition? *J. Neurosci.* **31**, 13260–13271 (2011).
3. Holmgren, C., Harkany, T., Svennenfors, B. & Zilberter, Y. Pyramidal cell communication within local networks in layer 2/3 of rat neocortex. *J. Physiol.* **551**, 139–153 (2003).
4. Yoshimura, Y. & Callaway, E. M. Fine-scale specificity of cortical networks depends on inhibitory cell type and connectivity. *Nat. Neurosci.* **8**, 1552–1559 (2005).
5. Couey, J. J. et al. Recurrent inhibitory circuitry as a mechanism for grid formation. *Nat. Neurosci.* **16**, 318–324 (2013).
6. Peng, Y., Barreda Tomás, F. J., Klisch, C., Vida, I. & Geiger, J. R. P. Layer-specific organization of local excitatory and inhibitory synaptic connectivity in the rat presubiculum. *Cereb. Cortex* **27**, 2435–2452 (2017).
7. Znamenskiy, P., et al Functional selectivity and specific connectivity of inhibitory neurons in primary visual cortex. //www.biorxiv.org/, https://doi.org/10.1101/294835 (2018).
8. Leutgeb, J. K., Leutgeb, S., Moser, M. B. & Moser, E. I. Pattern separation in the dentate gyrus and CA3 of the hippocampus. *Science* **315**, 961–966 (2007).
9. Rolls, E. T. Pattern separation, completion, and categorisation in the hippocampus and neocortex. *Neurobiol. Learn. Mem.* **129**, 4–28 (2016).
10. Cayco-Gajic, N. A., Clopath, C. & Silver, R. A. Sparse synaptic connectivity is required for decorrelation and pattern separation in feedforward networks. *Nat. Commun.* **8**, 1116 (2017).
11. Chavlis, S. & Poirazi, P. Pattern separation in the hippocampus through the eyes of computational modeling. *Synapse* **71**, e21972 (2017).
12. Leal, S. L. & Yassa, M. A. Integrating new findings and examining clinical applications of pattern separation. *Nat. Neurosci.* **21**, 163–173 (2018).
13. Bischofberger, J., Engel, D., Frotscher, M. & Jonas, P. Timing and efficacy of transmitter release at mossy fiber synapses in the hippocampal network. *Pflügers Arch.* **453**, 361–372 (2006).
14. Guzman, S. J., Schlögl, A., Frotscher, M. & Jonas, P. Synaptic mechanisms of pattern completion in the hippocampal CA3 network. *Science* **353**, 1117–1123 (2016).
15. Majani, E., Erlarson, R. & Abu-Mostafa, Y. On the k-winners takes-all network. *Adv. Neural Inf. Process Syst.* **1**, 634–642 (1988).
16. Maass, W. On the computational power of winner-take-all. *Neural Comput.* **12**, 2519–2535 (2000).
17. de Almeida, L., Idiart, M. & Lisman, J. E. A second function of gamma frequency oscillations: an E%-max winner-take-all mechanism selects which cells fire. *J. Neurosci.* **29**, 7497–7503 (2009).
18. Tetzlaff, T., Helias., M., Einevoll, G. T. & Diesmann, M. Decorrelation of neural-network activity by inhibitory feedback. *PLoS. Comput. Biol.* **8**, e1002596 (2012).
19. Faghihi, F. & Moustafa, A. A. A computational model of pattern separation efficiency in the dentate gyrus with implications in schizophrenia. *Front. Syst. Neurosci.* **9**, 42 (2015).
20. Wiechert, M. T., Judkewitz, B., Riecke, H. & Friedrich, R. W. Mechanisms of pattern decorrelation by recurrent neuronal circuits. *Nat. Neurosci.* **13**, 1003–1010 (2010).
21. Lin, A. C., Bygrave, A. M., de Calignon, A., Lee, T. & Miesenböck, G. Sparse, decorrelated odor coding in the mushroom body enhances learned odor discrimination. *Nat. Neurosci.* **17**, 559–568 (2014).
22. Gschwend, O. et al. Neuronal pattern separation in the olfactory bulb improves odor discrimination learning. *Nat. Neurosci.* **18**, 1474–1482 (2015).
23. Engin, E. et al. Tonic inhibitory control of dentate gyrus granule cells by α5-containing GABAA receptors reduces memory interference. *J. Neurosci.* **35**, 13698–13712 (2015).
24. Temprana, S. G. et al. Delayed coupling to feedback inhibition during a critical period for the integration of adult-born granule cells. *Neuron* **85**, 116–130 (2015).
25. Andersen, P., Eccles, J. C. & Løyning, Y. Recurrent inhibition in the hippocampus with identification of the inhibitory cell and its synapses. *Nature* **198**, 540–542 (1963).

26. Jonas, P. & Buzsáki, G. Neural inhibition. *Scholarpedia* **2**, 3286 (2007).

27. Chow, S. F., Wick, S. D. & Riecke, H. Neurogenesis drives stimulus decorrelation in a model of the olfactory bulb. *PLoS. Comput. Biol.* **8**, e1002398 (2012).

28. Miles, R. Synaptic excitation of inhibitory cells by single CA3 hippocampal pyramidal cells of the guinea-pig in vitro. *J. Physiol.* **428**, 61–77 (1990).

29. Jouhanneau, J. S., Kremkow, J. & Poulet, J. F. A. Single synaptic inputs drive high-precision action potentials in parvalbumin expressing GABA-ergic cortical neurons in vivo. *Nat. Commun.* **9**, 1540 (2018).

30. Pala, A. & Petersen, C. C. H. In vivo measurement of cell-type-specific synaptic connectivity and synaptic transmission in layer 2/3 mouse barrel cortex. *Neuron* **85**, 68–75 (2015).

31. Scharfman, H. E., Kunkel, D. D. & Schwartzkroin, P. A. Synaptic connections of dentate granule cells and hilar neurons: results of paired intracellular recordings and intracellular horseradish peroxidase injections. *Neuroscience* **37**, 693–707 (1990).

32. Geiger, J. R. P., Lübke, J., Roth, A., Frotscher, M. & Jonas, P. Submillisecond AMPA receptor-mediated signaling at a principal neuron-interneuron synapse. *Neuron* **18**, 1009–1023 (1997).

33. Galarreta, M. & Hestrin, S. A network of fast-spiking cells in the neocortex connected by electrical synapses. *Nature* **402**, 72–75 (1999).

34. Bartos, M., Vida, I., Frotscher, M., Geiger, J. R. P. & Jonas, P. Rapid signaling at inhibitory synapses in a dentate gyrus interneuron network. *J. Neurosci.* **21**, 2687–2698 (2001).

35. Galarreta, M. & Hestrin, S. Spike transmission and synchrony detection in networks of GABAergic interneurons. *Science* **292**, 2295–2299 (2001).

36. Larimer, P. & Strowbridge, B. W. Nonrandom local circuits in the dentate gyrus. *J. Neurosci.* **28**, 12212–12223 (2008).

37. Schröter, M., Paulsen, O. & Bullmore, E. T. Micro-connectomics: probing the organization of neuronal networks at the cellular scale. *Nat. Rev. Neurosci.* **18**, 131–146 (2017).

38. Erdös, P. & Rényi, A. On random graphs. I. *Publ. Math.* **6**, 290–297 (1959).

39. Song, S., Sjöström, P. J., Reigl, M., Nelson, S. & Chklovskii, D. B. Highly nonrandom features of synaptic connectivity in local cortical circuits. *PLoS Biol.* **3**, e68 (2005).

40. Perin, R., Berger, T. K. & Markram, H. A synaptic organizing principle for cortical neuronal groups. *Proc. Natl Acad. Sci. USA* **108**, 5419–5424 (2011).

41. Cossell, L. et al. Functional organization of excitatory synaptic strength in primary visual cortex. *Nature* **518**, 399–403 (2015).

42. Jouhanneau, J. S., Kremkow, J., Dorrn, A. L. & Poulet, J. F. In vivo monosynaptic excitatory transmission between layer 2 cortical pyramidal neurons. *Cell Rep.* **13**, 2098–2106 (2015).

43. Rieubland, S., Roth, A. & Häusser, M. Structured connectivity in cerebellar inhibitory networks. *Neuron* **81**, 913–929 (2014).

44. Hu, H. & Jonas, P. A supercritical density of Na$^+$ channels ensures fast signaling in GABAergic interneuron axons. *Nat. Neurosci.* **17**, 686–693 (2014).

45. Barabasi, A. L. & Albert, R. Emergence of scaling in random networks. *Science* **286**, 509–512 (1999).

46. Albert, R., Jeong, H. & Barabasi, A. L. Error and attack tolerance of complex networks. *Nature* **406**, 378–382 (2000).

47. Bartos, M., Vida, I. & Jonas, P. Synaptic mechanisms of synchronized gamma oscillations in inhibitory interneuron networks. *Nat. Rev. Neurosci.* **8**, 45–56 (2007).

48. Bragin, A. et al. Gamma (40–100 Hz) oscillation in the hippocampus of the behaving rat. *J. Neurosci.* **15**, 47–60 (1995).

49. Strüber, M., Sauer, J. F., Jonas, P. & Bartos, M. Distance-dependent inhibition facilitates focality of gamma oscillations in the dentate gyrus. *Nat. Commun.* **8**, 758 (2017).

50. Buzsáki, G., Geisler, C., Henze, D. A. & Wang, X. J. Interneuron diversity series: circuit complexity and axon wiring economy of cortical interneurons. *Trends Neurosci.* **27**, 186–193 (2004).

51. Watts, D. J. & Strogatz, S. H. Collective dynamics of 'small-world' networks. *Nature* **393**, 440–442 (1998).

52. Song, H. F. & Wang, X.-J. Simple, distance-dependent formulation of the Watts-Strogatz model for directed and undirected small-world networks. *Phys. Rev. E* **90**, 062801 (2014).

53. Pernía-Andrade, A. J. & Jonas, P. Theta-gamma-modulated synaptic currents in hippocampal granule cells in vivo define a mechanism for network oscillations. *Neuron* **81**, 140–152 (2014).

54. Pilz, G. A. et al. Functional imaging of dentate granule cells in the adult mouse hippocampus. *J. Neurosci.* **36**, 7407–7414 (2016).

55. Danielson, N. B. et al. In vivo imaging of dentate gyrus mossy cells in behaving mice. *Neuron* **93**, 552–559 (2017).

56. GoodSmith, D. et al. Spatial representations of granule cells and mossy cells of the dentate gyrus. *Neuron* **93**, 677–690 (2017).

57. Senzai, Y. & Buzsáki, G. Physiological properties and behavioral correlates of hippocampal granule cells and mossy cells. *Neuron* **93**, 691–704 (2017).

58. Kesner, R. P. An analysis of dentate gyrus function (an update). *Behav. Brain Res.* **354**, 84–91 (2018).

59. Taniguchi, H. et al. A resource of Cre driver lines for genetic targeting of GABAergic neurons in cerebral cortex. *Neuron* **71**, 995–1013 (2011).

60. Bischofberger, J., Engel, D., Li, L., Geiger, J. R. P. & Jonas, P. Patch-clamp recording from mossy fiber terminals in hippocampal slices. *Nat. Protoc.* **1**, 2075–2081 (2006).

61. Schmidt-Hieber, C., Jonas, P. & Bischofberger, J. Enhanced synaptic plasticity in newly generated granule cells of the adult hippocampus. *Nature* **429**, 184–187 (2004).

62. Guzman, S. J., Schlögl, A. & Schmidt-Hieber, C. Stimfit: quantifying electrophysiological data with Python. *Front. Neuroinform.* **8**, 16 (2014).

63. Efron, B. & Tibshirani, R. J. *An introduction to the bootstrap.* (Chapman & Hall/CRC, London, 1998).

64. Zhao, L., Beverlin, B. 2nd, Netoff, T. & Nykamp, D. Q. Synchronization from second order network connectivity statistics. *Front. Comput. Neurosci.* **5**, 28 (2011).

65. Benjamini, Y. & Hochberg, Y. Controlling the false discovery rate: a practical and powerful approach to multiple testing. *J. R. Stat. Soc. B* **57**, 289–300 (1995).

66. Royer, S. et al. Control of timing, rate and bursts of hippocampal place cells by dendritic and somatic inhibition. *Nat. Neurosci.* **15**, 769–775 (2012).

67. Bittner, K. C. et al. Conjunctive input processing drives feature selectivity in hippocampal CA1 neurons. *Nat. Neurosci.* **18**, 1133–1142 (2015).

68. Han, Z. S., Buhl, E. H., Lörinczi, Z. & Somogyi, P. A high degree of spatial selectivity in the axonal and dendritic domains of physiologically identified local-circuit neurons in the dentate gyrus of the rat hippocampus. *Eur. J. Neurosci.* **5**, 395–410 (1993).

69. Hosp, J. A. et al. Morpho-physiological criteria divide dentate gyrus interneurons into classes. *Hippocampus* **24**, 189–203 (2014).

70. Hefft, S. & Jonas, P. Asynchronous GABA release generates long-lasting inhibition at a hippocampal interneuron–principal neuron synapse. *Nat. Neurosci.* **8**, 1319–1328 (2005).

Author contributions

S.J.G. and P.J. designed the experiments, C.E. performed the in vitro experiments, X.Z. performed the in vivo experiments, C.E., S.J.G., and P.J. analyzed the data, and P.J. wrote the paper. All authors jointly revised the paper.

Additional information

Supplementary Information accompanies this paper at https://doi.org/10.1038/s41467-018-06899-3.

Competing interests: The authors declare no competing interests.

Reprints and permission information is available online at http://npg.nature.com/reprintsandpermissions/

Publisher's note: Springer Nature remains neutral with regard to jurisdictional claims in published maps and institutional affiliations.

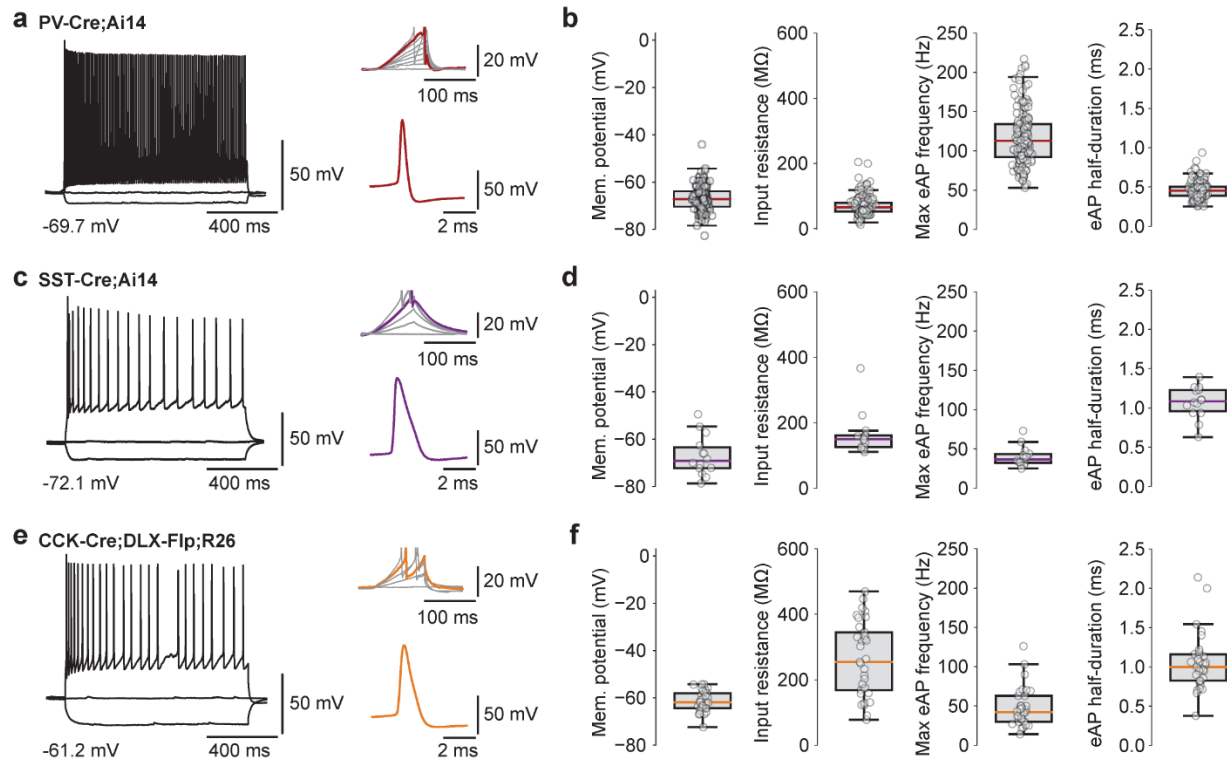**Supplementary Figure 1** | Action potential phenotype and membrane properties of different types of genetically identified interneurons in the dentate gyrus.

(**a**) Functional properties of identified PV⁺ interneurons in the dentate gyrus. Left, voltage changes evoked by long depolarizing and hyperpolarizing current pulses (0.6, 0, and −0.1 nA) applied to the PV⁺ interneuron. Fast-spiking phenotype (> 100 Hz) and low input resistance (< 100 MΩ) are characteristic. Right, single AP waveform evoked by a depolarizing current ramp.

(**b**) Box plots of resting membrane potential (mean, –66.9 mV), input resistance (70.2 MΩ), maximal evoked AP frequency (116 Hz), and evoked AP half-duration (0.45 ms; 173 cells). PV⁺ interneurons were identified in slices based on tdTomato labeling in PV-Cre;Ai14 mice.

(**c, d**) Similar data as in (a, b), but for SST⁺ interneurons. SST-Cre mice were used for labeling.

(**e, f**) Similar data as in (a, b), but for CCK$^+$ interneurons. CCK-Cre;DLX 5/6-Flp mice were used for labeling. In (c, e), voltage changes were evoked by long depolarizing and hyperpolarizing current pulses (0.3, 0, and −0.1 nA).

Box plots in (b, d, and f) show lower quartile (Q1), median (horizontal red line), and upper quartile (Q3). The interquartile range (IQR = Q3–Q1) is represented as the height of the box. Whiskers extend to the most extreme data point that is no more than 1.5 x IQR from the edge of the box (Tukey style). Data from individual cells are plotted on top of the corresponding box.

Supplementary Figure 2 | Coactivation of converging inputs from granule cells is required to initiate APs in PV$^+$ interneurons.
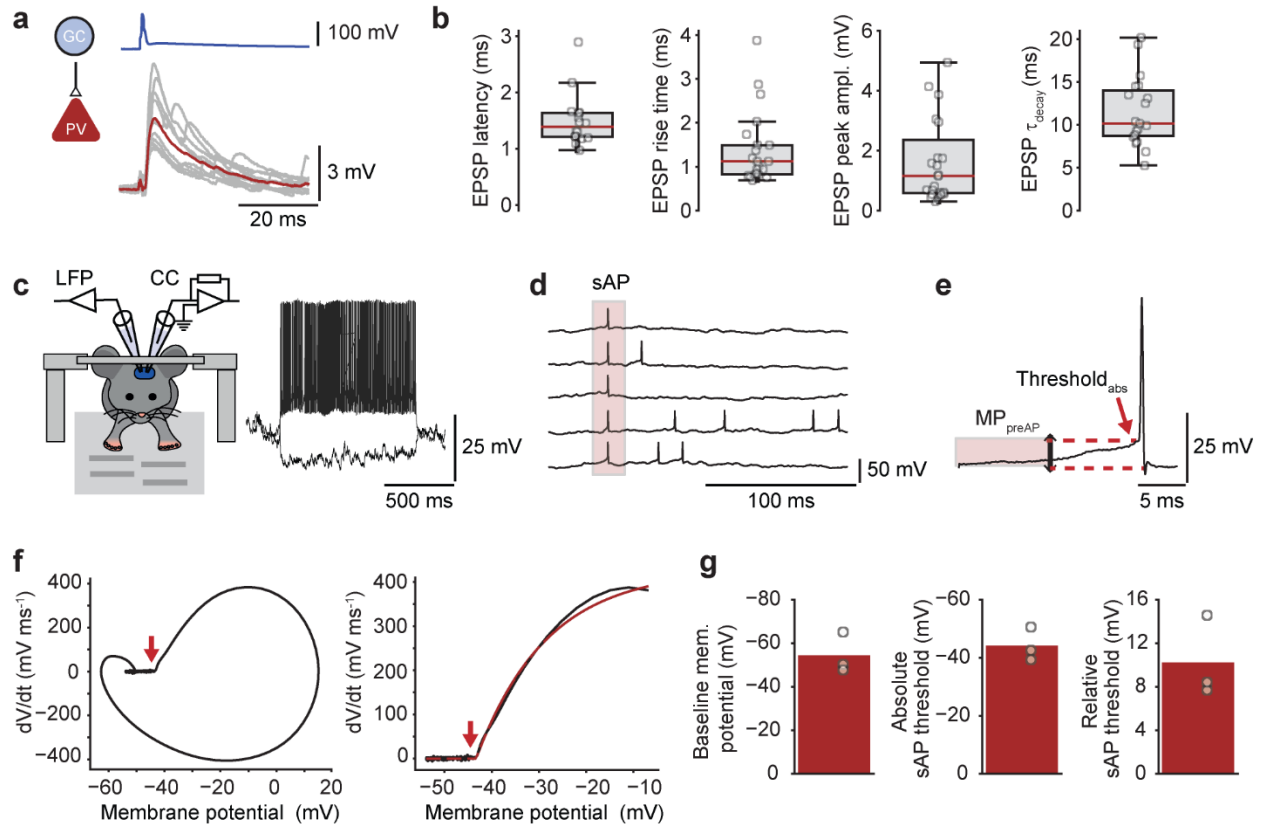
(**a**) Unitary excitatory postsynaptic potentials (EPSPs), with individual synaptic responses (gray) and average trace (red, 15 traces) in a representative GC–PV$^+$ interneuron pair.

(**b**) Box plots of EPSP latency, 20–80% rise time, peak amplitude, and decay time constant.

(**c**) AP properties of fast-spiking interneurons in the dentate gyrus *in vivo* in awake, behaving animals. Left, schematic illustration of recording configuration; CC, whole-cell current clamp; LFP, local field potential recording. Right, traces of membrane potential in response to depolarizing and hyperpolarizing current injections.

(**d, e**) Compressed plot of five spontaneous APs (sAPs) aligned to the sAP peak (d) and expanded plot of a single AP (e). Light red area shows the time interval in which the

baseline membrane potential before the spike was determined. MP_{preAP}, membrane potential preceding AP.

(**f**) Left, phase plot analysis of the AP shown in (e). Right, fit of the rising component of the phase plot by an exponential function including a shift factor (red curve). Red arrows indicate absolute threshold of sAP initiation determined from the shift.

(**g**) Summary bar graph of baseline membrane potential (in time window 10–20 ms before the AP, left), absolute sAP threshold (center), and relative sAP threshold (relative threshold = absolute threshold – baseline membrane potential).

Supplementary Figure 3 | Propagation of evoked EPSPs in PV[+] interneuron networks via gap junctions.
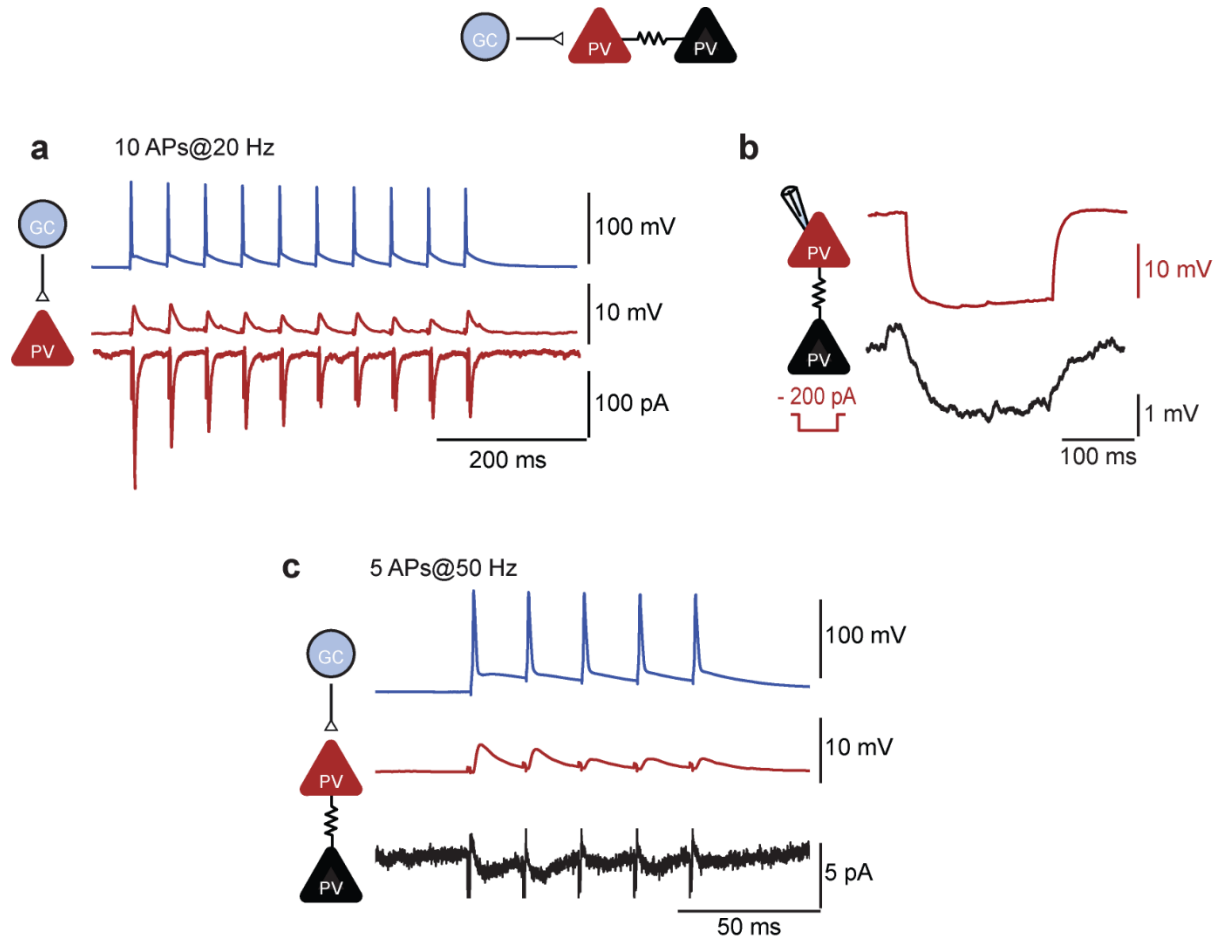
(**a**) Simultaneous recording from a GC and two PV[+] interneurons. APs in the GC led to monosynaptic EPSPs (current-clamp conditions) or EPSCs (voltage-clamp conditions) in the first PV[+] interneuron.

(**b**) The two recorded PV[+] interneurons were coupled by gap junctions.

(**c**) Propagation of EPSPs from PV[+] interneuron 1 (red) to PV[+] interneuron 2 (black). APs in the GC led to EPSCs with peak amplitude < 5 pA in the second PV[+] interneuron. These excitatory synaptic events were apparently propagated via gap junctions[S1].

Supplementary Figure 4 | Relation between intersomatic distance and axon length.
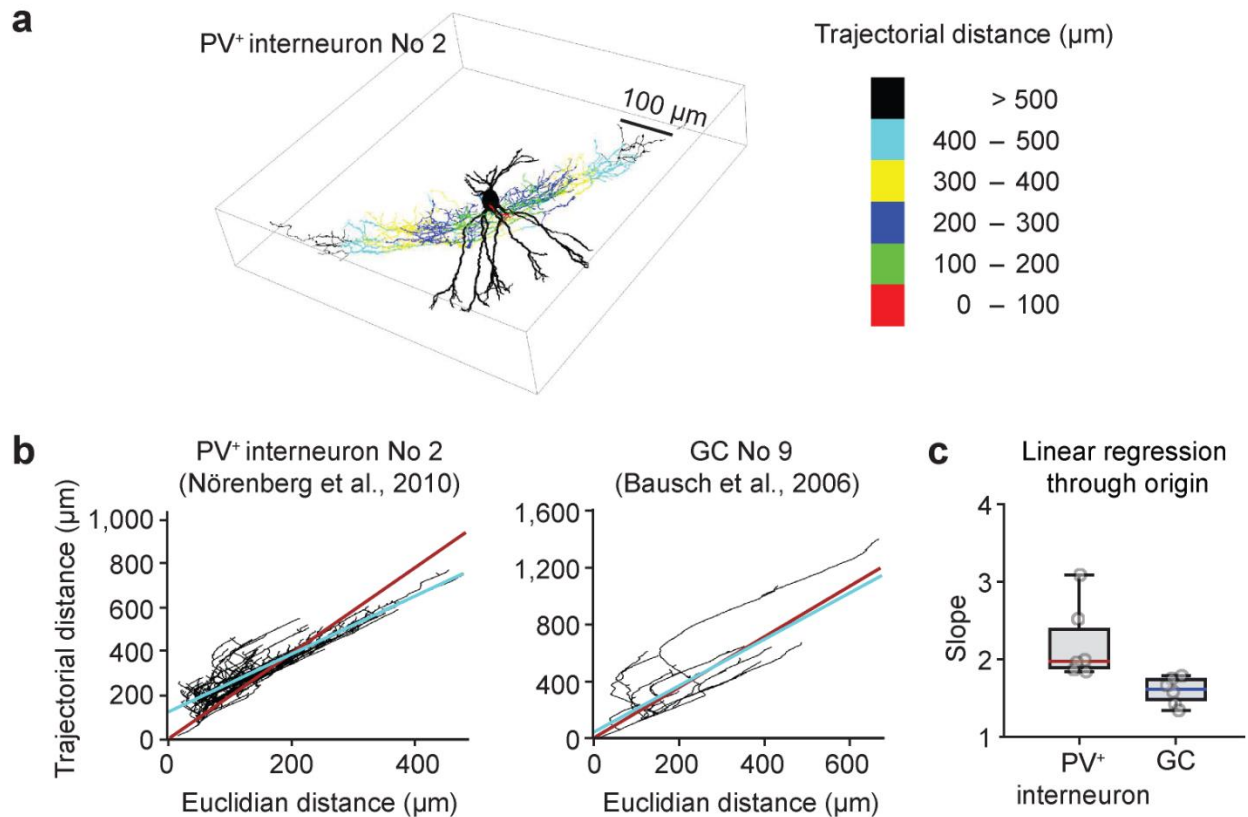
(**a**) Reconstructed fast-spiking PV⁺ interneuron in the dentate gyrus. Soma and dendrites are drawn in black, axon is color coded according to the length of the axonal path. Cell No 2 from the sample of dentate gyrus PV⁺ interneurons from Nörenberg et al.[S2].

(**b**) Plot of axon length (trajectorial distance) against intersomatic distance (Euclidian distance). Data points were analyzed by regression with linear function through origin (red line) or with offset (light blue line). Left, PV⁺ interneuron (cell No 2; Ref. S2); right, GC (cell No 9; Ref. S3). All distance values were measured relative to the center of the soma.

(**c**) Slope of the axon length–intersomatic distance relation (fit with line through origin). Box plots show lower quartile (Q1), median (horizontal red line), and upper quartile (Q3). The interquartile range (IQR = Q3–Q1) is represented as the height of the box. Whiskers extend to the most extreme data point that is no more than 1.5 x IQR from the edge of the box (Tukey style). Data from individual cells are plotted on top of the corresponding

box. Data from six fast-spiking PV$^+$ interneurons in the dentate gyrus and six dentate gyrus GCs (Cells No 9, 47, 52, 56, 58, and 61; Ref. S3).

Supplementary Table 1 | Abundance of lateral inhibition in different brain regions.

Brain region	p_{IE} / p_{EI} [a]	$n_{lateral}$ / $n_{recurrent}$ [b]	Reference
Visual and somatosensory cortex	0.99	0.13	Holmgren et al., 2003 [S4]
Visual cortex	2.5	2.0	Yoshimura and Callaway, 2005 [S5]
Entorhinal cortex	1.5	1.1	Couey et al., 2013 [S6]
Presubiculum superficial	1.04	1.3	Peng et al., 2017 [S7]
Presubiculum deep	0.68	0.67	Peng et al., 2017 [S7]
Dentate gyrus	3.83 [c]	9.25	This paper

(a) p_{IE} / p_{EI} indicates ratio of mean inhibitory IN–PN to mean excitatory PN–IN connection probability.

(b) $n_{lateral}$ / $n_{recurrent}$ represents ratio of number of lateral inhibition motifs and recurrent inhibition motifs in all recorded PN–IN pairs.

(c) Quantified from the integral under the connection probability–distance curves (**Fig. 3**).

Supplementary References

S1.   Galarreta, M. & Hestrin, S. A network of fast-spiking cells in the neocortex connected by electrical synapses. *Nature* **402**, 72–75 (1999).

S2.   Nörenberg, A., Hu, H., Vida, I., Bartos, M. & Jonas, P. Distinct nonuniform cable properties optimize rapid and efficient activation of fast-spiking GABAergic interneurons. *Proc. Natl. Acad. Sci. USA* **107**, 894–899 (2010).

S3.   Bausch, S.B., He, S. & Dong, Y. Inverse relationship between seizure expression and extrasynaptic NMDAR function following chronic NMDAR inhibition. *Epilepsia* **51** Suppl 3, 102–105 (2010).

S4.   Holmgren, C., Harkany, T., Svennenfors, B. & Zilberter, Y. Pyramidal cell communication within local networks in layer 2/3 of rat neocortex. *J. Physiol.* **551**, 139–153 (2003).

S5.   Yoshimura, Y. & Callaway, E.M. Fine-scale specificity of cortical networks depends on inhibitory cell type and connectivity. *Nat. Neurosci.* **8**, 1552–1559 (2005).

S6.   Couey, J.J., Witoelar, A., Zhang, S.J., Zheng, K., Ye, J., Dunn, B., Czajkowski, R., Moser, M.B., Moser, E.I., Roudi, Y. & Witter, M.P. Recurrent inhibitory circuitry as a mechanism for grid formation. *Nat. Neurosci.* **16**, 318–324 (2013).

S7.   Peng, Y., Barreda Tomás, F.J., Klisch, C., Vida, I. & Geiger, J.R.P. Layer-specific organization of local excitatory and inhibitory synaptic connectivity in the rat presubiculum. *Cereb. Cortex* **27**, 2435–2452 (2017).